

# NASA CR- 177896

Final Report for

NASA Contract NAS5-25690

by

D. A. Gurnett and R. L. Huff



(NASA-CR-177896) [ACTIVITIES SUPPORTING  
DATA ANALYSIS FROM THE PLASMA WAVE  
INSTRUMENT ON THE DYNAMICS EXPLORER (DE-1) 26420  
SPACECRAFT] Final Report, 5 Mar. 1980 - 31  
Jul. 1983 (Iowa Univ.) 211 p

N86-72339  
THRU  
N86-72341  
Unclassified  
44008  
00/89

Department of Physics and Astronomy  
THE UNIVERSITY OF IOWA

Iowa City, Iowa 52242

Graduate College  
The University of Iowa  
Iowa City, Iowa

CERTIFICATE OF APPROVAL

---

MASTER'S THESIS

---

This is to certify that the Master's thesis of

Daniel Ray Weimer

has been approved by the Examining Committee  
for the thesis requirement for the Master of  
Science degree in Physics at the May, 1983  
graduation.

Thesis committee:

Stanley S. Hanham  
Thesis supervisor

Daniel A. Smith  
Member

Daniel Ray Weimer  
Member

**Final Report for  
NASA Contract NAS5-25690  
by  
D. A. Gurnett and R. L. Huff**

**April 1986**

**Department of Physics and Astronomy  
The University of Iowa  
Iowa City, IA 52242  
Telephone: 319/353-3527**

*14630032*

## I. INTRODUCTION

This report describes the activities supported by NASA contract NASS-25690 for the period from March 5, 1980, to July 31, 1983. This contract supported the reduction and analysis of data from the Plasma Wave Instrument on the Dynamics Explorer (DE-1) spacecraft.

The Dynamics Explorer spacecraft-pair was launched in 1981 for the purpose of studying coupling between the magnetopause, ionosphere and the atmosphere. Within this framework, specific objectives for the Plasma Wave Instrument (PWI) were as follows:

- (1) Measure the intensity and spectrum of electromagnetic and electrostatic waves associated with auroral, plasmaspheric, polar cusp and other magnetospheric plasma processes in the frequency range of 1 Hz to 2 MHz;
- (2) Identify regions of large quasi-static electric fields, especially those associated with auroral electron acceleration;
- (3) Determine growth rates and spectral characteristics of waves stimulated by VLF transmitters and naturally occurring VLF waves in the plasmapause region;
- (4) Measure wave propagation direction (Poynting vector), wave normal angle and wave polarization components to identify the source regions and source characteristics of kilometric radiation and other plasma waves;

(5) Assess the characteristics and the importance of electrostatic waves in plasma processes such as particle acceleration and particle diffusion, especially in the auroral and plasmapause regions; and

(6) Associate the measured plasma wave characteristics with plasma distribution functions, current systems, plasma flow parameters, auroral images, electric field regions and characteristics of the ionosphere and upper atmosphere measured by the other DE instruments in order to discern the plasma processes coupling the magnetosphere and atmosphere.

After launch, PWI-related activities fell primarily within two main areas:

- (1) mission operations and data processing;
- (2) data analysis and publication.

These topics will be addressed in the sections that follow.

## II. MISSION OPERATIONS AND DATA PROCESSING

Activities comprising the mission operations and data processing effort occurred over the entire contract period and included the following items.

### Pre-Launch

- Generation and testing of software for the production of Mission Analysis Files at the GSFC DE Central Data Management Facility
- Generation and testing of special processing and data display software
- Generation and testing of software and communication procedures for commanding and monitoring the Plasma Wave Instrument

### Post-Launch

- Production of Mission Analysis Files at the GSFC DE Central Data Management Facility
- Transmission of Mission Analysis Files to Iowa via magnetic tape or synchronous data line
- Maintenance of Iowa in-house DE database
- Production of standard DE/PWI data products such as Step Frequency Receiver spectrograms (electric, magnetic and wave characteristics), DE DC electric field plots and survey films of the wideband data
- Production of special plots and other data products for Iowa investigators and other investigator groups
- Scheduling of PWI instrument commands and the monitoring of instrument performance
- Other activities including software modification and maintenance, maintenance and repair of DE equipment at Iowa, and tape handling, storage and dispersal

### III. DATA ANALYSIS AND PUBLICATIONS

During the period from the launch of DE-1 in August 1981 to July 31, 1983, a total of ten papers were published or submitted for publication by our group in the area of research supported by our DE data analysis contract (NAS5-25690). The titles and authors of these papers, a set of abstracts, copies of the papers and a list of oral presentations are included in Section IV. Many of these papers involve correlative investigations with other research investigators from the DE-1 and DE-2 spacecraft programs, as well as multi-spacecraft investigations with research investigators from the ISEE, IMP, Isis and S3-3 spacecraft programs.

Two graduate students completed their thesis projects using DE data. For his M.S. thesis, Mr. Dan Weimer completed a study of magnetospheric electric fields measured by DE-1. The main objective of this study was to derive the techniques used to analyze DE-1 quasi-static electric field data and to plot polar cap plasma convection patterns. During the contract period, Mr. Weimer began research for his Ph.D. thesis which involved comparing auroral zone electric field measurements from DE-1 with electric field measurements from DE-2, both projected to a common altitude, at times of magnetic conjunctions. This study was a multi-instrument collaboration with M. Sugiura, N. Maynard, J. Burch and E. Shelly. Although the research was not completed during the contract

period, Mr. Weimer went on to verify the steady-state theory which postulates that there are parallel potential drops associated with variations in the perpendicular electric fields resulting in field-aligned currents.

For her M.S. thesis, Ms. Ann Persoon has completed a study on the electron density profile over the northern polar cap. This study utilizes PWI electric field spectrograms as well as low-altitude, topside sounder data from the Alouette II and Isis-1 satellites to obtain a median density profile from  $1 R_e$  to  $5 R_e$ . The main result of this study is that polar cap electron densities exhibit a power law distribution above  $2 R_e$ , varying as  $R^{-3.85}$ .

#### ACKNOWLEDGEMENTS

I wish to thank Stan Shawhan and Don Gurnett for valuable discussions on the DE-1 electric field data and magnetospheric electric fields in general. Credit is due to Richard Huff for his efforts in getting electric field data transferred from NASA/GSFC to the University of Iowa. I thank Terry Averkamp for the utility programs he provided for reading the data tapes and other assistance he gave on using the Physics Department's computer facilities. This research is supported by NASA/GSFC Contracts NAS5-25690 and NAS5-24294.

NASS-25690 P121

D,  
26421

MAGNETOSPHERIC ELECTRIC FIELDS MEASURED WITH  
DYNAMICS EXPLORER-1

by

Daniel Ray Weimer

A thesis submitted in partial fulfillment  
of the requirements for the degree of  
Master of Science in Physics  
in the Graduate College of  
The University of Iowa

May, 1983

Thesis supervisor: Professor Stanley D. Shawhan

**"Page missing from available version"**

## ABSTRACT

The Plasma Wave Instrument (PWI) on the Dynamics Explorer-1 satellite has been used to measure DC electric fields in the earth's magnetosphere. The DE-1 spacecraft is in an elliptical polar orbit with a radial range of 1.106 to 4.67  $R_e$ . The DC electric field measurements are obtained with two sets of double probes. A long wire antenna with a tip-to-tip length of 215 m measures the electric field in the satellite spin plane. A tubular antenna with a length of 9 m is used for measurements along the spin axis. Data from the sensitive long wire electric field probe is given the most attention. This antenna is rotating with the spacecraft at a rate of one revolution every 6 seconds. By applying a least square error fit to the sinusoidal waveform, the magnitude and orientation of the electric field in the spin plane of the spacecraft is determined. Further computations reduce the measured electric field to components perpendicular and parallel to the magnetic field. Due to the short length of the tubular antenna, the electric field measured along the spin axis shows interference from a non-uniform electric potential around the body of the spacecraft. A simple averaging approach is used to filter some of the interference from the DC measurements. The results of the computations are plotted on graphs with several different formats. One type of graphical output shows the plasma

convection velocity component which is calculated from the electric field measured in the spin plane. These graphs are used extensively in a discussion on polar cap plasma convection. The DE-1 observations affirm the existence of a two-cell circulation pattern. Flow velocities over 2 km/s are seen near the reversals which occur at the center of the convection cells. But the plasma convection pattern is found to be highly variable; the two-cell circulation is often absent. The variations which occur on an orbital and daily basis are compared to changes in the Interplanetary Magnetic Field (IMF) and geomagnetic activity indices. The north-south polarity of the IMF appears to correlate better than the geomagnetic activity with a stronger and more uniform convective flow. Electric field measurements in the auroral zone are discussed. Oppositely directed fields with a magnitude of 100 to 200 mV/m are a common feature, but the absence of "paired electrostatic shocks" of a greater magnitude contradicts measurements with the S3-3 satellite reported in the literature. Electric fields having the paired shock structure which are found in association with field aligned currents have the characteristics of an "auroral vortex." Spectrograms from the Plasma Wave Instrument indicate that these events produce localized plasma waves over a wide frequency range. The final chapter on the observations discusses the relationship between unusual electric fields detected at low latitude concurrent with Stable Auroal Red (SAR) arcs. The electric fields are associated with plasma flows of over 8 Km/s. The phenomenon had been reported before under the name of "Subauroral ion drift", but there had been no previous connection with SAR arcs.

## TABLE OF CONTENTS

	Page
LIST OF TABLES . . . . .	vi
LIST OF FIGURES . . . . .	vii
CHAPTER	
I. INTRODUCTION . . . . .	1
II. INSTRUMENTATION . . . . .	3
III. DATA REDUCTION . . . . .	6
Data Processing System . . . . .	6
Calculation of Electric Fields . . . . .	7
Graphical Display of Data . . . . .	15
IV. POLAR CAP PLASMA CONVECTION . . . . .	21
Previous Results . . . . .	21
DE-1 Results. . . . .	23
V. AURORAL ZONE ELECTRIC FIELDS . . . . .	28
Previous Results. . . . .	28
DE-1 Results. . . . .	30
VI. STABLE AURORAL RED ARCS. . . . .	33
Previous Results. . . . .	33
DE-1 Results. . . . .	34
VII. DISCUSSION . . . . .	37
VIII. CONCLUSIONS . . . . .	39
REFERENCES. . . . .	42
APPENDIX A: TABLES . . . . .	45
APPENDIX B: FIGURES. . . . .	47

LIST OF TABLES

Table	Page
1. Characteristics of the Electric Field Sensors in the Plasma Wave Instrument on the Dynamics Explorer-1 Spacecraft . . . . .	46

## LIST OF FIGURES

Figure	Page
1. Graph of electric field strengths measured along the spacecraft Z axis and X axis . . . . .	48
2. Location of the long wire electric field probes on the DE-1 spacecraft. . . . .	50
3. Illustration of the time relationship between successive data records and each measurement. . . . .	52
4. Graph of electric field data after computer processing . . . . .	54
5. Diagram of the orientation of the $E_1$ electric field at different positions of the DE-1 spacecraft in its orbit. . . . .	56
6. Illustration of a case when the magnetic field is not entirely in the spin plane. . . . .	58
7. Peak electric field summary plot . . . . .	60
8. Southern hemisphere plasma convection measured from 6:15 UT to 6:39 UT on day 81343 (December 9, 1981) . . . . .	62
9. Empirical models of polar cap potentials derived by Heppner to match patterns in the OGO-6 data . . . . .	64
10. Interplanetary magnetic field data and geomagnetic activity indices for day 81343 (December 9, 1981) . . . . .	66
11. Southern hemisphere plasma convection measured from 8:06 UT to 8:29 UT on day 81287 (October 14, 1981) . . . . .	68

Figure		Page
12.	Southern hemisphere plasma convection measured from 14:54 UT to 15:17 UT on day 81287 (October 14, 1981) . . . . .	70
13.	Southern hemisphere plasma convection measured from 21:49 UT to 22:14 UT on day 81287 (October 14, 1981) . . . . .	72
14.	Interplanetary magnetic field and geomagnetic activity indices for day 81287 (October 14, 1981) . . . . .	74
15.	Southern hemisphere plasma convection measured from 4:29 UT to 4:53 UT on day 81294 (October 21, 1981) . . . . .	76
16.	Southern hemisphere plasma convection measured from 11:16 UT to 11:39 UT day 81294 (October 21, 1981) . . . . .	78
17.	Southern hemisphere plasma convection measured from 18:08 UT to 18:32 UT day 81294 (October 21, 1981) . . . . .	80
18.	Southern hemisphere plasma convection measured from 1:03 UT to 1:28 UT day 81295 (October 22, 1981) . . . . .	82
19.	Southern hemisphere plasma convection measured from 4:25 UT to 4:50 UT day 81296 (October 23, 1981) . . . . .	84
20.	Southern hemisphere plasma convection measured from 11:12 UT to 11:35 UT day 81296 (October 23, 1981) . . . . .	86
21.	Southern hemisphere plasma convection measured from 4:22 UT to 4:46 UT day 81298 (October 25, 1981) . . . . .	88
22.	Geomagnetic activity indices for the period from day 81294 (October 21, 1981) to day 81298 (October 25, 1981) . . . . .	90
23.	Southern hemisphere plasma convection measured from 8:57 UT to 9:23 UT on day 81364 (December 30, 1981) . . . . .	92

Figure		Page
24. Interplanetary magnetic field data and geomagnetic activity indices for day 81364 (December 30, 1981) . . . . .		94
25. Example of oppositely directed electric fields detected on auroral field lines . . . . .		96
26. Northern hemisphere plasma convection measured from 14:35 UT to 15:35 UT on day 82092 (April 2, 1982) . . . . .		98
27. High-resolution electric field data for the auroral vortex event at 15:27 UT on day 82092 . . . . .		100
28. Plasma Wave Instrument spectrogram for 14:30 UT to 18:30 UT on day 82092 (April 2, 1982) . . . . .		102
29. Southern hemisphere plasma convection measured from 22:02 UT to 22:43 UT on day 82108 (April 8, 1982) . . . . .		104
30. Plasma Wave Instrument spectrogram for 21:30 UT to 23:30 UT on day 82108 (April 18, 1982) . . . . .		106
31. Example of an unusual, low latitude electric field found on a magnetic field line coincident with an SAR arc . . . . .		108
32. Electric field measurement from the VEFI experiment on the low-altitude DE-2 spacecraft . . . . .		110

## CHAPTER I

### INTRODUCTION

The Dynamics Explorer (DE) spacecraft were launched by the National Aeronautics and Space Administration for the purpose of investigating the coupling between the earth's magnetosphere and ionosphere, and the transfer of energy from the solar wind and solar radiation to the near-earth space environment. The two DE satellites were launched in August of 1981. DE-1 makes measurements primarily in the magnetosphere; the orbit is highly elliptical, with perigee at 675 km ( $1.106 R_e$ ) and apogee at 23,400 km ( $4.67 R_e$ ). DE-2 orbits in the thermosphere at altitudes of 305 to 1300 km. The spacecraft are in coplanar polar orbits. Further details of the Dynamics Explorer program are provided by Hoffman et al. [1981a,b].

The Plasma Wave Instrument (PWI) on DE-1 measures both plasma wave phenomena and quasi-static electric fields. The objective of this paper is to document in detail the techniques used to analyze the data from the electric field measurements, and present initial observations on various electric field phenomena.

Electric fields in the magnetosphere play a key role in the transfer of energy and particles from the solar wind to the magnetosphere, which is defined as a cavity in the streaming solar plasma, inside which the field lines of the planetary magnetic field are

confined. Charged particles in the magnetosphere are transported and accelerated by electric fields. Such fields are thought to be responsible for the aurora or "northern lights," as the phenomenon is more popularly known. A review of the current knowledge of magnetospheric electric fields is given by Stern [1977]. Numerous references are presented in the review.

Although a considerable amount of data has been collected with the Dynamics Explorer spacecraft, limited data processing facilities at NASA have restricted the amount of PWI DC electric field data processed to date. Consequently, this paper will focus on the general nature of the electric field data and on three specific topics:

- (1) The polar cap plasma convection electric field system.
- (2) The auroral zone electric fields and associated plasma wave phenomena.
- (3) The electric fields observed on magnetic field lines coincident with stable auroral red arcs.

## CHAPTER II

### INSTRUMENTATION

The entire Plasma Wave Instrument on DE-1 is described by Shawhan et al. [1981]. Of concern here are mainly the instrument sub-systems used for D.C. electric field measurements.

Using the double floating probe technique, the electric field is determined from the measurement of the floating potentials of identical probes located in symmetric positions relative to the body of the spacecraft. The difference in the potentials divided by the distance separating the probes gives one vector component of the electric field. Further information about this technique can be found in the papers by Fahleson [1967] and by Cauffman and Gurnett [1972]. The DE-1 spacecraft has two sets of probes. A 9 m tip-to-tip tubular electric antenna is used for electric field measurements along the spin axis of the spacecraft ( $E_z$ ). A 215 m tip-to-tip long wire antenna perpendicular to the spin axis is used to measure the electric field in the spin plane ( $E_x$ ) of DE-1.

The tubular electric antenna is constructed from silver-plated BeCu elements, 2.8 cm in diameter and 4 m long. The elements are mounted on opposite ends of the spacecraft directly on the spin axis to eliminate the effects of centrifugal force on the antennas. The spacecraft body is 1 m high, resulting in a total distance of 9 m

between the tips. The inboard 3 m of each element has an insulating coating of teflon. As the plasma potential is measured between the midpoints of the conductors, the effective electrical length is 8 m.

The long wire electric antenna is constructed from BeCu wire with 7 strands, each having a diameter of .005"; five gram masses on each tip serve to hold the wires in an extended position by centrifugal force. The spacecraft spins at a rate of 10 RPM, or one revolution every 6 seconds. The antenna specifications previously published [Shawhan et al., 1981] described the wires as having lengths of 100 m with the inboard 71.1 m insulated with Styland, resulting in an effective DC electrical length of 173.1 m. The construction of the antenna on DE-1 is actually the same as the long antenna on the ISEE-1 spacecraft, which has a tip-to-tip length of 215 m. This is more consistent with an effective electrical length of  $186 \pm 1$  m that is measured.

To minimize the error caused by currents drawn from the space plasma, each antenna is connected to a preamplifier with an input impedance of  $10^{10}$  ohms. The preamplifier outputs are fed to differential amplifiers to obtain the potential difference between antenna elements. There are two differential amplifiers with different gains on both the  $E_z$  and  $E_x$  antennas. A high-gain amplifier is for measurements of weak electric fields at high resolution, while a low-gain output enables measurements of strong electric fields, which saturate the high-gain amplifier. Table 1 summarizes the measurement range and resolution obtained with each antenna and amplifier. Range switching is not required in the spacecraft electrical system as both output channels on each axis are received on the ground.

The amplifier outputs, which simply are DC voltage levels, are sampled 16 times per second by an analog-to-digital converter with an 8 bit digital output. The raw telemetry data received on the ground for the electric field measurements consists of four sets of integers from 0 to 255 representing measurements spaced apart in time by 62.5 msec. The next chapter describes the procedures required to convert these numbers into scientifically meaningful data.

The Plasma Wave Instrument on DE-1 also has the capability to measure the electric and magnetic components of plasma waves. Certain signatures in the plasma wave spectrograms are correlated with quasi-static electric fields. Examples will be presented in Chapter V. Wave electric fields are measured over a frequency range of 1 Hz to 2 MHz. Wave magnetic fields are sensed with a search coil from 1 Hz to 1 KHz and a loop antenna from 100 Hz to 400 KHz. The step frequency correlator provides a 128-point spectrum from 100 Hz to 400 KHz; the low frequency correlator provides 8-point spectra from 1 Hz to 100 Hz. Spectra are obtained every 32 s for 2 antennas. In addition, high time-resolution data can be obtained through a wideband analog data link. Capabilities of the PWI include distinction between electromagnetic and electrostatic wave phenomena and determination of wave polarization and propagation direction.

The electrical power for the instruments on DE-1 is provided by solar cells. The supply of power is insufficient to operate all of the different instruments continuously. As each instrument has an "on" time of about 50%, there are periodic gaps in the data which are collected.

## CHAPTER III

### DATA REDUCTION

#### Data Processing System

The science data which are acquired by the Dynamics Explorer spacecraft are radioed to NASA tracking stations on the ground. All telemetry data are transferred to the Science Data Processing System at Goddard Space Flight Center where it is stored on magnetic tape. The telemetry data must be promoted from the tape data base to on-line computer disk memory for further processing which is done on a Xerox/Honeywell Sigma-9 Computer. Details of the DE Science Data Processing System are described by Smith et al. [1981].

Science investigators located at different sites across the country are responsible for the processing and analysis of the data from the separate instruments on the spacecraft. The DE investigators access the data with remote terminals located at their respective facilities. But the computations required to process all of the data exceeds the capabilities of the relatively small Sigma-9 system. As a result, each of the investigating teams has experienced a slow processing rate. This rate has been marginally adequate for the processing of the Plasma Wave Instrument spectrograms but simultaneous processing of the DC electric field data would have been impractical from the remote terminal. For this reason, the electric field data are

sent on magnetic tape to the University of Iowa where a Univac 418 Computer in the Department of Physics and Astronomy is used for the numerical analysis. A Calcomp microfilm plotter provides for a graphical display of the processed data.

Information about the spacecraft's orbit and attitude is written onto the magnetic tapes along with the "raw" electric field data. This information is vital for the numerical analysis. The process of getting the numbers extracted from the telemetry and orbit/attitude data bases and written onto a tape is initiated from the remote terminal at Iowa. This limits the rate at which data tapes are received. For this reason, the following chapters which describe the scientific results are based on only a small subset of the electric field data which has actually been collected with the Plasma Wave Instrument. Data from about 36 different days has been processed at the present.

#### Calculation of Electric Fields

The four analog channels, two from  $E_x$  and two representing  $E_z$ , are multiplexed to a common A/D converter. The converter is designed to have a full-scale digital output of 255 "counts" with an analog input of 5.12 volts. In order to measure both positive and negative electric fields a nominal voltage offset of +2.56 V is added to the outputs of the DC amplifiers. In practice the offset is added to the inputs of the different high/low gain amplifiers, scaled to the gain of the final amplifier stage. With this scheme a digital output of 127 translates to a measurement of 0, while counts of 0 and 255 correspond to respective voltage measurements of -2.54 V and +2.56 V.

A digital output number  $N$  is translated to an electric field value with the formula:

$$E = \frac{2.56 (N - N_0)}{G L_{\text{eff}}} \quad (1)$$

$N_0$  is the integer number representing a value of zero for the electric field.  $L_{\text{eff}}$  is the effective antenna length and  $G$  is the gain of the amplifier. A summary of the relevant parameters for the DC electric field measurements with DE-1 is contained in Table 1. Included in the table are the full scale electric fields and 1 bit resolution of each antenna and amplifier combination. The DC amplifier gains were obtained from instrument calibration measurements on the ground. Table 1 contains two values for the length of the  $E_x$  antenna. One is the previously published figure; the other length has been determined from on-orbit "calibration" measurements of the  $\underline{V} \times \underline{B}$  electric field, where  $\underline{V}$  is the spacecraft velocity. More information about this follows.

The number  $N_0$  used in equation (1) has the nominal value of 127. Examination of the telemetry data, however, revealed that on both axes the simultaneous high-gain and low-gain outputs did not agree. The relative amplitude changes between each step were exactly as expected but there appeared to be a constant DC offset between outputs. On the X axis the high-gain data were at a zero level of 127 while the low-gain output was at 123, which scales to  $-74 \text{ mV/m}$ ! Since the antenna is rotating in the electric field the output should follow a sine wave centered on zero. The high-gain numbers had the expected waveform, centered around 127, while the low-gain numbers had a zero

crossing at 123. The obvious method to obtain the proper agreement between channels was to subtract 123 from the low-gain digital values before multiplying by the scale factors to obtain mV/m. With this change in the conversion, the different channels agree to within the 1 bit resolution of the low-gain numbers. A similar offset occurs in the Z axis data, where 124 is subtracted from the low-gain values to obtain the proper agreement. However, since the antenna is not rotating, a sine wave is not available to check the zero-level. The origin of the offset appears to be in the different potentials applied at the inputs of each final amplifier stage in order to bias each output by 2.56 V.

After the conversion of digital counts to mV/m the electric field strengths on the Z axis and X axis can be plotted as a function of time, as in Figure 1. Normally the high-gain data are used due to the higher resolution, but above the saturation levels of the high-gain outputs the low-gain data are selected. The telemetry data from DE-1 are divided into 8 second "records" with 128 data points. Each record has a time-tag in units of milliseconds-of-day (UT). This data format influences the design of these plots and subsequent analysis operations.

The X axis plot in Figure 1 shows the expected sine waveform with a period of 6 seconds. However, the Z axis electric field should be fairly constant, without any spin modulation. The data show "spikes" occurring twice each spin period and a nonsymmetrical spin modulation. This interference on the Z axis has been very persistent during the spacecraft mission, but the magnitude of the noise spikes appears to depend on plasma density. At high altitudes ( $2 - 4.5 R_E$ ) the spikes are

very large and completely mask the true electric field. When the spacecraft enters the plasmasphere the spikes are attenuated, but some spin modulation still exists. The interference seems to be due to differential charging of the spacecraft skin. Similar potential variations--several volts in magnitude--are also detected with the RIMS instrument [R. Chappell, private communication, 1981]. This interference has severely limited the utility of DC electric field measurements with the tubular electric antenna ( $E_z$ ). Consequently, the data analysis has been concentrated on the measurements with the long wire antenna ( $E_x$ ). This antenna, in the spacecraft orbit plane, measures the N-S and radial electric fields. As the magnetic field vector generally lies in this plane, electric field components parallel and perpendicular to B can be determined. Measurements of the plasma convection component perpendicular to the orbit of the spacecraft can be obtained with the  $E_x$  antenna.

From the sine wave measured with the rotating antenna it is necessary to determine the magnitude and direction of the electric field in the spin plane of the DE-1 spacecraft. This determination is carried out with a computer program which does a least square error fit of the data to obtain the magnitude and phase of the sine wave. Each data sample is taken at a specific time; the time difference between the sample time and a reference time is converted to a relative angular position (of the probe antenna) by multiplication of the time difference with the spacecraft's angular rotation rate. The phase obtained with the curve-fitting routine is the angle between the peak of the sine wave and the reference time (angle). The reference is

obtained from the nadir times in the DE data base, derived from earth horizon sensors on DE-1. At the nadir times the +Y axis of the spacecraft is pointing toward the center of the earth. This orientation provides the reference necessary to convert the measured electric field to a known coordinate system, as the vector position of the satellite from the center of the earth is a well known function of time. The Z axis, given in geocentric equatorial inertial (GEI) coordinates, remains relatively constant. The Z axis is perpendicular to the orbit plane. It is maintained to  $\pm 1^\circ$ . Given the satellite position vector ( -Y axis orientation) in GEI coordinates, the X axis is derived from  $\underline{Y} \times \underline{Z}$ . From the orientations of the X, Y, and Z spacecraft axes, specified as unit vectors in GEI coordinates, one has an orthogonal transformation for converting vectors from GEI coordinates to spacecraft coordinates (and vice versa). This transformation is a function of spacecraft position, hence it changes with time. It must be calculated for each eight second period spanning each record of data. The nadir and positional data are available from the DE orbit-attitude (OA) data base at NASA/GSFC.

The long wire antennas on the DE-1 satellite are mounted at points  $15^\circ$  from the line which defines the Y axis. Since the zero-phase points are assumed to be at the nadir times, it is seen in Figure 2 that there should be a  $165^\circ$  lag between the measured electric field and one directed along the +Y axis. With the magnitude,  $E_0$ , and phase angle,  $\phi$ , of the sine wave determined by the curve fitting routine, the x and y components of the electric field in spacecraft coordinates are obtained from the formulas:

$$E_y = E_o \cos(\phi - 165^\circ) \quad (2a)$$

$$E_x = E_o \sin(\phi - 165^\circ) \quad (2b)$$

The least-squares fit routine works on data spanning one complete, six second spin period. As seen in Figure 1, the electric field may change considerably in one period. Rapid changes in the field can be determined with a greater accuracy by overlapping the time periods in which the curve fitting is done. With the data formatted into eight second records the best way to obtain continuity is to use a two second overlap. This choice results in exactly two measurements or data points for every record (Figure 3). As the data analysis presently is performed by reading data from magnetic tape and writing results to another tape, only two records of input data need to be kept in computer memory at any given time.

Often there may be considerable noise or distortion in the sine wave in regions where there are large and rapid fluctuations in the electric field. Without a "good" sine wave, the magnitude and phase determination may not be accurate. To get some idea of the reliability of the measurements, the error in the curve-fit is calculated. The "chi" coefficient is obtained from the formula:

$$\text{Chi} = \left[ \frac{\sum_{i=1}^N \left( \frac{M_i - F_i}{E_o} \right)^2}{N} \right]^{1/2} \quad (3)$$

$M_i$  is the measured electric field at each point  $i$  and  $F_i$  is the electric field of the sine wave function fitted to the data. The expression for chi in equation (3) is similar, but not identical to the "chi square" calculation normally used in statistical analysis. The error coefficient thus calculated is dimensionless, as the error of each data point is scaled to the sine wave magnitude  $E_0$ . The total number of points,  $N$ , is normally 96, unless there are "drop-outs" in the data record. A reasonably good sine wave will have a chi coefficient less than 0.1. If the measured electric field is obscured by noise the curve-fitting algorithm still produces numbers for the magnitude and phase of a sine wave fit. In this case, chi will be greater than one indicating that the fit is not reliable.

The interference on the Z axis can be filtered out to some extent by taking an average (mean) of a number of data points. Since the  $E_z$  data are processed simultaneously with the  $E_x$  data, considerable simplicity is achieved by averaging over the same six second periods in which the  $E_x$  data are analyzed. The standard deviation is calculated for each period as an indicator of the amount of noise present.

A significant proportion of the measured electric field is due to the motion of the satellite through the earth's magnetic field. This  $\underline{V} \times \underline{B}$  electric field must be subtracted from the measured electric field to get the true electric field. The vector  $\underline{V}$  is the velocity of the spacecraft relative to a frame of reference corotating with the earth. Ideally the spacecraft would measure a three-component electric field vector which could be transformed to GEI coordinates for subtraction of  $\underline{V} \times \underline{B}$  and further analysis. But the measurements along

the Z axis and the X-Y plane have different resolution and reliability. Combining the measurements to obtain a vector in GEI coordinates would contaminate the spin plane data with the interference on the Z axis. Therefore most analysis is done entirely in spacecraft coordinates, where the measurements from the different antennas are kept separate. The  $\underline{V} \times \underline{B}$  electric field is conveniently calculated in the GEI coordinate system from the numbers in the OA data base at NASA/GSFC. The velocity is calculated from orbital parameters, and  $\underline{B}$  is obtained from a model magnetic field rather than magnetometer data.  $\underline{V} \times \underline{B}$  is transformed from GEI coordinates to spacecraft coordinates, then subtracted from the measured values of  $E_x$ ,  $E_y$ , and  $E_z$ .

When the spacecraft is well within the plasmasphere there should be little electric field other than that from  $\underline{V} \times \underline{B}$ , provided that the velocity is calculated relative to a plasma which is assumed to be corotating with the earth. This expected result has provided a way to check the calibration of the instrument with the antennas extended while in orbit.

Just after launch the perigee of DE-1 was over the south pole, so that the spacecraft spent very little time in the plasmasphere at L values less than 4 (on magnetic field lines intersecting the equatorial plane at 4 earth radii). These early data had indicated that the phase angle of the electric field measured in the spin plane was off by a constant amount--of the order of 12 to 16 degrees. By early 1982 the perigee had precessed to the equator, so that there was maximum penetration into the plasmasphere. With a large  $\underline{V} \times \underline{B}$  electric field it was possible to obtain a more accurate calibration check. An analysis of

two orbits 30 days apart indicated that the phase shift is  $16^\circ \pm 1^\circ$ , so the computer code which does the data reduction was fine-tuned accordingly. The constant phase shift has been attributed to the capacitor coupling the antennas to the amplifier. In combination with the input impedance of the amplifier this capacitor forms a high-pass filter, which shifts the phase of a signal with a low frequency. The phase shift, as with the constant DC offset in the amplifiers, appears to be stable over time. A phase shift of  $10^\circ$  is expected from the nominal values of the components in the instrument circuit.

The in-orbit calibration was also used to obtain a modified value for the effective length of the spin plane antenna. Originally a length of 173.1 m was assumed. It was found that the magnitude of the electric field was greater than the  $\underline{V} \times \underline{B}$  field by a factor of 7%. This factor was the same for both amplifier gains, so the effective antenna length used in the calculation was adjusted to a value of  $186 \pm 1$  m. The electric field measured on the Z axis agreed with expected values, within the limits of the offsets introduced by the spacecraft charging interference.

#### Graphical Display of Data

After the numerical analysis has been performed, the results must be displayed in a graphical format which can be easily interpreted. It is most economical to perform the time-consuming analysis once, saving the results for use by different plotting routines. The various plotting programs will often access the same data. Interesting features can be replotted with different scale factors to show the finer details without the need for repeating the calculations.

The primary type of display shows the electric fields measured along the Z axis and in the spin plane, with the  $\underline{V} \times \underline{B}$  electric field subtracted out. A sample graph is shown in Figure 4. The upper plot is from the six second average of electric fields measured along the Z axis. Immediately below it is a plot of the standard deviation. The next two plots,  $E_{\perp}$  and  $E_{\parallel}$ , are the components of the spin plane electric field perpendicular and parallel to the magnetic field vector's projection into the spin plane. At the bottom of the graph is the plot for chi, the error coefficient as calculated by equation (3). All data are plotted as a function of time, with the abscissa marked in units of hours and minutes of universal time (UT). Spacecraft position is given in terms of earth radii (R), magnetic latitude (MLAT), magnetic local time (MLT), and McIlwain L-shell parameter (L).

The perpendicular electric field component is calculated from a vector cross product of the measured field with the magnetic field in the spin plane:

$$\frac{E_{\perp} = E_x B_y - E_y B_x}{|B|} \quad (4)$$

The resulting number is positive if  $E$  cross  $B$  is positive by the "right-hand rule". Since this calculation is done in the spacecraft coordinate system, it is not obvious how  $E_{\perp}$  relates to the electric field in the geographic coordinate system. Figure 5 clarifies this matter. In the northern hemisphere a positive  $E_{\perp}$  is aligned in the direction of the spacecraft motion. In the southern hemisphere it is just the opposite due to the change in sign of the magnetic field.

The parallel component is obtained simply from the inner product:

$$\frac{E_{\parallel} = E_x B_x + E_y B_y}{|B|} \quad (5)$$

One of the objectives of the measurements is to search for parallel electric fields which may be responsible for the acceleration of charged particles in the auroral zones. There are, however, several sources of error which may appear as parallel electric fields which are not real. One cause would be an error in the phase angle adjustment factor which corrects for the instrumental phase shift. An error would cause a truly perpendicular electric field to appear to have a measured parallel component. Likewise, if the electric field has a lot of noise or changes direction rapidly (within 6 seconds) there will be an error in the measured phase angle. In this case chi will be large. Finally, the magnetic field vector may lie at an angle from the spin plane. A convection electric field perpendicular to B may have a component in the spin plane that is parallel to the projection of the magnetic field vector. This possibility is illustrated in Figure 6. If B lies completely in the spin plane this situation cannot occur. As the geomagnetic pole is tilted from the geographic pole by 11° the angle between B and the spin (orbit) plane will vary between 0° and 11° during each day.

There are several instances where fluctuations in the graph of  $E_{\parallel}$  match fluctuations in the graph of  $E_z$  while the graph of  $E_{\perp}$  has a shape of a completely different nature. The ratio of  $E_{\parallel}$  to  $E_z$  is about 1/5.

The variations in  $E_{\parallel}$  due to an East-West (Z axis) electric field component are caused by the offset angle between  $\underline{B}$  and the spin plane. But electric field measurements with the long wire antenna usually translate entirely to perpendicular fields. This verifies that the data reduction technique and the associated coordinate transformations are accurate, as magnetohydrodynamic theory predicts that  $\underline{E}$  should be perpendicular to  $\underline{B}$ .

Electric fields in the auroral zone are expected to have important features which may occur on a size scale much less than the 30 km distance the satellite typically travels in one spin period. The sine wave fit tends to filter out any rapid changes in the electric field which may be important. Likewise, the averaging done on the Z axis data limits both the spatial and time resolution. For this reason a second type of graph which shows peak electric fields is highly useful. An example is shown in Figure 7. The upper plot again shows Z axis data, but with the maximum, minimum, and average fields from each six second period plotted along with the Z component of  $\underline{V} \times \underline{B}$ . The reduction in the noise spikes in the plasmasphere (after 8:25 UT) is easy to see on this type of graph. The lower plot shows the maximum and minimum fields measured with the long wire antenna, along with the spin plane component of  $\underline{V} \times \underline{B}$ . Any errors in the calibration factors or the magnetic field data show up clearly on this type of graph. Likewise, the regions where large and rapid fluctuations in E occur, such as the auroral zones, are easy to spot. An example is the peak near 8:19 UT in Figure 7. This peak does not show up in the processed data in Figure 4.

The change in the 1-bit resolution as the data switches from high-gain to low-gain is evident in the peak field plot at 9:02 UT. But even when the peak lies in the low-gain range (low resolution), the electric field strength obtained with the least square error fit has a much better resolution, since the curve-fitting routine works with high-gain data through most of the spin period.

A third type of graph shows plasma convection velocity (East-West), calculated from the electric field in the spin plane (North-South). An example is shown in Figure 8. The position of DE-1 is plotted in magnetic latitude and magnetic local time coordinates on a polar cap projection. The magnetic latitude is obtained from the spacecraft's location through a transformation from the geographic coordinates to a geomagnetic coordinate system. The magnetic local time is obtained directly from the NASA/GSFC OA data base. The plasma convection velocity is drawn as a vector perpendicular to the orbit plane. The vector U is calculated from:

$$\underline{U} = (\underline{E} \times \underline{B})/B^2 \quad (6)$$

The lengths of the convection vectors on the graph are proportional to the total magnitude of the vector thus calculated, rather than just the length of a projection of U into the equatorial plane. But the directions of the vectors in the figure are obtained by transforming U into GEI coordinates. From these coordinates the angle between U and the sun vector in the equatorial plane is calculated. The convection vectors are drawn at the same angle with respect to the line connecting

the origin and 12 HRS MLT. The convection plots thus obtained from the DE-1 electric field data in general agree with the well-established pattern of anti-sunward flow over the polar cap and sunward flow at lower latitudes [Stern, 1977]. The plot in Figure 8 is a classic example. But irregular features are often observed in the convection plots; these will be discussed in Chapter IV.

The convection plots generated for the times when DE-1 is above  $3 R_E$  do not turn out well for a number of reasons. The spacecraft is moving slower at the high altitude, so successive data points on the plot get blurred together. The magnitude of the magnetic field is very small, so fluctuations in E are magnified through the division by B in equation (6). The electric fields are small, only several mV/m, and rapid fluctuations within one spin period produce a high error coefficient in the data fitting.

CHAPTER IV  
POLAR CAP PLASMA CONVECTION

Previous Results

The phenomena of large-scale convection of plasma in the magnetosphere is well-established. The general pattern is that of a two-cell circulation, with anti-sunward flow over the polar cap and sunward flow at lower latitudes. From the interaction of this flow with the magnetic field of the earth, there is a dawn to dusk electric field over the polar cap. In the auroral zones the electric field is oppositely directed, pointing poleward in the evening zone and equatorward in the morning zone.

According to Axford and Hines [1961] the source of the convection is a "viscous-like interaction" between magnetospheric plasma and the solar wind. At the boundary of the magnetosphere the flow is in the direction of the solar wind, and closer to the earth there is a return flow toward the sun. In this view the convective flow is the primary phenomenon and the electric field is the by-product.

An alternative model proposed by Dungey [1961] views the electric field as the primary phenomenon. The field is produced by the flow of the solar wind through "open" magnetic field lines extending from the poles into interplanetary space. The electric field is "mapped" down to low altitudes along the magnetic field lines, which are equipotential

surfaces. Over the poles this field drives the anti-sunward convection; the return flow on closed magnetic field lines is a secondary consequence due to continuity in the plasma flow and electric field.

It is known that there is a high correlation between magnetic activity and the north-south component,  $B_z$ , of the interplanetary magnetic field (IMF). This lends support to the model of an open magnetosphere. Likewise, it is expected that the strength of the magnetospheric convection is influenced by the polarity of the IMF [Block, 1973]. A southward IMF should enhance the convection.

The earliest confirmation of the two-lobbed convection pattern by satellite measurement of the electric field was obtained with the Injun 5 spacecraft [Cauffman and Gurnett, 1971]. It is noted that the double-cell pattern represents "a gross simplification of the actual convection, which is often chaotic or turbulent, and variable in time" [Cauffman and Gurnett, 1972]. The Injun 5 data did not reveal a statistically significant relationship between convection magnitude and magnetic activity. It was found that convection magnitudes are often greatest near the reversals, with average velocities of 1.5 km/s. Over the polar region the anti-sunward convection was usually less than 0.75 km/s.

More accurate and continuous measurements were obtained with the OGO 6 probes, but only for a period of about 2 weeks. Contrary to expectations, it was found that the general electric field pattern is not highly variable, even during substorms [Heppner, 1972a]. A correlation was found between substorms and electric fields occurring with a relatively small time and spatial extent, but Heppner pointed out

that there isn't necessarily a direct cause and effect relationship. A dawn-dusk asymmetry in the convection patterns were found to be correlated with the  $B_y$  component of the IMF [Heppner, 1972b]. The north-south component of the IMF appears to have been ignored in this paper. From the OGO 6 data empirical models of the polar cap potentials were derived to fit various patterns seen in the electric field [Heppner, 1977]. Examples are shown in Figure 9. Note in Figure 9b the distortion in the two-cell pattern, required to explain multiple reversals seen in the evening auroral zone.

Plasma convection in the ionosphere has also been measured with incoherent scatter radar. These observations have also led to the conclusion that the two-cell convection is not greatly perturbed, but expands equatorward and that velocities are enhanced in response to substorms [Foster et al., 1981].

All of these measurements were obtained at relatively low altitudes. The Injun 5 spacecraft orbited in the range of 680 km to 2530 km altitude, and OGO 6 measured fields from 400 km to 1100 km. As noted earlier, the DE-1 orbit is highly elliptical, with an altitude range of 675 to 23,400 km, so this spacecraft has the opportunity to measure electric fields in unexplored territory.

#### DE-1 Results

Science operations on the DE-1 spacecraft began in October of 1981, after a month-long sequence of attitude adjustment and instrument activation. At this time orbit apogee was over the north pole and perigee was over the south pole. This enabled the observation of con-

vection in the southern hemisphere during the initial months of operation.

The limited amount of data processed so far have indicated that the convection can be highly irregular in structure. Only on rare occasions is an undisturbed two-cell pattern seen. Significant changes occur from day to day, and even from one orbit to the next (the orbital period is about 7 hours). At the times for which interplanetary magnetic field data are available the evidence supports the view that a southward IMF produces a strong convective flow. Correlation with indices of geomagnetic activity is weaker. Dips in the hourly equatorial  $D_{st}$  index appear to correlate better than the three hour  $K_p$  index. Enhanced polar convection seen at times of high geomagnetic activity may be a coincidence due to the fact that substorms usually occur when the Z component of the IMF is negative.

Figure 8 shows a convection plot from day 81343. (This notation refers to the 343rd day, December 9, of the year 1981.) Plots of  $B_z$ ,  $D_{st}$ , and  $K_p$  for day 81343 are in Figure 10. Preceeding the time of the measurement in Figure 8,  $B_z$  was negative and  $D_{st}$  had dropped slightly, which is indicative of an increase in the extraterrestrial ring current. At the time of the measurement,  $B_z$  turned positive. It is reasonable to expect a time delay between changes in the IMF, as measured with spacecraft orbiting beyond the bow shock, and the effects seen in the near-earth magnetosphere.

The variability in the convection is illustrated in the graphs from three consecutive orbits shown in Figures 11 to 13. Figure 14 contains the geomagnetic indices and IMF data for this period. The anti-sunward

flow over the polar cap is irregular in Figures 11 and 12. During this time from 5 to 15 hours UT on day 81287 both the  $K_p$  and  $D_{st}$  indices were recovering from levels indicative of a high disturbance in the geomagnetic field. From 16 to 24 hours UT  $K_p$  steadily increased from 3+ to 6- coincident with a southward turning of the IMF. At 22:00 UT the convection flow in Figure 13 is seen to be enhanced.

Another sequence of plots spanning the period from day 81294 (Oct. 21, 1981) to day 81298 (Oct. 25, 1981) is presented in Figures 15 through 21. There is no IMF data available for this period, but some correlations can be made with the magnetic activity, given in Figure 22. At the time when the data in Figure 15 were obtained, the magnetic activity is high. The convection is fairly uniform with the exception of the reversal at  $65^\circ - 72^\circ$  MLAT in the evening sector. This type of pattern agrees with Heppner's model in Figure 9b. In Figure 16 there is no large-scale pattern in the convective flow. There are localized regions where a strong flow occurs in one direction then reverses. These are most likely associated with field-aligned currents as described in the next chapter. Figure 17 indicates almost no convection;  $K_p$  reached a low of 2+ during this time. One orbit later, in Figure 18, the familiar pattern is seen. The  $D_{st}$  index had dipped slightly and  $K_p$  was on the rise. On the next day the flow is weak and the region of anti-sunward flow has expanded, as shown in Figure 19. One orbit later (Figure 20) the convection has become erratic. The features at  $50^\circ$  to  $75^\circ$  MLAT in the evening sector in Figure 19 appear to have "evolved" to the pattern seen in Figure 20. Figure 21 again shows a two-cell convective flow at the same time that the  $D_{st}$

index takes a dip. The largest convection magnitude is seen just equatorward of the reversals. A component over 2 km/s occurs at one point. This agrees with the trend seen in the Injun 5 data [Cauffman and Gurnett, 1972].

The best plasma flow pattern seen in the data processed to date is shown in Figure 23. These data were obtained on day 81364 (Dec. 30, 1981). The geomagnetic and IMF data for this day are displayed in Figure 24. Preceeding the pass of DE-1 over the pole, the  $D_{st}$  index had dropped to -80 gammas coincident with a southward turn in the interplanetary magnetic field. The  $K_p$  index at this time was 4-indicating moderate magnetic activity. Since there are several cases where  $K_p$  is much higher while the convective flow is weaker, there does not appear to be a direct link between the two.

There is a relationship between features on the convection graphs and patterns in the plasma wave spectrograms obtained with the Plasma Wave Instrument. The regions of sunward flow usually have intense, right-hand polarized, whistler-mode radiation at frequencies of 300 Hz to 20 kHz. The region of anti-sunward flow is very quiet. In contrast, at the point where the reversal occurs there is often a noise burst at all frequencies from 1 Hz up to 400 kHz. Although the noise spans the frequency range, the wave energy peaks below 60 Hz. This is consistent with "velocity shear driven plasma turbulence" detected with the Hawkeye 1 spacecraft [Kintner, 1976]. The turbulence is indicated by both electric and magnetic fluctuations which do not propagate from the source. The high frequency components, however, do not agree with Kinter's observations. Phase measurements with the DE-1 PWI indicate

that the components above 100 Hz are sometimes well correlated, with a right-polarized mode. To add to the confusion, the noise bursts are often found well within the region of sunward plasma flow at the points where the electric field reaches a peak. Examples are presented in Chapter V.

CHAPTER V  
AURORAL ZONE ELECTRIC FIELDS

Previous Results

The precise nature of the relationship between the aurora and magnetospheric electric fields has yet to be determined. From the Injun 5 data it was established that the electric field reversals occur in the auroral zone, at invariant latitudes of  $60^{\circ}$  to  $80^{\circ}$  [Cauffman and Gurnett, 1972]. The reversal is considered to occur at the boundary between open and closed magnetic field lines. It was noted by Frank and Gurnett [1971] that this boundary is coincident with the energetic electron ( $E > 45$  kev) trapping boundary. Furthermore, the reversals were found to be associated with "inverted V" electron precipitation events, so called because of a characteristic shape in graphs of electron energy vs. time. The electron precipitation involves a considerable field-aligned "Birkeland" current. In the neighborhood of the "inverted V" events the electric field had large ( $125$  mV/m) and irregular fluctuations, often consisting of distinct pairs of oppositely directed spikes [Gurnett, 1972].

With the S3-3 satellite, Mozer et al. [1977] have observed oppositely directed, perpendicular electric fields of a similar nature but with a much larger magnitude ( $>400$  mV/m). Large parallel electric field components over  $400$  mV/m were found between the "paired electrostatic shocks". Other instruments on S3-3 identified magnetic

field-aligned currents and extreme plasma turbulence in the regions of the shocks. Mozer identified the wave turbulence as electrostatic ion cyclotron waves.

The S3-3 satellite had provided measurements at altitudes from about 260 km to the satellite apogee at 8000 km. A quasi-static electric field experiment on the ISEE-1 satellite has measured electrostatic shock "events" at geocentric distances between 2.9 and  $6.5 R_e$  [Mozer, 1980]. In this paper, "an 'event' was defined as an interval of  $> 10$  Hz electric field turbulence within which the quasi-static electric field magnitude somewhere exceeded about 100 mV/m". Mozer argues that "the duration and field strengths of these events suggest that the auroral particle acceleration region is confined to altitudes less than a few  $R_e$  and that the highest altitude observations are due to mapping of electric fields from the acceleration region to the point of observation" [1980].

A different view of a qualitatively similar phenomenon is given by Burk, Silevitch, and Hardy [1982]. Their analysis is based on data from the S3-2 satellite flying at altitudes of 240 km to 1557 km. They characterize the events as "small-scale auroral vortices", marked by large deflections in the east-west magnetic field component measured on the spacecraft, indicative of downward and upward current sheets, which are also observed in the particle spectra. In the region between current sheets the electric field rotated by  $180^\circ$  then returned to the original orientation. The magnitude of the fields can exceed 200 mV/m. The plasma flow is viewed as having "two vortices with clockwise and

counterclockwise rotations around the positively and negatively charged flux tubes, respectively".

#### DE-1 Results

The DE-1 measurements of auroral zone electric fields both reaffirm some of the previous observations and introduce some new questions. Electric fields with the general character of an "electrostatic shock" are seen, but none have ever been observed with the large magnitudes reported by Mozer. The electric fields detected with the DE-1 long wire antenna never exceed 200 mV/m in the cases processed to date.

One case of a shock-like event is shown in Figure 25. These data are from a time when DE-1 was in the northern hemisphere at an invariant latitude of  $65.3^\circ$  and altitude of 9,000 km (2.42 Re). At 3:45:02 UT (28 seconds from start of plot), there is an electric field of 90 mV/m. After the antenna rotates  $180^\circ$  there is a field with the same sign at a magnitude of 160 mV/m. This field is pointing in the opposite direction from the one encountered 3 seconds earlier. The separation is 16 km as the satellite was moving 5.46 km/s. At this time DE-1 was directly on a magnetic field line connected with a source of auroral hiss. This is determined from the plasma wave frequency-time spectrogram which shows a "funnel-shaped" feature centered on the event. This type of spectral feature is explained by Gurnett et al. [1983]. The funnel shape is "a propagation effect caused by a frequency dependence beaming of the whistler mode radiation along the magnetic field." It is indicative that the source of the auroral hiss was located a distance below the spacecraft.

At lower altitudes events consistent with the "auroral vortex" theory are often seen. As mentioned before, the plasma convection velocity often has the largest magnitude near the reversals, usually in the sunward flowing regions. The PWI spectrograms show broadband noise at these events. The electric field looks as if a perturbation had been added to the uniform convection field. The perturbation field consists of oppositely directed fields. The data from the magnetometer on DE-1 indicate that these fields are associated with field-aligned currents. A similar correlation between the electric and magnetic fields is seen on the DE-2 satellite [Sugiura et al., 1982].

The best examples of vortices are found near the cusp. One case is shown in Figure 26. The peak near  $64^\circ$  MLAT on the convection graph occurred at 15:27:40 UT on day 82092. Figure 27 shows high-resolution data where the electric field measured in the spin-plane reaches a peak then reverses. The field along the spacecraft Z axis also shows a large variation at this point, of the order of 350 mV/m. As the magnetic field is co-planar with the spin-plane and perpendicular to the Z axis, this indicates that the electric field is rotating around in a plane perpendicular to B. Summary data from the DE-1 magnetometer shows a perturbation of 500 nT in the east-west magnetic field due to field-aligned currents. Figure 28 contains the plasma wave spectrogram for this time. The broadband noise burst is clearly visible. This plot also shows the relatively quiet region where the plasma flow is antisunward before 15:25 UT, and the occurrence of whistler-mode radiation in the sunward flowing plasma after 15:25 UT.

A very interesting case was found in the southern hemisphere 16 days later. (By this time in 1982 the orbit had precessed such that perigee was near the equator and both poles were crossed at roughly equal altitudes.) Figures 29 and 30 show a convection plot and spectrogram containing two events of interest. The noise burst at 22:09 UT corresponds to the peak in the morning sector. There is a pair of opposing electric fields in the evening sector at 22:24 UT corresponding to another broadband line in the spectrogram. The DC electric field reaches 140 mV/m in this event.

The plasma waves have both electric and magnetic components. The narrow vertical shapes on the frequency-time spectrograms indicate that the disturbances are highly localized on specific field lines. In the event of 22:09 UT on day 82108 (Figure 30), the DE-1 spacecraft, at a distance of  $1.5 R_E$ , must have been very close to the source region. The same is true of the case shown in Figure 28, but some spread is seen in the spectrogram above 10 KHz. There is a greater spread at the second event in Figure 30. These are of the same nature as the "funnel shapes" encountered when DE-1 is at distances above  $2 R_E$  [Gurnett et al., 1983] but the components above 100 KHz were never seen at the greater distances. The components above 100 Hz are usually correlated, with a right-polarized mode.

The mechanism by which the noise bursts are generated has yet to be determined. One possibility is the current driven ion cyclotron instability associated with non-uniform magnetic shear. More work needs to be done to see if the observations are consistent with a theory described by Bakshi et al. [1983].

## CHAPTER VI

## STABLE AURORAL RED ARCS

Previous Results

Stable auroral red (SAR) arcs generally occur at mid-latitudes during geomagnetic storms. These arcs are unusual in that they occur well equatorward of the auroral zone and their intensity does not vary greatly with time. The light from these arcs is from the red 630 nm emission line of atomic oxygen, at subvisual intensities. The emission occurs at an altitude of about 400 km. A review of the characteristics of SAR arcs is given by Rees and Roble [1975]. It is known that the arcs occur on magnetic field lines connected with the plasmapause region. Satellite measurements have found that in the region of SAR arc emission there is a depression in the electron density and an enhancement in the electron temperature. Collisions between atomic oxygen and electrons with energy greater than 2 eV excite the atoms which produce the 630 nm radiation.

It has been proposed that perpendicular electric fields could produce an SAR arc by providing the energy to heat the electrons. Rees and Roble [1975] discount this hypothesis on the basis of their own theoretical calculations. Additionally, electric fields had previously never been observed in SAR arcs.

DE-1 Results

The DE-1 data had indicated the occasional presence of stable, large-scale electric fields at low invariant latitudes. On the basis of information provided by Nagy and Kozyra [private communication, 1982] it has been found that these unusual fields are found on magnetic field lines coincident with reported SAR arcs. Several cases have been found. The electric fields have a very distinct character. An example is given in Figure 31, from day 81293. After the pass through the auroral zone, where the electric field is fairly noisy, a very smooth perpendicular field is encountered at 14:09 UT. The field reaches a peak of 27 mV/m after 14:11 UT, then drops off abruptly. An SAR arc was detected by ground-based photometers on the same day at the same invariant latitude ( $53^\circ$ ) where the electric field reaches the peak. The plasma convection associated with the peak field is about 8 km/s, directed westward, opposite to corotation. This occurs on an L shell which is normally considered to be well within the corotating plasmasphere. The long "tail" on the electric field plot extending to 14:20 UT is indicative that the plasmasphere is "slipping". It is an artifact of the  $\underline{V} \times \underline{B}$  calculation in which the spacecraft velocity is relative to a corotating frame of reference. The plasma observed by the spacecraft from 14:12 UT to 14:20 UT is gradually speeding up to match corotation as the spacecraft moves in to lower L values. This particular event is associated with a magnetic substorm which started 6 hours prior to the observation, at which time the  $K_p$  index was 7-.

The Vector Electric Field Instrument (VEFI) on the low-altitude DE-2 spacecraft measured a similar electric field on nearly coincident

magnetic field lines. This instrument is described by Maynard et al. [1981]. The magnitude measured with VEFI was much higher due to magnetic field line convergence at lower altitudes. Data provided by N. Maynard of NASA/GSFC is shown in Figure 32. DE-2 was in the southern hemisphere moving toward a higher invariant latitude as time increases, so the electric field is almost a mirror image of the graph in Figure 31. The ratio of the electric field magnitudes measured with DE-1 and DE-2 is found to be in agreement with the equation:

$$\frac{E_1}{E_2} = \left( \frac{R_2}{R_1} \right)^{3/2} \quad (7)$$

This is an approximate equation for the electric fields found at different radial distances on the same magnetic field line. This equation is based on the assumption that the field lines are equipotentials.

According to Maynard the langmuir probe on DE-2 had measured an increase in the electron temperature and a decrease in the electron density coincident with the peak in the electric field measured with VEFI [DE Science Team meeting, Feb. 1983]. This is consistent with the characteristics of SAR arcs mentioned before [Rees and Roble, 1975]. The DE-1 PWI spectrograms usually show the presence of intensified VLF plasmaspheric hiss where the large electric fields are encountered, indicative of an elevated electron temperature.

The type of electric field and plasma convection described here has been observed with other spacecraft. Spiro et al. [1979] refer to the phenomena as sub-auroral ion drift (SAID) in a report on AE-C ion drift measurements. Maynard et al. (1980) saw a case in the ISEE-1 electric field data. The SAID events occur predominately in the local time sector between 18:00 hrs and 2:00 hrs. Their occurrence is associated with magnetic substorms, but no previous connection has been made with SAR arcs. The SAID events are in agreement with a modeling of substorms by Harel et al. [1980a,b] and Spiro et al. [1980].

Even though large electric fields are found coincident with SAR arcs, it is not conclusive that the fields are directly responsible for producing the arcs. There are times when no electric fields were seen when DE-1 was on magnetic field lines on which SAR arcs were observed on the ground. One such case is the SAR arc event described by Kozyra et al. [1982]. The SAR arcs also have a nearly global longitudinal extent, whereas the SAID events are confined to locations around 21:00 hrs local time. The relationship between the SAR arcs and SAID is most likely that both occur on the edge of the plasmaphere when it moves inward during magnetic substorms.

## CHAPTER VII

### DISCUSSION

The analysis of the DC electric field data from DE-1 is obviously not a trivial task. Considerable time was spent over a nine month period in developing the computer programs which convert the data from digital bits to graphic displays. Every step of the development had to be checked carefully to insure that the intermediate results were consistent with the input data. Several plotting programs are required to display the data in different formats, such as peak electric fields or calculated convection velocity component. In addition utility programs were required for such tasks as listing on a printer the data and orbital information for specific time periods. Program efficiency was also a consideration, since it takes one hour of computer time to process 12 hours of real-time data. Once the main analysis program was known to be functioning correctly it was completely restructured in order to obtain a 3:1 increase in efficiency. (This included the elimination of a time-consuming printout of every computed value, required in the early stages for diagnostic purposes.)

The results obtained so far are consistent with previous electric field measurements. But the data have always yielded new information due to the excellent sensitivity of the long wire antenna and the unique orbit of the spacecraft.

The convection graphs are very useful in understanding various magnetospheric processes, such as the merging of the earth's magnetic field with the interplanetary field carried by the solar wind. But due to the complexity of the situation a statistically significant number of cases must be collected before definite conclusions can be reached.

Numerous auroral passes have been collected in the data base. Since the mechanism by which the aurora are produced is not completely understood there is opportunity for making new discoveries. Information about the electric fields is of vital importance, but simultaneous data from other instruments is required. A comprehensive analysis is beyond the intent of this paper, but observations reported in Chapter V could form the basis of such an investigation. Of particular interest are the plasma waves found coincident with the oppositely directed DC electric fields on auroral field lines.

The subauroral ion drift phenomenon had been detected before, but previously there had been no connection with SAR arcs. A direct cause and effect relationship may not even exist. This subject is currently under investigation in collaboration with scientists at the University of Michigan Space Physics Research Laboratory. The identical patterns seen in both the DE-1 and DE-2 electric field data at a magnetic conjunction verify that the analysis techniques are correct.

## CHAPTER VIII

## CONCLUSIONS

The short tubular electric antenna on DE-1 has been of limited use for DC electric field measurements due to the interference which masks the true field values. In the plasmasphere, where the plasma density is higher, the interference is highly attenuated and the measured field matches the calculated  $\mathbf{V} \times \mathbf{B}$  field fairly well. On occasion, there will be changes detected with the short antenna which match features in the spin plane data. The measurement along the spin axis then gives an indication of the three dimensional structure of the electric field.

In contrast, the long wire antenna has provided excellent data on the electric field in the spacecraft spin plane. The magnitude of the field can be determined to within 0.42 mV/m. The spatial and time resolution is limited by the 6 second rotational period. For most of the electric field phenomenon observed, this hasn't been highly detrimental.

Measurements of the polar cap plasma convection patterns have been very illuminating. Significant changes occur from one day to the next, and even on successive spacecraft orbits there are large variations. This indicates that the convective flow is not a constant steady-state but is influenced greatly by outside forces. There is not a direct

correlation between geomagnetic activity and the strength or uniformity of the polar cap plasma convection. The most important factor appears to be the polarity of the north-south component of the interplanetary magnetic field. A southward IMF produces a distinct two-cell convection pattern. This supports the theory of an "open" magnetosphere with the field lines in the polar regions merging with the interplanetary field. The electric field in the solar wind is connected to the ionospheric plasma along the open field lines.

At times a two-cell convective flow is not seen. Then the passes over the polar cap are characterized by localized regions of rapid flow. Even when the two-cell pattern is seen, there are enhancements to the electric field near the boundary between sunward plasma flow and antisunward flow. The peaks in the electric field often occur in pairs pointing in opposite directions. Magnetometer data indicate that these events are associated with field aligned currents which produce a vortex in the plasma flow. When only one peak is seen in the electric field, it may be because the path of the spacecraft through the region did not intercept both peaks. Coincident with the field aligned current events, the plasma wave instrument detects the presence of intense plasma wave oscillations. The disturbances have both electric and magnetic components, sometimes with a definite right circular polarization. It occurs at a wide range of frequencies from 1 Hz up to over 300 kHz. The source region of the plasma oscillations is found at a radial distance of  $1.5 R_e$ .

The oppositely directed electric fields seen in the DE-1 data are consistent in character with similar events previously reported in the

literature. The field reversals occur on a region 10 to 30 km across. But the magnitudes measured with DE-1 are not as large as previously reported by Mozer et al. [1977]. This could be due to a difference in the response of the instruments to rapid changes in the DC field. But it is possible that as more DE-1 data is processed electric fields will be found with magnitudes greater than 200 mV/m.

A correlation has been found between unusual low-latitude electric fields and SAR arcs. The electric field corresponds to a plasma flow directed opposite to corotation. As this phenomenon had previously been discovered with ion drift detectors it had been given the name "subauroral ion drift". The boundary region between the corotating plasma and the SAID contains plasma which is virtually standing still in the inertial (GEI) reference frame. The peak in the electric field or plasma flow is found to be on SAR arc field lines. The exact mechanism by which the SAR arcs are produced is yet to be determined. The electric field could be responsible for heating the electrons which produce the arcs. Electrons accelerated by the electric field would be heated by collisions in the ionosphere. But the fact that the arcs can occur without the electric field adds to the mystery.

## REFERENCES

- Axford, W. I., and C. D. Hines, A unifying theory of high-latitude geophysical phenomena and geomagnetic storms, Can. J. Phys., 39, 1433, 1961.
- Bakshi, P., and G. Ganguli, and Palmadesso, Finite width currents, non-uniform magnetic shear and the current driver ion cyclotron instability, NRL Memorandum Report 5034, 1983.
- Block, L. P., The Magnetosphere, Ch. 8, Cosmical Geophysics, Scandinavian University Books, 1973.
- Burke, W. J., M. Silevitch, and D. A. Hardy, Observations of small-scale auroral vortices by the S3-2 satellite, 1982 preprint.
- Cauffman, D. P., and D. A. Gurnett, Double-probe measurements of convection electric fields with the Injun-5 satellite, J. Geophys. Res., 76, 6014-6027, 1971.
- Cauffman, D. P., and D. A. Gurnett, Satellite measurements of high latitude convection electric fields, Space Science Reviews, 13, 369-410, 1972.
- Dungey, J. W., Interplanetary magnetic field and the auroral zones, Phys. Rev. Lett., 6, 47-48, 1961.
- Fahleson, U., Theory of electric field measurements conducted in the magnetosphere with electric probes, Space Science Reviews, 7, 238-262, 1967.
- Foster, J. C., J. R. Dovpnito, and G. S. Stiles, Large scale patterns of auroral ionospheric convection observed with the chatanika radar, J. Geophys. Res., 86, 11, 357, 1981.
- Frank, L. A., and D. A. Gurnett, Distributions of plasmas and electric fields over the auroral zones and polar caps, J. Geophys. Res., 76, 6829, 1971.
- Gurnett, D. A., Electric field and plasma observations in the magnetosphere, proceedings of the symposium jointly sponsored by COSPAR, IAGA, and URSI, 11-13 May 1972, p. 123-138.

Gurnett, D. A., S. D. Shawhan, and R. R. Shaw, Auroral hiss z-mode radiation and auroral kilometric radiation in the polar magnetosphere: DE-1 observations, J. Geophys. Res., 88, 329-340, 1983.

Harel, M., R. A. Wolf, P. H. Reiffe, R. W. Spiro, W. J. Burke, F. J. Rich, and M. Smiddy, Quantitative simulation of a magnetospheric substorm, I. model logic and overview, J. Geophys. Res., 86, 2217, 1981.

Heppner, J. P., Electric field variations during substorms: Ogo-6 measurements, Planet Space Sci., 20, 1475, 1972a.

Heppner, J. P., Polar-cap electric field distributions related to the interplanetary magnetic field direction, J. Geophys. Res., 77, 4877, 1972b.

Heppner, J. P., Empirical models of high-latitude electric fields, J. Geophys. Res., 82, 1115, 1977.

Hoffman, R. A., and E. R. Schmerling, Dynamics Explorer program: an overview, Space Sci. Instr., 5, 345, 1981a.

Hoffman, R. A., G. D. Hogan, and R. C. Maehl, Dynamics Explorer spacecraft and ground operations systems, Space Sci. Instr., 5, 349, 1981b.

Kintner, P. M., Observations of velocity shear driven plasma turbulence, J. Geophys. Res., 81, 5114, 1976.

Kozyra, J. U., T. E. Cravens, A. F. Nagy, M. O. Chandler, L. H. Brace, N. C. Maynard, D. W. Slater, B. A. Emery, and S. D. Shawhan, Characteristics of a stable auroral red arc event, Geophys. Res. Lett., 9, 973-976, 1982.

Maynard, N. C., T. L. Aggson, and J. P. Heppner, Magnetospheric observations of large subauroral electric fields, Geophys. Res. Lett., 7, 881, 1980.

Maynard, N. C., E. A. Bielecki, and H. F. Burdick, Instrumentation for vector electric field measurements from DE-B, Space Science Instr., 5, 523-534, 1981.

Mozer, F. S., ISEE-1 observations of electrostatic shocks on auroral zone field lines between 2.5 and 7 earth radii, University of California preprint, 1980.

Mozer, F. S., C. W. Carlson, M. K. Hudson, R. B. Torbert, B. Parady, and J. Yatteau, Observations of paired electrostatic shocks in the polar magnetosphere, Phys. Rev. Lett., 38, 292, 1977.

Rees, M. H. and R. G. Roble, Observations and theory of the formation of stable auroral red arcs, Rev. Geophys. and Space Physics, 13, 201, 1975.

Shawhan, S. D., and D. A. Gurnett, D. A. Odem, R. A. Helliwell, and Chung G. Park, The plasma wave instrument and quasi-state electric field instrument (PWI) for Dynamics Explorer-A., Space Sci. Instru., 5, 535, 1981.

Smith, P. H., C. H. Freeman, and R. A. Hoffman, Dynamic Explorer science data processing system, Space Science Instru., 5, 561-573, 1981.

Spiro, R. W., R. A. Heelio, and W. B. Hanson, Rapid subauroral ion drifts observed by Atmospherere Explorer C, Geophys. Res. Lett., 6, 657, 1979.

Spiro, R. W., and M. Harel, R. A. Wolf, and P. H. Reiff, Quantitative simulation of a magnetospheric substorm, 3. Plasmaspheric electric fields and evolution of the plasmapause, J. Geophys. Res., 86, 2261, 1981.

Stern, D. P., Large-scale electric fields in the earth's magnetosphere, Rev. Geophys. and Space Phys., 15, 156, 1977.

Sugiura, M., N. C. Maynard, W. H. Farthing, J. P. Heppner, B. G. Ledley, and L. J. Cahill, Initial results on the correlation between the magnetic and electric fields observed from the DE-2 satellite in the field-aligned current regions, Geophys. Res. Lett., 9, 985, 1982.

**APPENDIX A:****TABLES**

TABLE 1

Characteristics of the Electric Field Sensors in the Plasma Wave  
 Instrument on the Dynamics Explorer-1 Spacecraft

	Effective DC Antenna Length	Amplifier Gain	Full Scale Electric Field	Digital Resolution
E <sub>z</sub> Low Gain		0.178	1.8 V/m	14 mV/m
	8 m			
E <sub>z</sub> High Gain		1.78	180 mV/m	1.4 mV/m
<hr/>				
E <sub>x</sub> Low Gain				
Design	173.1 m		2.38 V/m	19 mV/m
		0.0062		
Calibrated	186 m		2.22 V/m	17.3 mV/m
<hr/>				
E <sub>x</sub> High Gain				
Design	173.1 m		58 mV/m	0.45 mV/m
		0.254		
Calibrated	186 m		54 mV/m	0.42 mV/m

**APPENDIX B****FIGURES**

Figure 1

Graph of electric field strengths measured along the spacecraft Z axis and X axis. The data shown spans a 72 second period. On this time scale, the sine wave modulation on the X axis is clearly visible. The modulation is due to the rotation of the spacecraft once every six seconds. The Z axis data also shows a spin modulation which should not be present, as the probes are parallel to the spin axis.

A-683-294

UNIVERSITY OF IOWA  
DE-1 PLASMA WAVE INSTRUMENT      DC ELECTRIC FIELD  
ORBIT 281      DAY 81295      UT 14: 8:12 - 14: 9:24

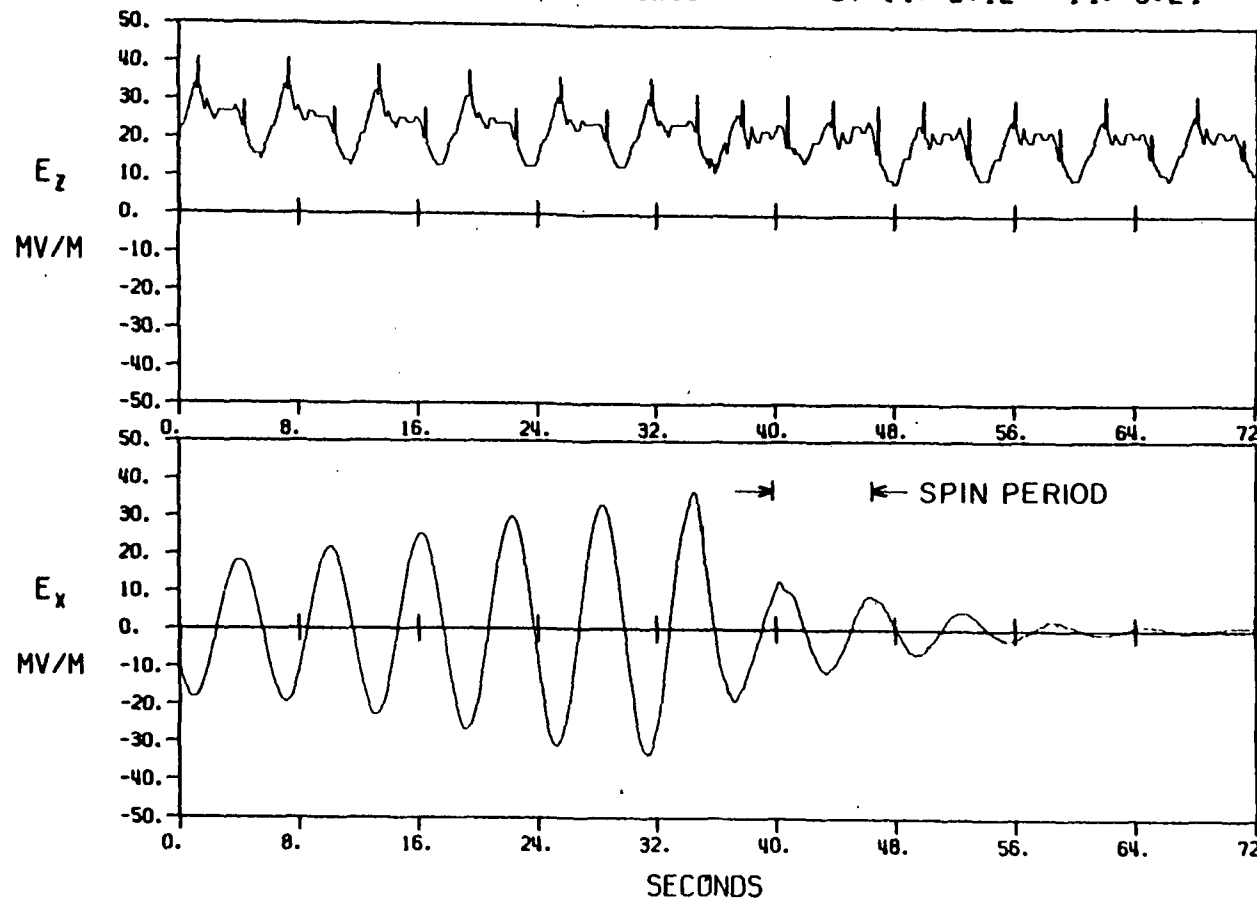


Figure 1

Figure 2

Location of the long wire electric field probes on the DE-1 spacecraft. Due to the  $15^\circ$  offset between the probes and the Y axis, there should be a  $165^\circ$  lag between the time at which the +Y axis is pointing to earth center and the time at which the electric field is being measured in the same direction.

A-683-171

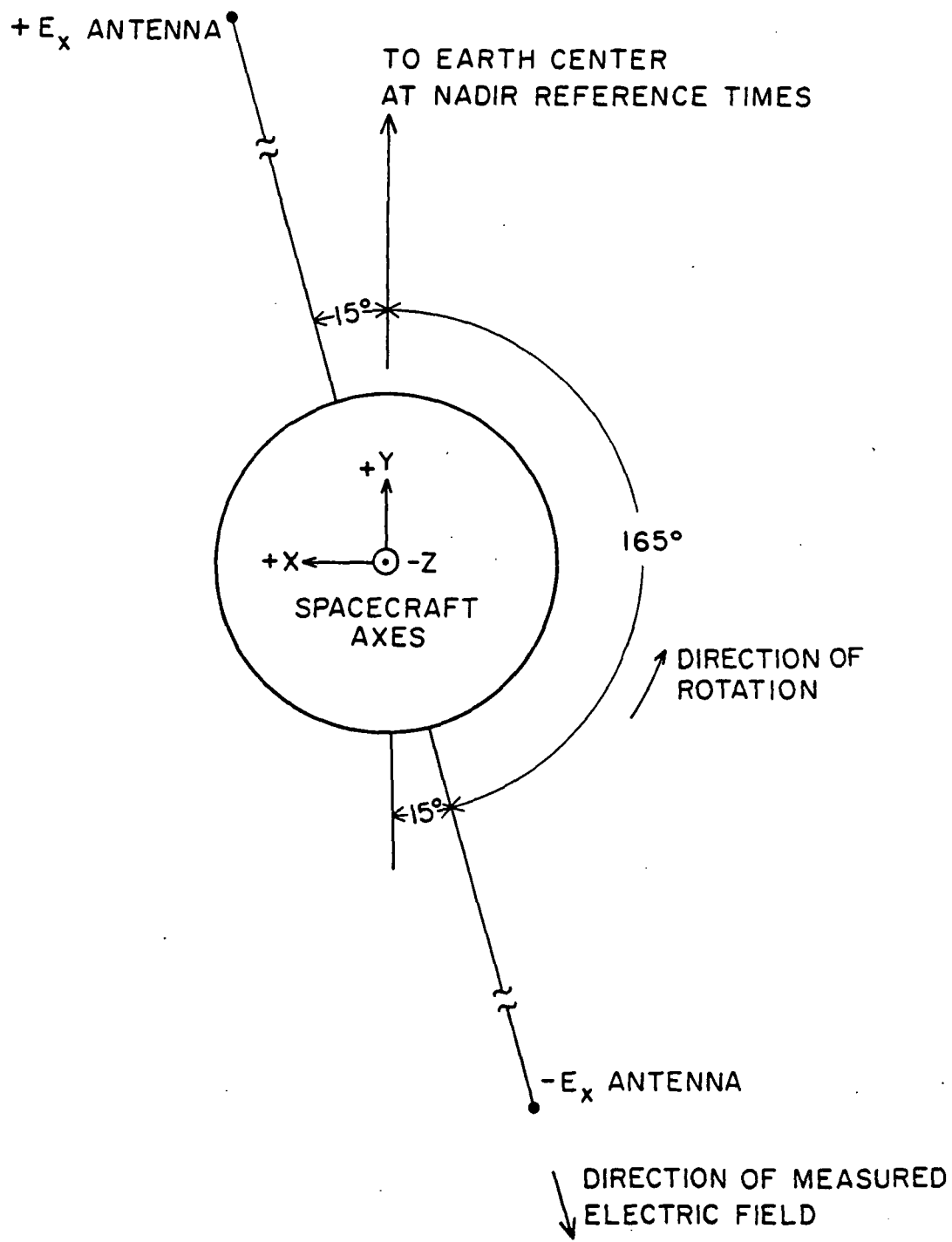


Figure 2

**Figure 3**

Illustration of the time relationship between successive data records and each measurement. The data is grouped into records spanning 8 seconds of time. The analysis is performed on segments of data spanning 6 seconds of time, with a 2 second overlap between adjacent segments. This results in measurements spaced 4 seconds apart, or two per data record.

A - G83 - 172

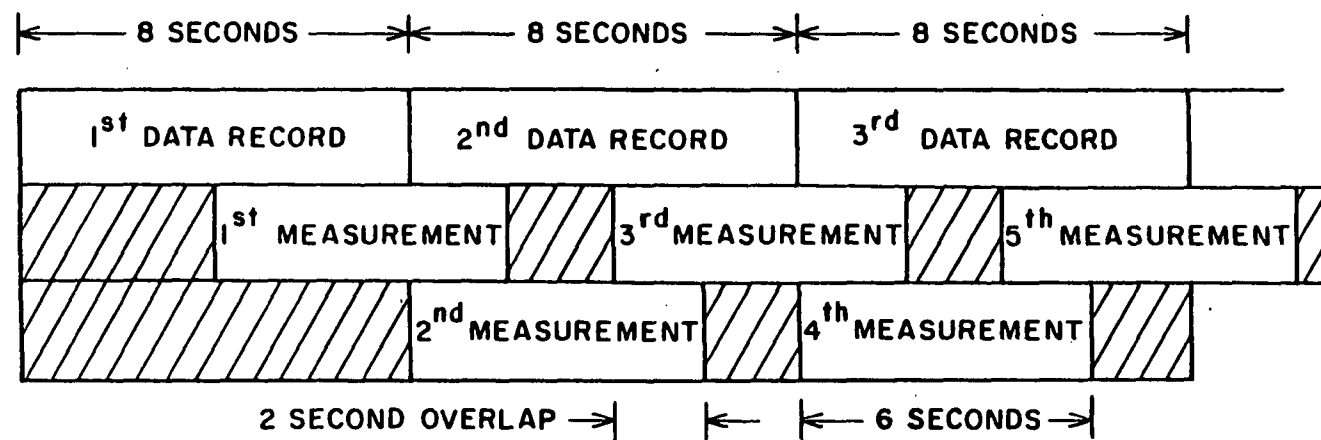


Figure 3

Figure 4            Graph of electric field data after computer processing. The data covers a time period of 80 minutes. The top plot shows the average Z axis electric field. Below that is the standard deviation calculated for each average value of  $E_z$ . The next two plots show the components of the spin plane electric field perpendicular and parallel to the magnetic field in the spin plane. The bottom plot is the chi error coefficient for the spin plane measurements.

UNIVERSITY OF IOWA  
DE-1 PLASMA WAVE INSTRUMENT

DC ELECTRIC FIELD  
ORBIT 522  
DAY 81364

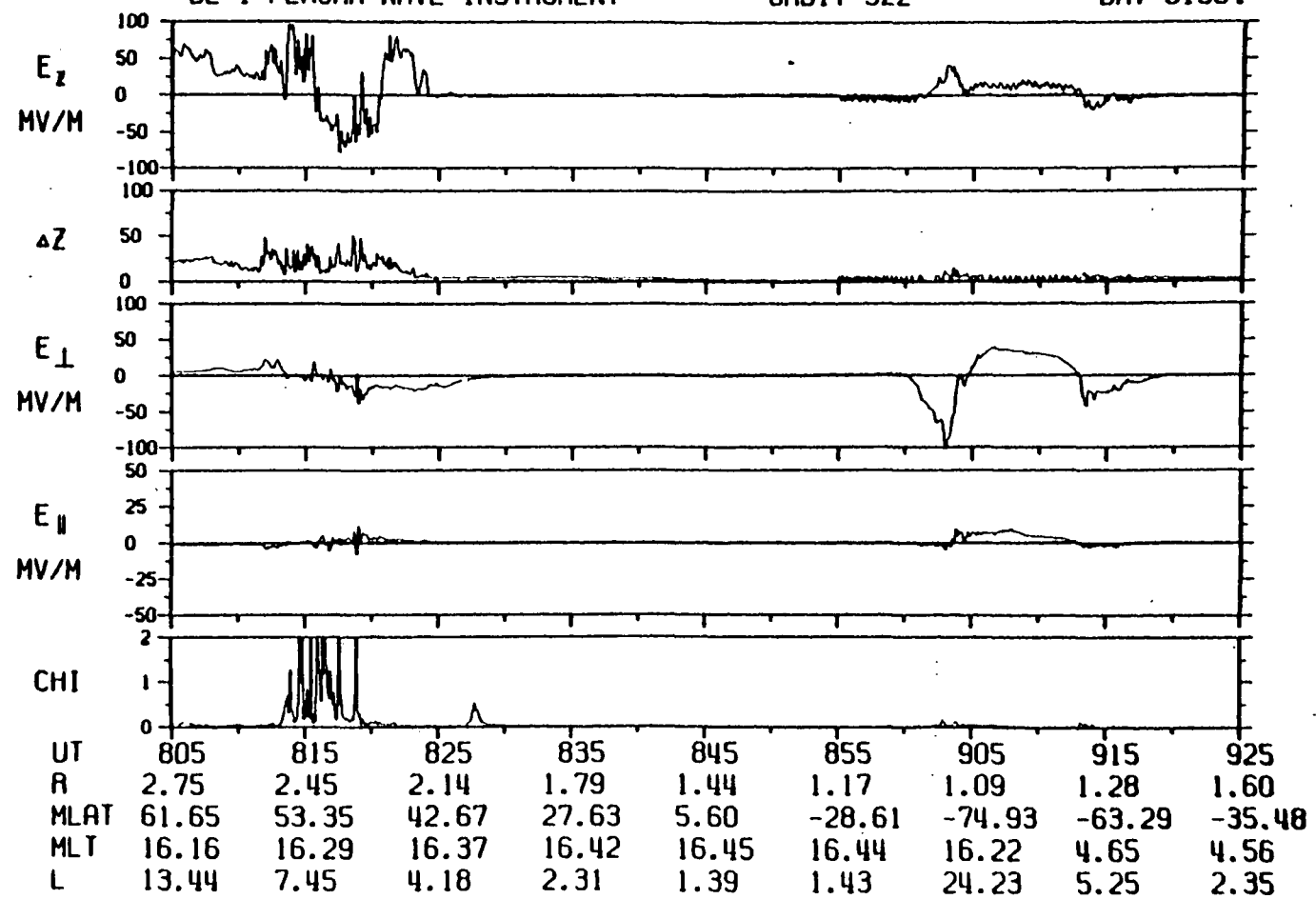


Figure 4

Figure 5

Diagram of the orientation of the  $E_{\perp}$  electric field at different positions of the DE-1 spacecraft in its orbit. The calculation of  $E_{\perp}$  is carried out in a spacecraft coordinate system, with axes  $\hat{X}$ ,  $\hat{Y}$ , and  $\hat{Z}$  pointing in the direction shown. The  $\hat{Y}$  axis is defined to point toward the center of the earth. Since  $B$  changes direction as the spacecraft orbits, the orientation of a positive  $E_{\perp}$  also changes. In the northern hemisphere, a positive  $E_{\perp}$  is in the direction of spacecraft motion, but is oppositely directed in the southern hemisphere. This diagram is highly simplified; the real orbit of DE-1 is elliptical.

A-G83-247

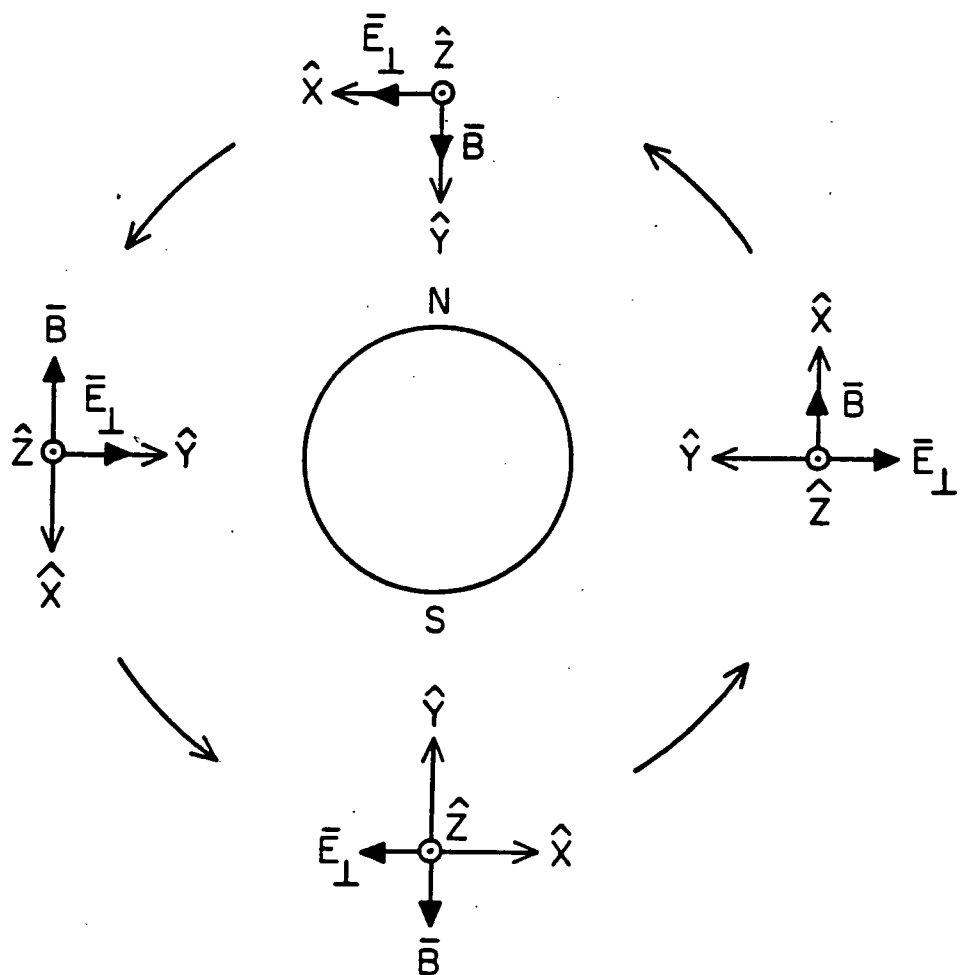


Figure 5

**Figure 6**

Illustration of a case when the magnetic field is not entirely in the spin plane. An electric field vector perpendicular to the magnetic field has a component in the spin plane labeled E<sub>sp</sub>. This vector may have a component parallel to the projection of the magnetic field into the spin release. If B lies completely in the spin plane, this situation cannot occur.

A-G83-173

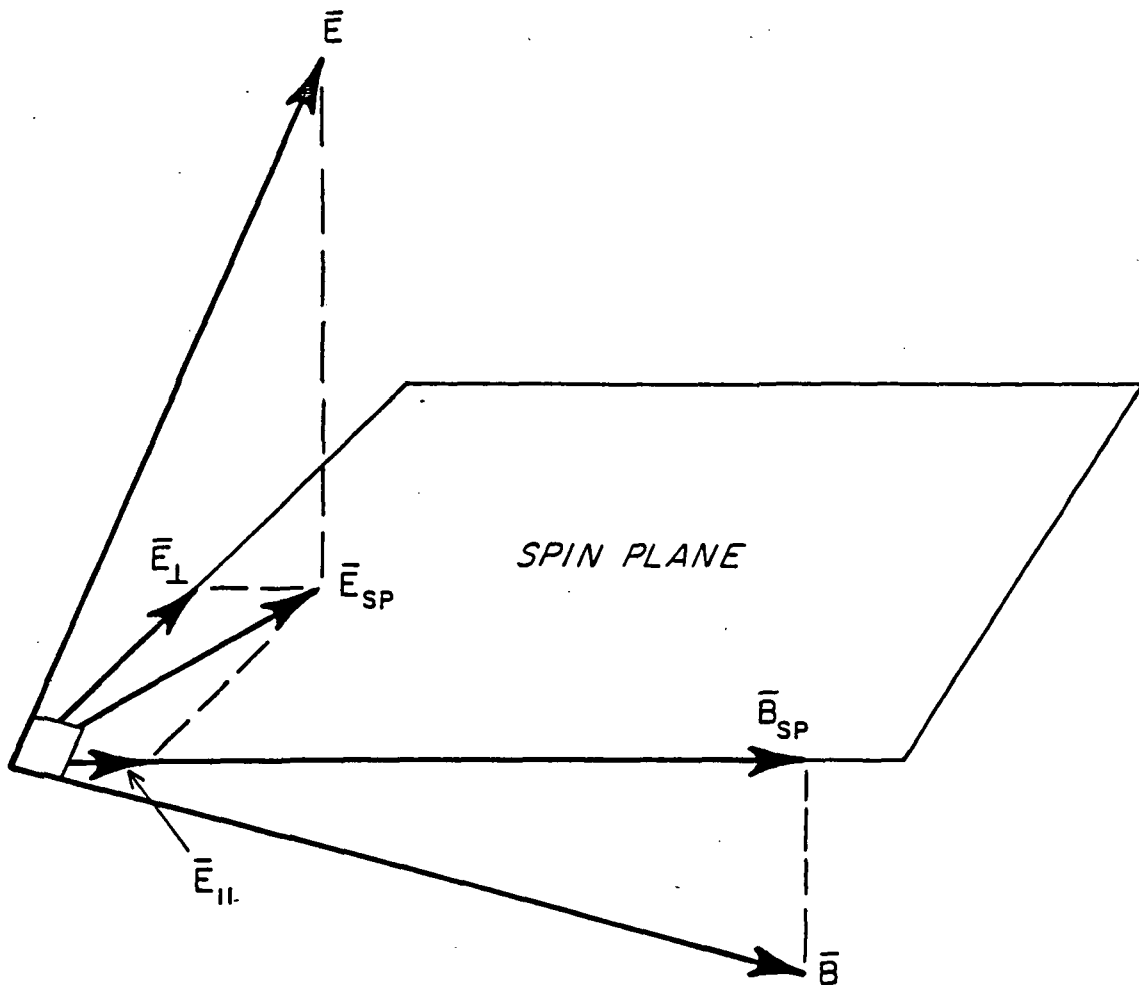


Figure 6

**Figure 7**

Peak electric field summary plot. This graph shows the peak electric fields, both positive and negative, measured on the z-axis and x-axis in each 6 second period. The plot also contains the calculated  $\underline{V} \times \underline{B}$  electric field for both axes. The time period for this graph is the same as the graph in Figure 4. This type of graph is very useful for spotting large peaks in the electric field which get filtered out by the analysis program. The spike near 8:19 UT is one such case. The change in the digital resolution for the low-gain amplifier is evident at 9:02 UT.

A-683-295

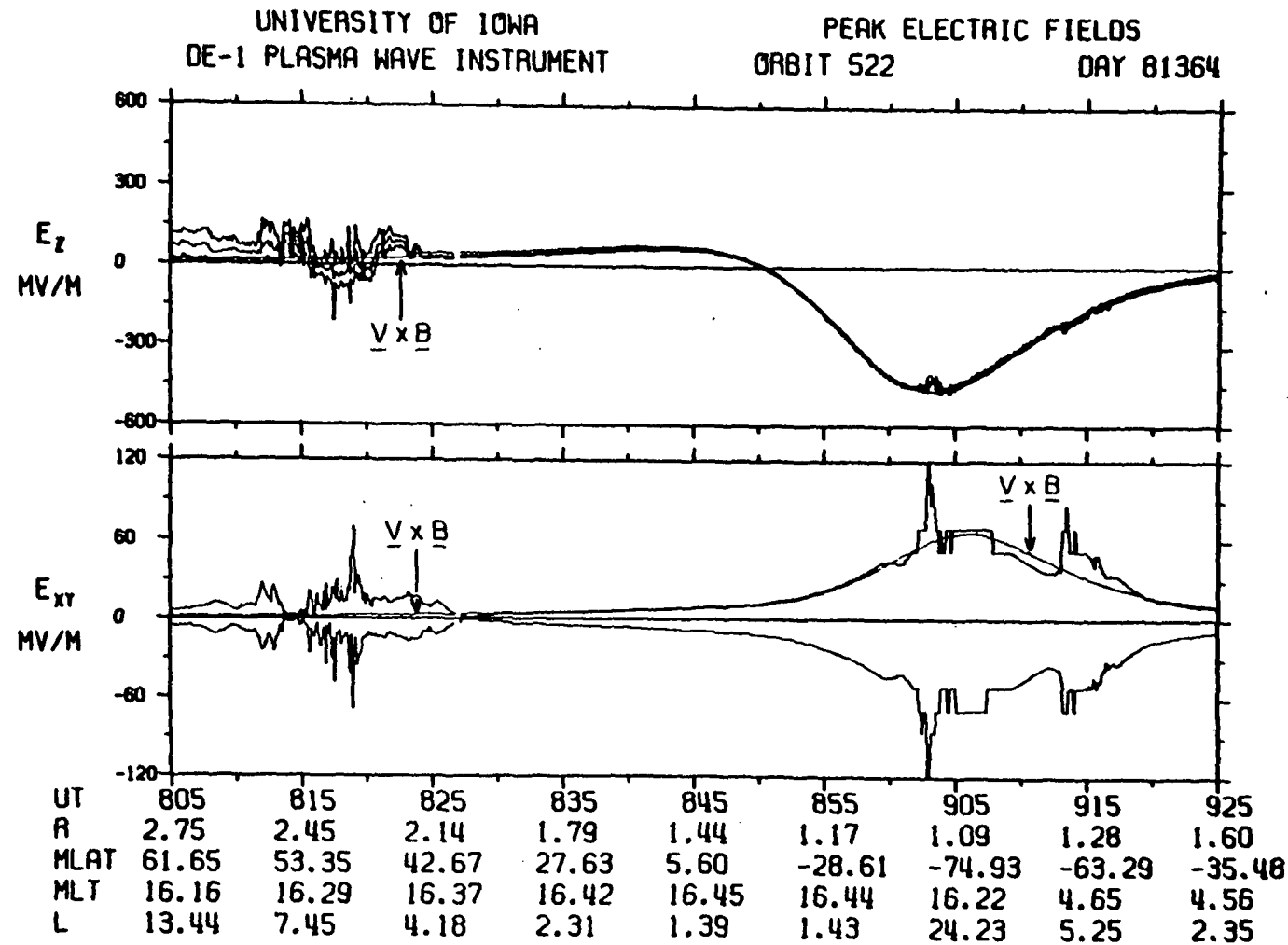


Figure 7

Figure 8      Southern hemisphere plasma convection measured from  
6:15 UT to 6:39 UT on day 81343 (December 9, 1981).

UNIVERSITY OF IOWA  
DE-1 PLASMA WAVE INSTRUMENT

SOUTHERN HEMISPHERE

ALTITUDE:  
780 - 2883 KM

RADIUS:  
1.122 - 1.453 RE

DAY 81343  
ORBIT 448  
615 - 639 UT

CONVECTION VELOCITY  
COMPONENT

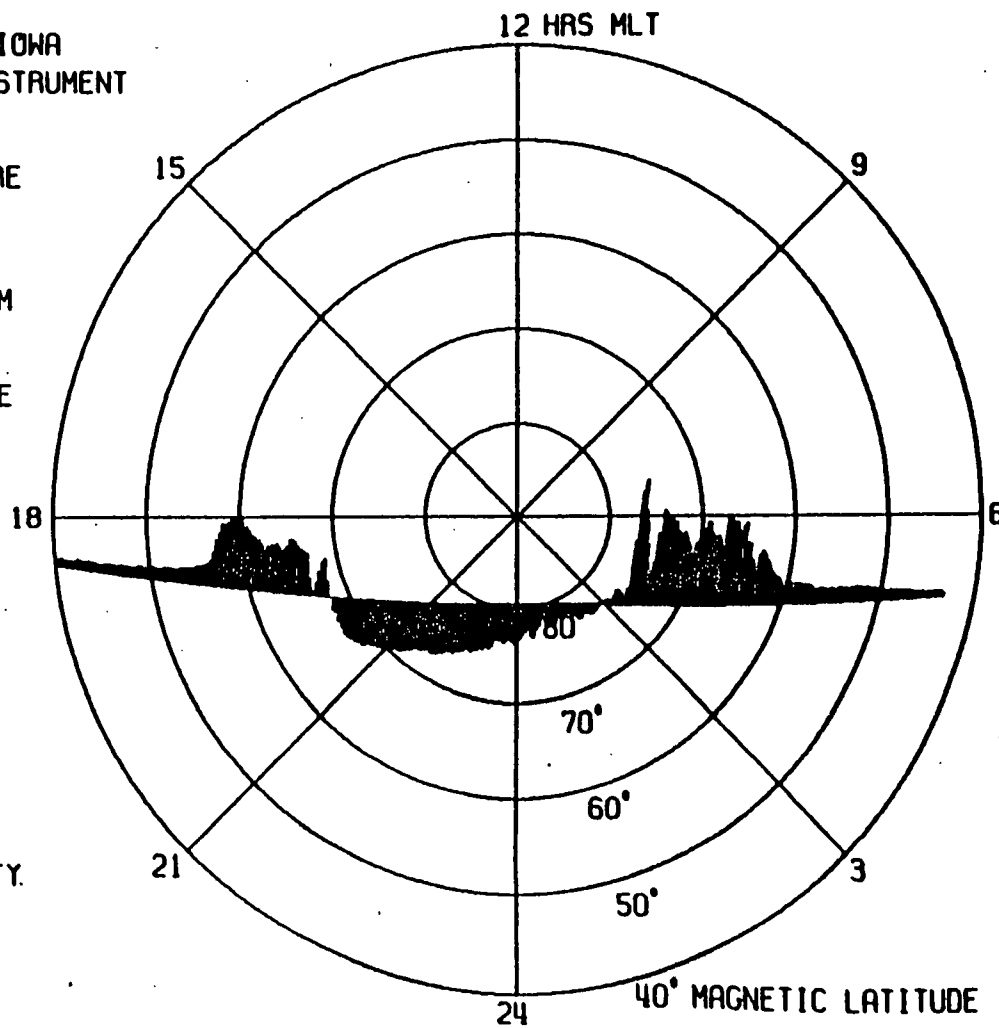
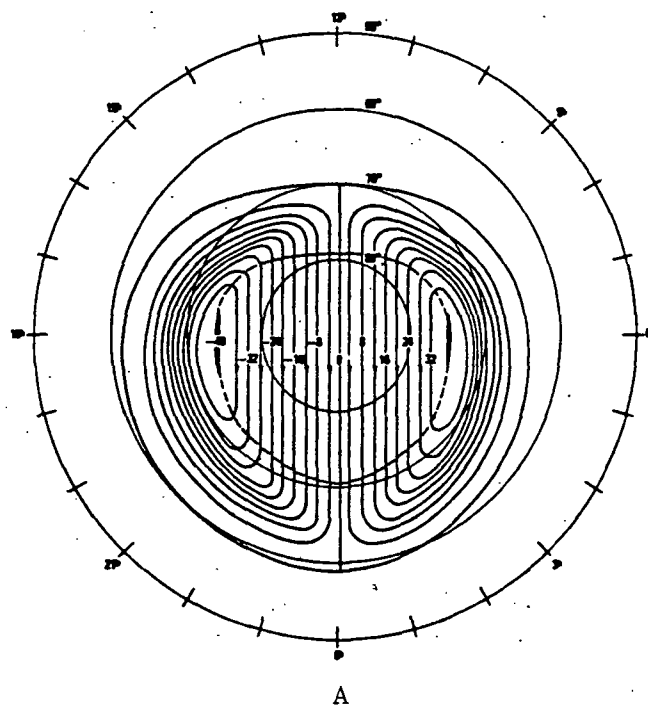


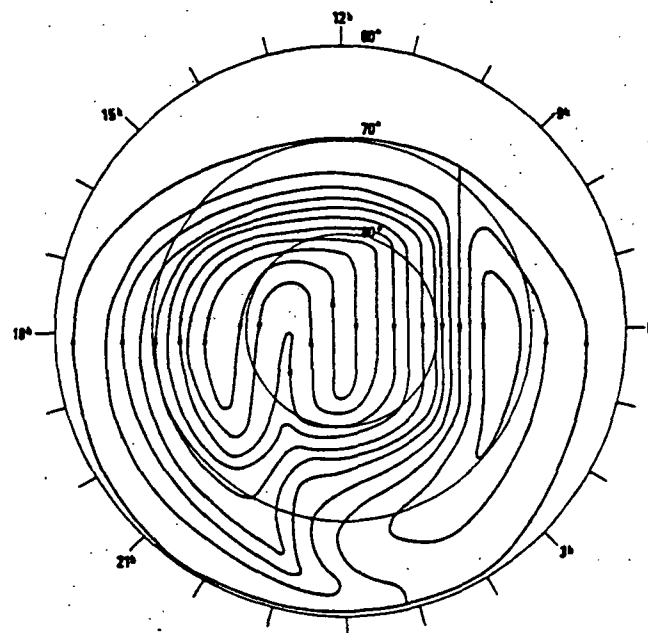
Figure 8

**Figure 9**

Empirical models of polar cap potentials derived by Heppner to match patterns in the OGO-6 data. Model A is a "sun-aligned" representation with 4 kV contour intervals corresponding to the standard two-cell pattern. Model B shows a mode of distorting the two-cell pattern to account for regions of reverse flow in the 18-24 hours local time sector.



A



B

Figure 9

Figure 10

Interplanetary magnetic field data and geomagnetic activity indices for day 81343 (December 9, 1981). The bar after 6 hours marks the period when the data in figure 8 was obtained. Just before this time, the IMF was southward (negative  $B_Z$ ). The IMF data was obtained from the National Space Science Data Center composite omnитape SM-41B. The magnetic activity indices are from Solar Geophysical Data, published by NOAA Environmental Data and Information Service.

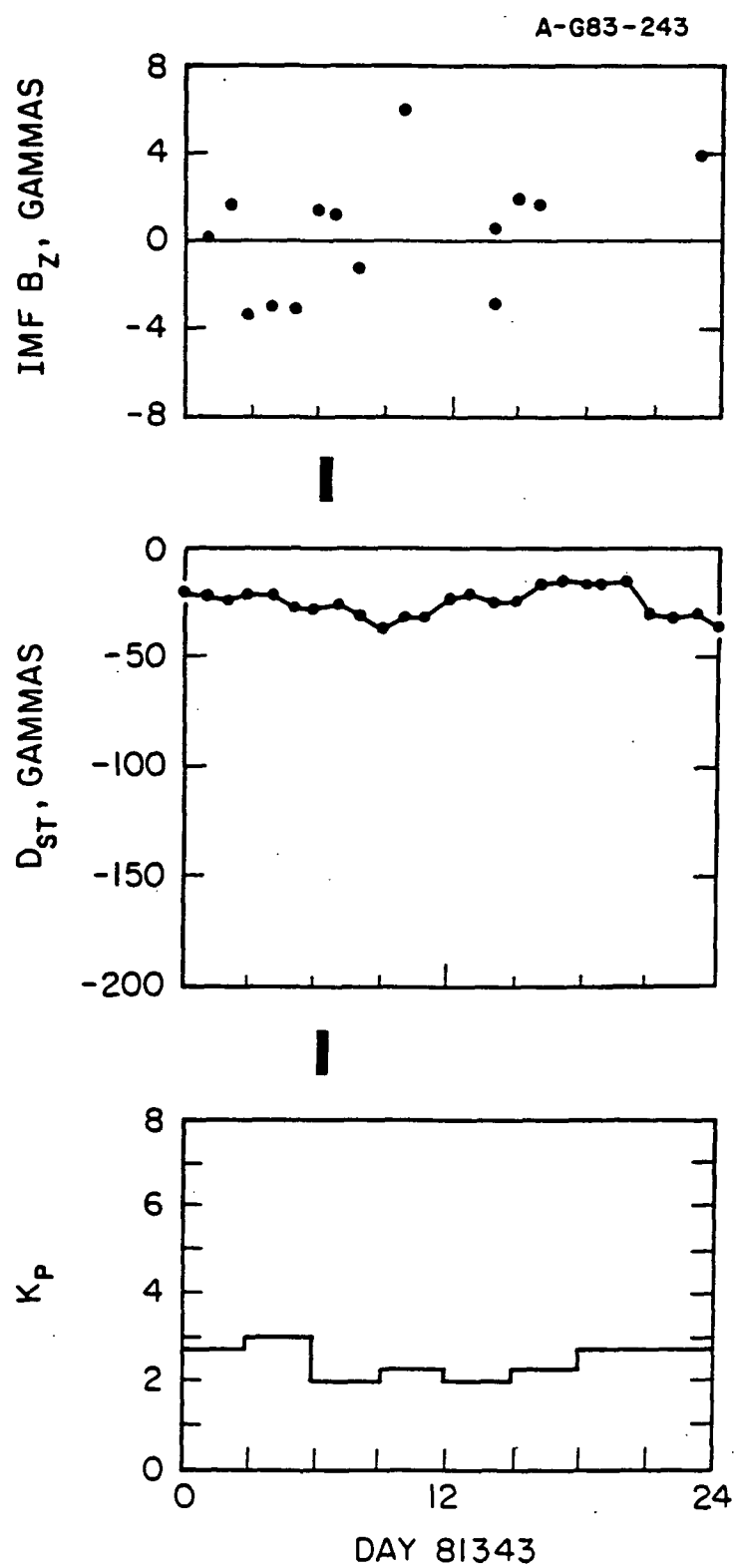


Figure 10

**Figure 11**

Southern hemisphere plasma convection measured from 8:06 UT to 8:29 UT on day 81287 (October 14, 1981). This is the first of three graphs illustrating the variability from one orbit to the next. During this time DE-1 was reaching perigee altitude of 675 km over the south pole. The altitudes in the figure refer to the start and end points on the plot.

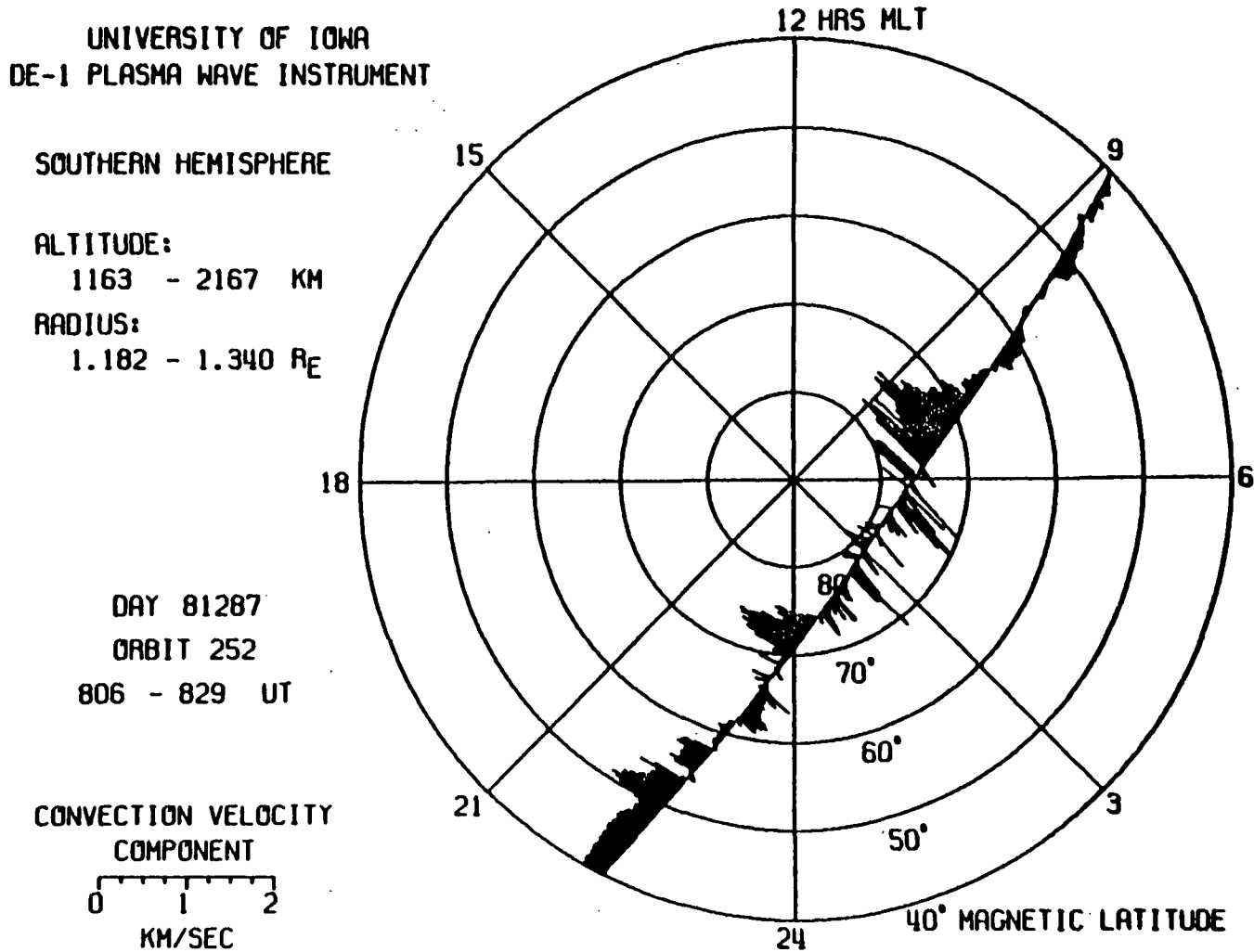


Figure 11

**Figure 12**      Southern hemisphere plasma convection measured from  
14:54 UT to 15:17 UT on day 81287 (October 14, 1981).

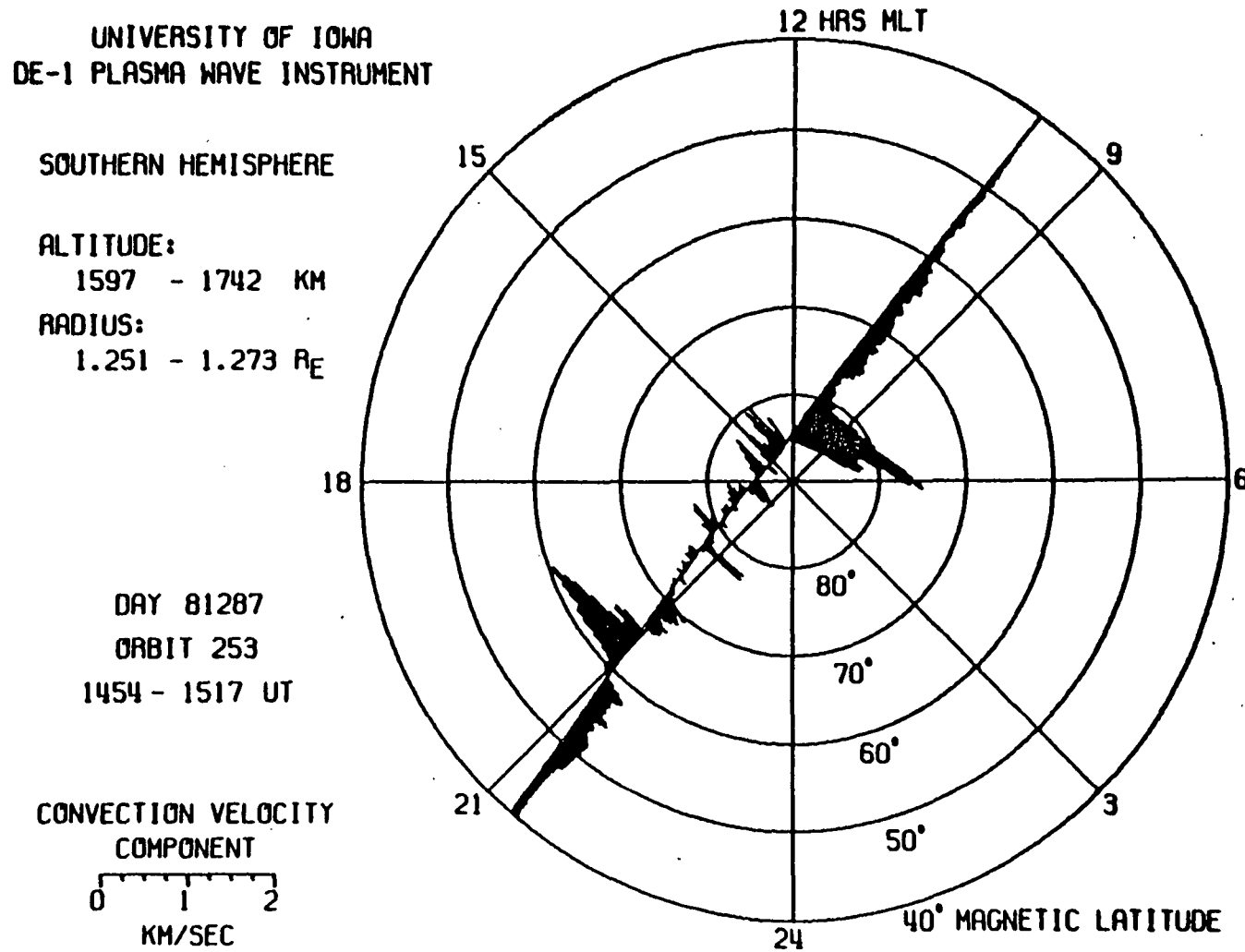


Figure 12

Figure 13      Southern hemisphere plasma convection measured from  
21:49 UT to 22:14 UT on day 81287 (October 14,  
1981). There is a gap in the data from 60° to 65°  
MLAT in the morning sector.

UNIVERSITY OF IOWA  
DE-1 PLASMA WAVE INSTRUMENT

SOUTHERN HEMISPHERE

ALTITUDE:

975 - 2755 KM

RADIUS:

1.153 - 1.432 RE

DAY 81287

ORBIT 254

2149 - 2214 UT

CONVECTION VELOCITY  
COMPONENT

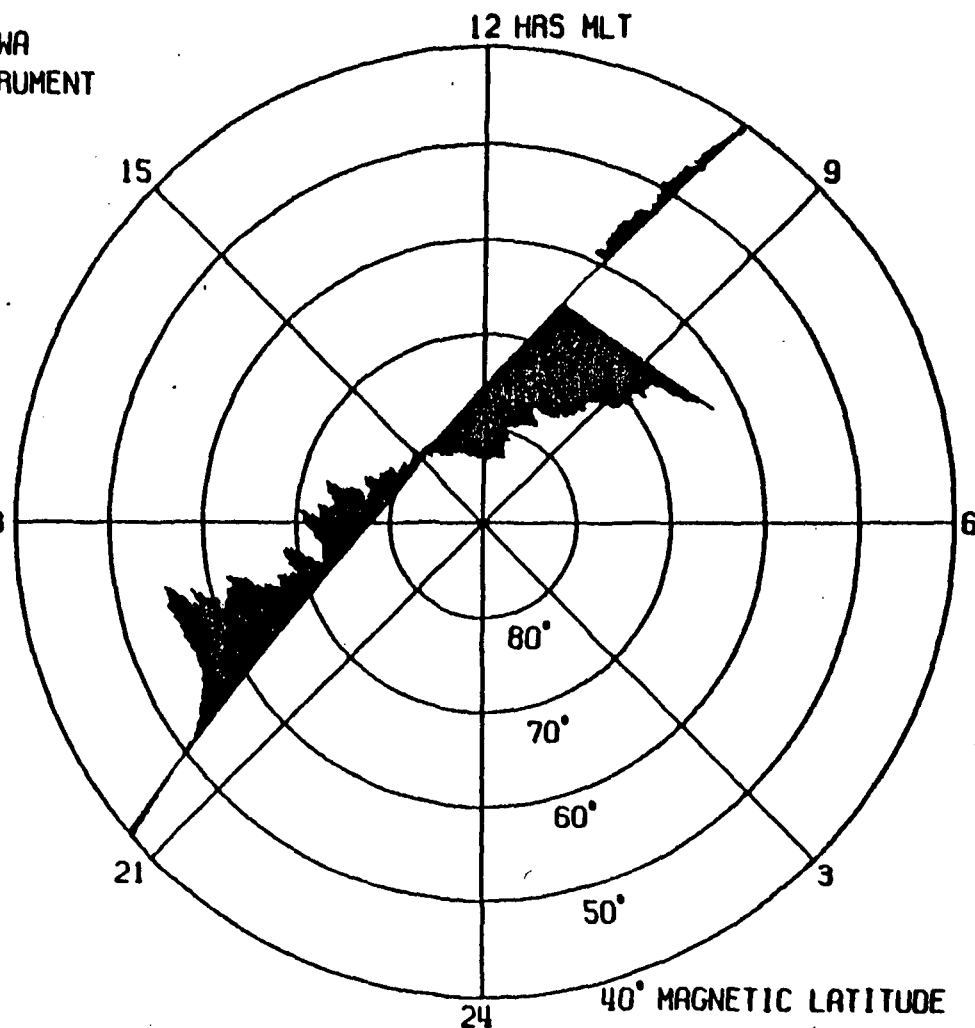


Figure 13

Figure 14      Interplanetary magnetic field and geomagnetic activity indices for day 81287 (October 14, 1981).  
The three dark bars mark the periods when the data in figures 11, 12, and 13 were obtained.

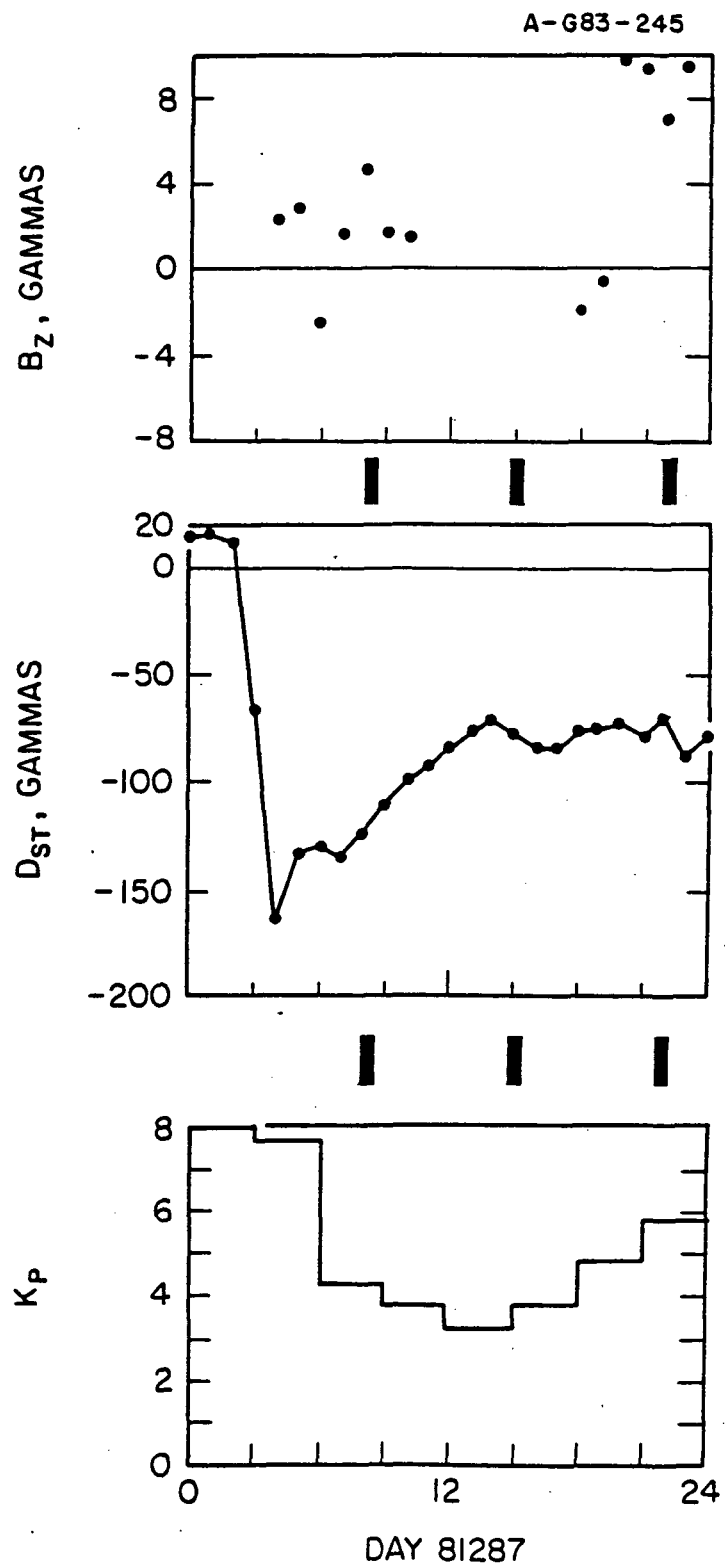


Figure 14

**Figure 15      Southern hemisphere plasma convection measured from  
4:29 UT to 4:53 UT on day 81294 (October 21, 1981).**

UNIVERSITY OF IOWA  
DE-1 PLASMA WAVE INSTRUMENT

SOUTHERN HEMISPHERE

ALTITUDE:  
876 - 2941 KM

RADIUS:  
1.137 - 1.462  $R_E$

DAY 81294  
ORBIT 276  
429 - 453 UT

CONVECTION VELOCITY  
COMPONENT

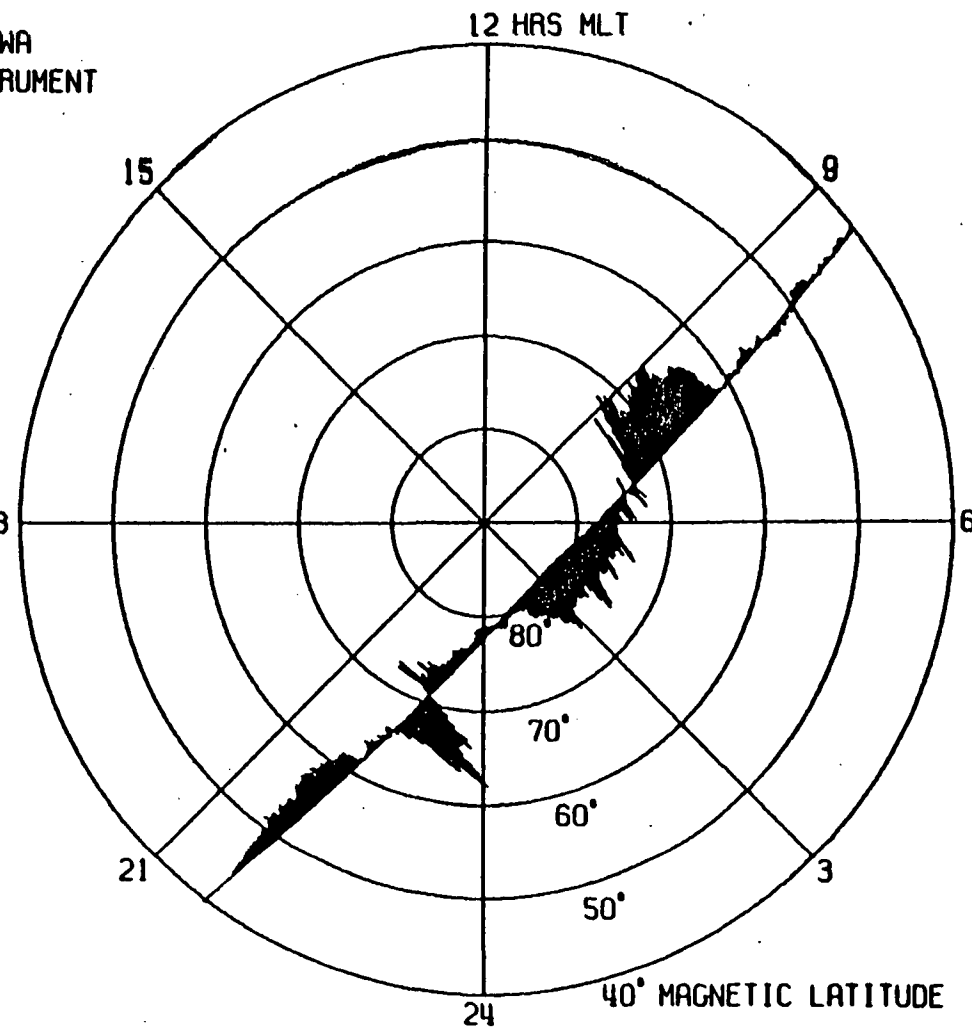


Figure 15

Figure 16      Southern hemisphere plasma convection measured from  
11:16 UT to 11:39 UT day 81294 (October 21, 1981).

UNIVERSITY OF IOWA  
DE-1 PLASMA WAVE INSTRUMENT

SOUTHERN HEMISPHERE

ALTITUDE:

1426 - 1856 KM

RADIUS:

1.224 - 1.291 RE

DAY 81294

ORBIT 277

1116 - 1139 UT

CONVECTION VELOCITY  
COMPONENT

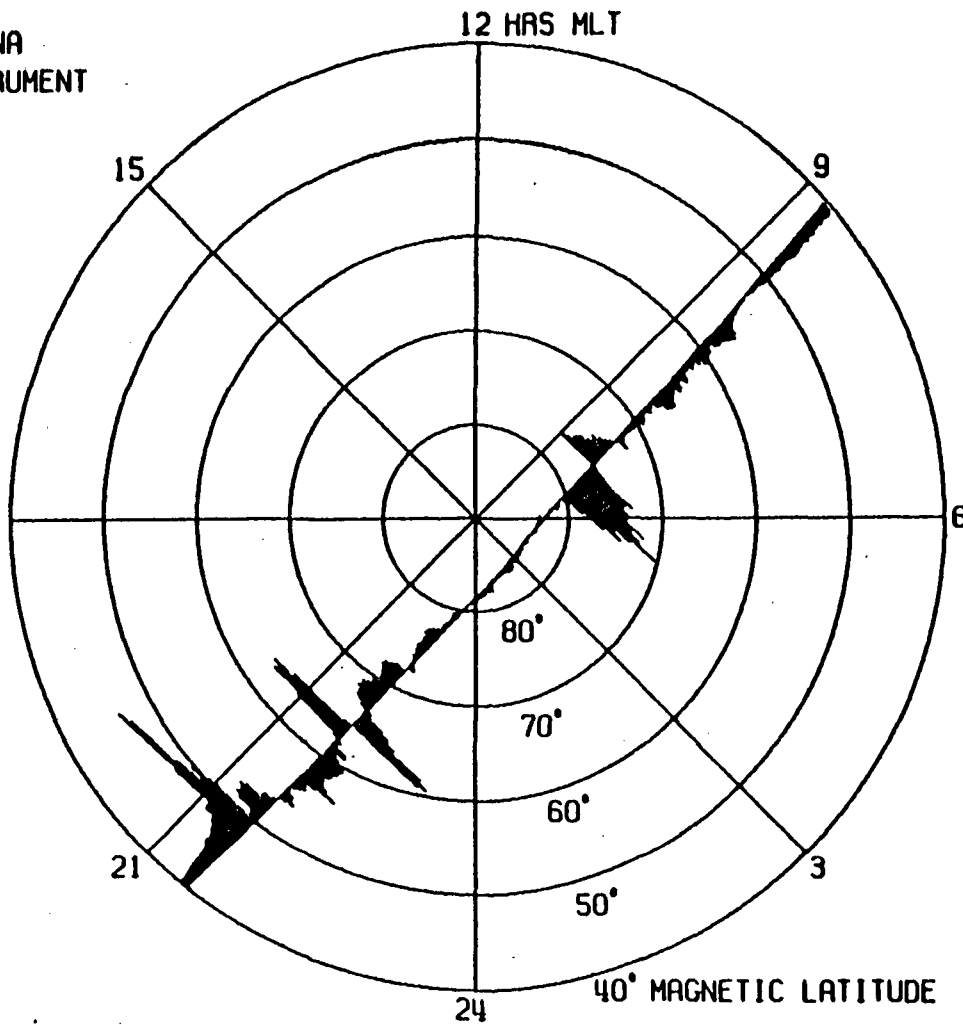


Figure 16

Figure 17      Southern hemisphere plasma convection measured from  
18:08 UT to 18:32 UT day 81294 (October 21, 1981).  
There is a gap in the transmitted data around 15 hrs.  
MLT.

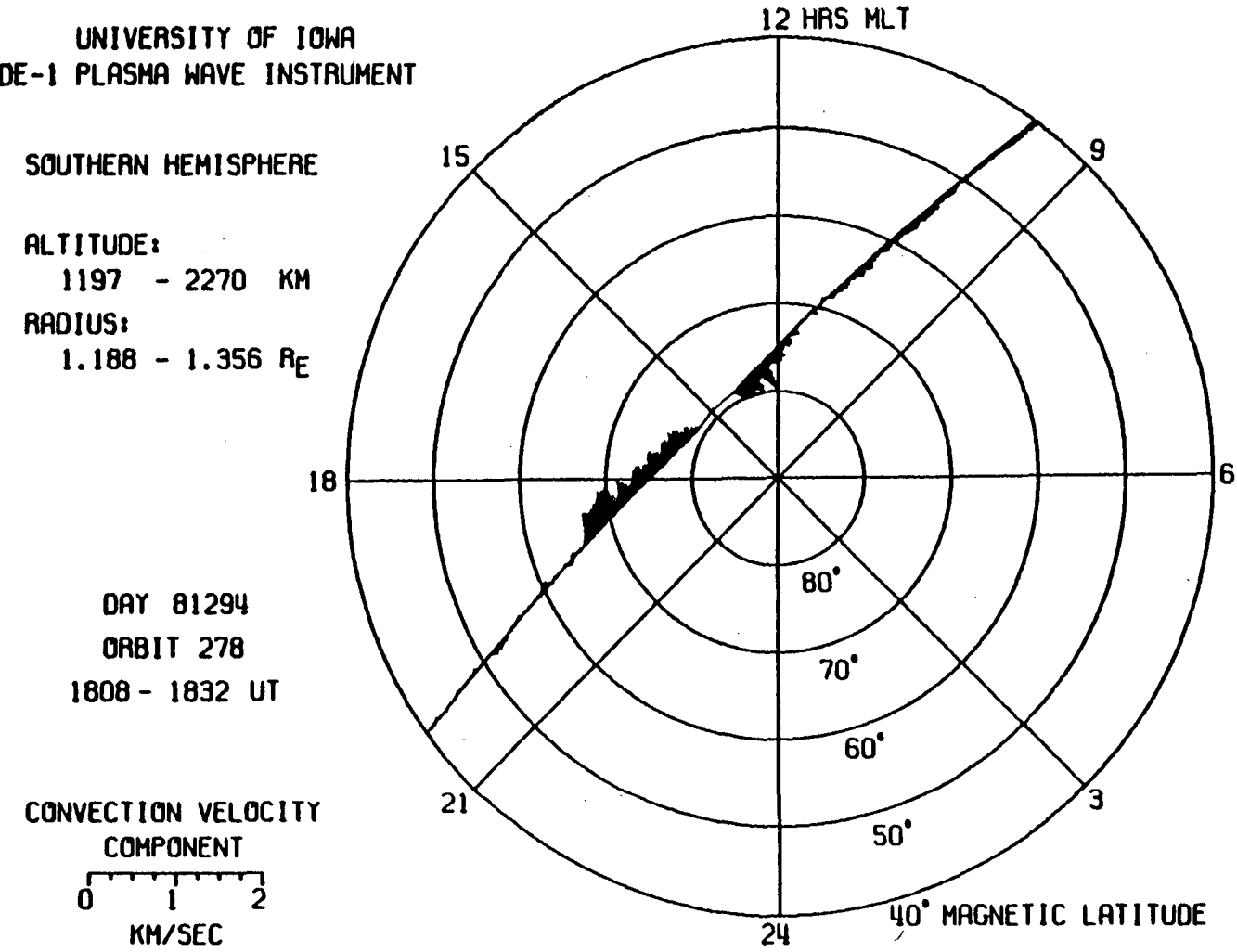


Figure 17

Figure 18      Southern hemisphere plasma convection measured from  
1:03 UT to 1:28 UT day 81295 (October 22, 1981).

UNIVERSITY OF IOWA  
DE-1 PLASMA WAVE INSTRUMENT

SOUTHERN HEMISPHERE

ALTITUDE:

800 - 3359 KM

RADIUS:

1.126 - 1.527  $R_E$

DAY 81295

ORBIT 279

103 - 128 UT

CONVECTION VELOCITY  
COMPONENT

0 1 2  
KM/SEC

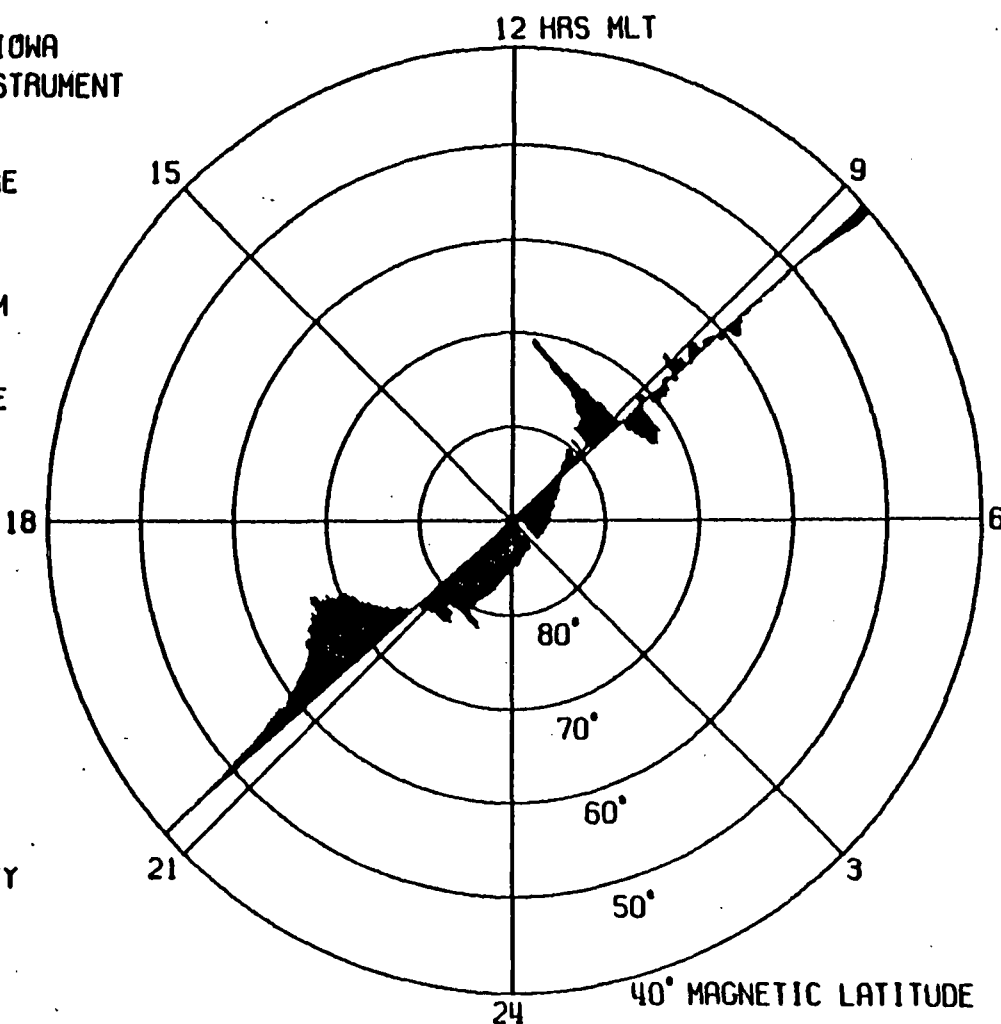


Figure 18

**Figure 19      Southern hemisphere plasma convection measured from  
4:25 UT to 4:50 UT day 81296 (October 23, 1981).**

UNIVERSITY OF IOWA  
DE-1 PLASMA WAVE INSTRUMENT

SOUTHERN HEMISPHERE

ALTITUDE:

859 - 3057 KM

RADIUS:

1.135 - 1.480  $R_E$

DAY 81296

ORBIT 283

425 - 450 UT

CONVECTION VELOCITY  
COMPONENT

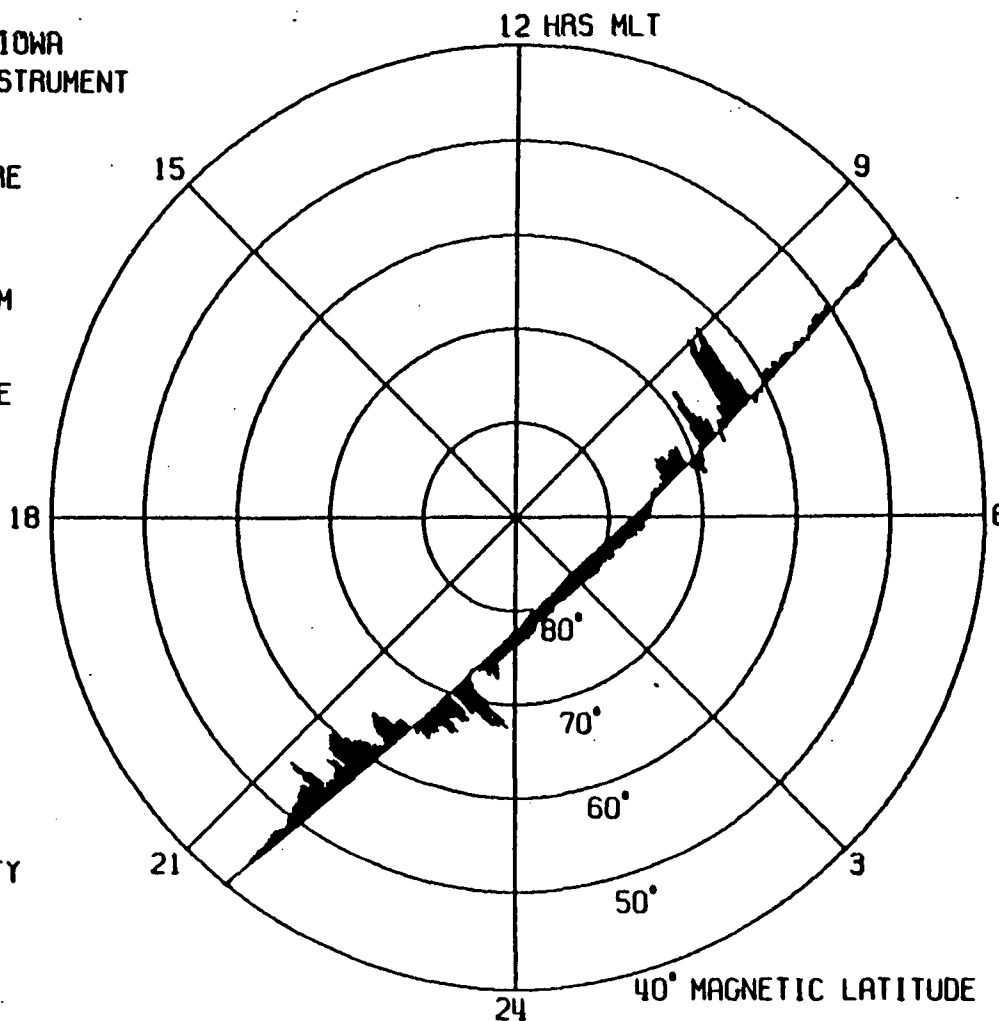


Figure 19

**Figure 20**      Southern hemisphere plasma convection measured from  
11:12 UT to 11:35 UT day 18296 (October 23, 1981).

UNIVERSITY OF IOWA  
DE-1 PLASMA WAVE INSTRUMENT

SOUTHERN HEMISPHERE

ALTITUDE:  
1400 - 1907 KM

RADIUS:  
1.220 - 1.299  $R_E$

DAY 81296  
ORBIT 284  
1112 - 1135 UT

CONVECTION VELOCITY  
COMPONENT  
0 1 2  
KM/SEC

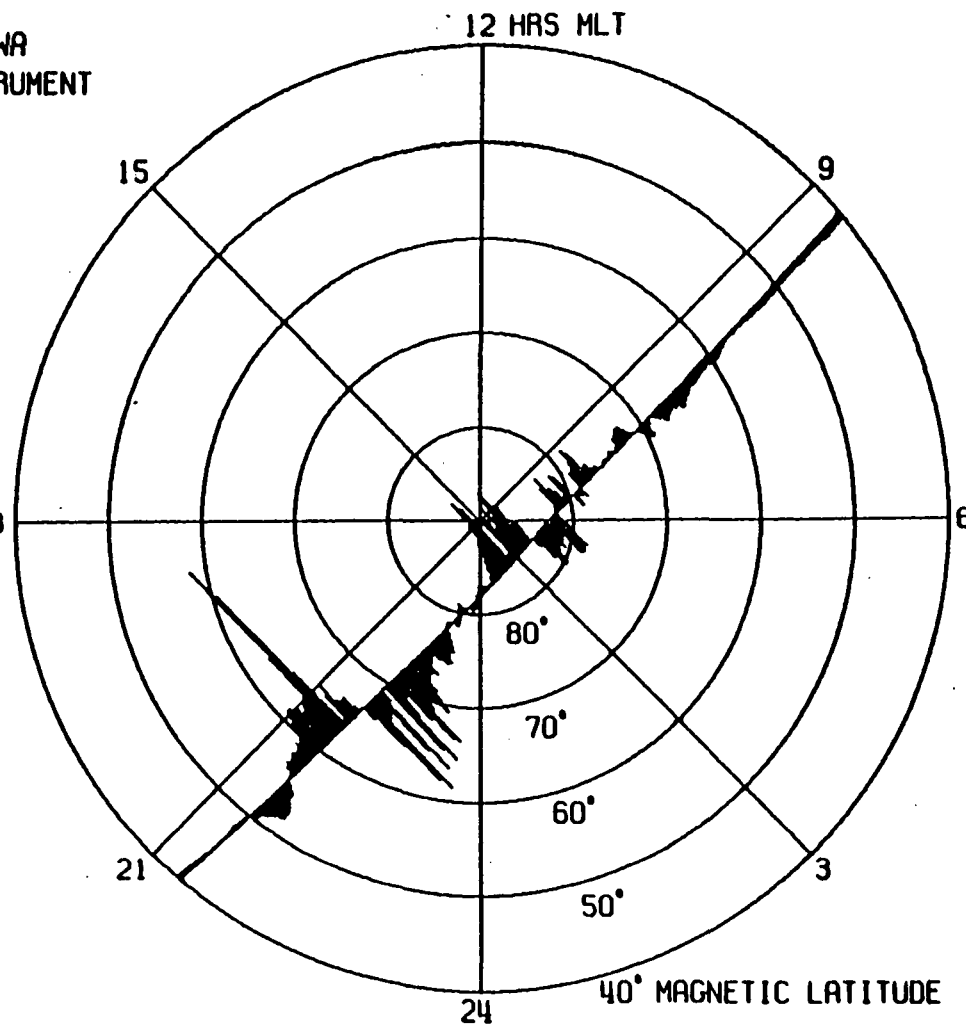


Figure 20

Figure 21      Southern hemisphere plasma convection measured from  
4:22 UT to 4:46 UT day 81298 (October 25, 1981).

UNIVERSITY OF IOWA  
DE-1 PLASMA WAVE INSTRUMENT

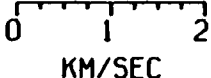
SOUTHERN HEMISPHERE

ALTITUDE:  
841 - 3092 KM

RADIUS:  
1.132 - 1.485  $R_E$

DAY 81298  
ORBIT 290  
422 - 446 UT

CONVECTION VELOCITY  
COMPONENT



0 1 2  
KM/SEC

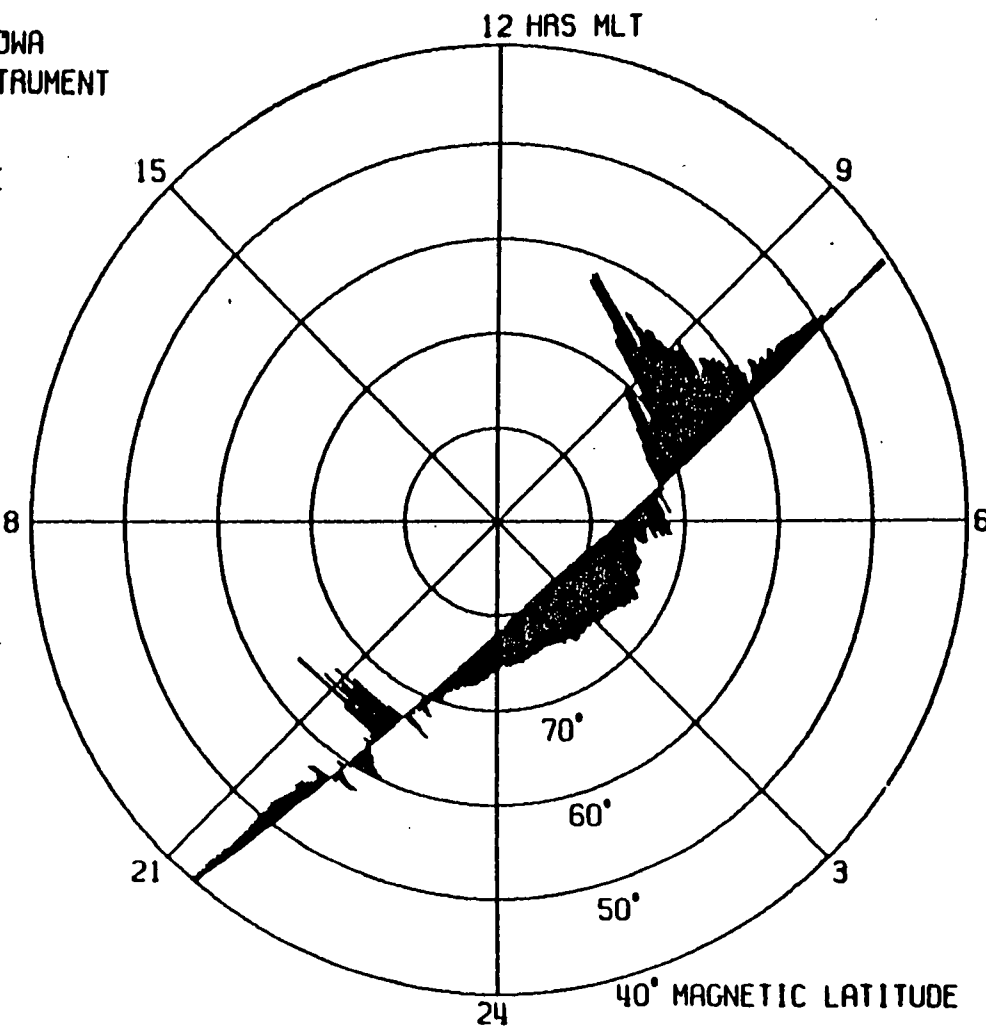


Figure 21

Figure 22

Geomagnetic activity indices for the period from day 81294 (October 21, 1981) to day 81298 (October 25, 1981). The seven bars positioned along the time scale mark the periods when the data on figures 15 through 21 were obtained.

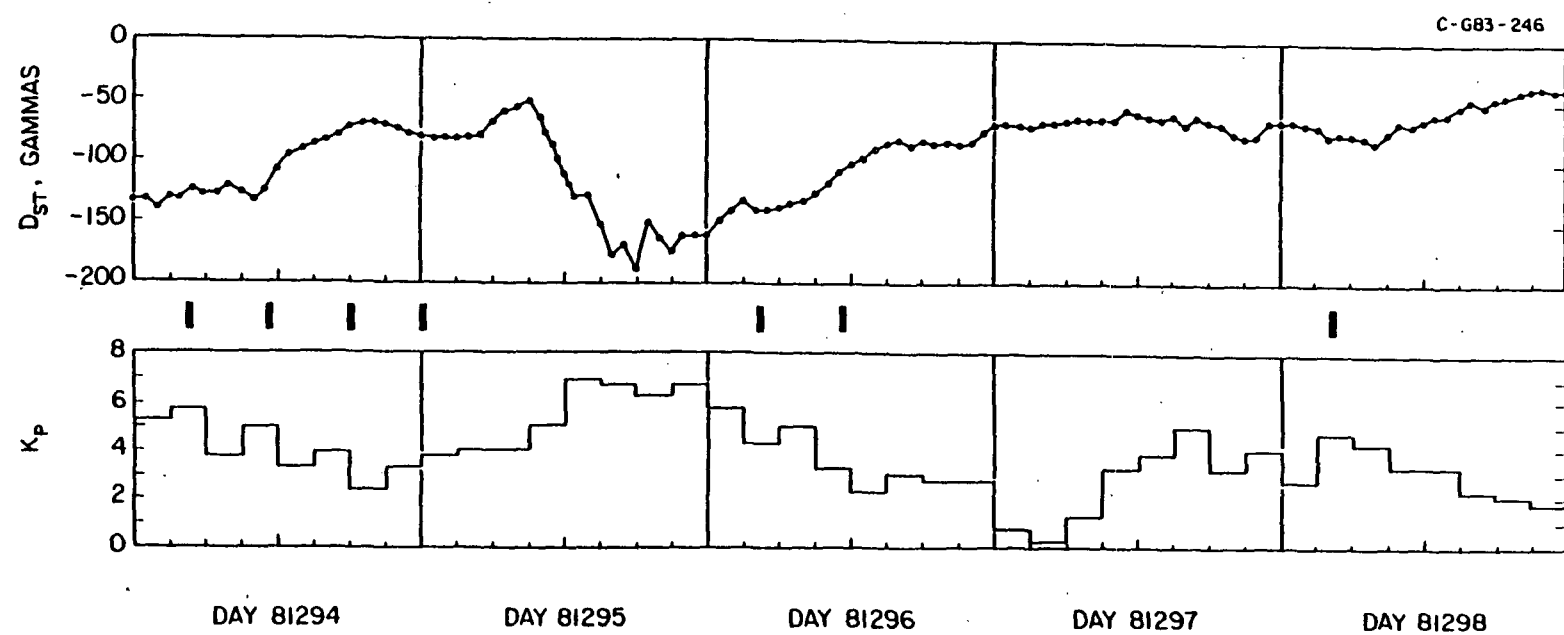


Figure 22

Figure 23

Southern hemisphere plasma convection measured from 8:57 UT to 9:23 UT on day 81364 (December 30, 1981). This graph has the best plasma flow pattern corresponding to a two-cell circulation seen in the data processed to date. The electric field graphs for this time period are in Figures 4 and 7.

UNIVERSITY OF IOWA  
DE-1 PLASMA WAVE INSTRUMENT

SOUTHERN HEMISPHERE

ALTITUDE:  
763 - 3414 KM

RADIUS:  
1.120 - 1.536  $R_E$

DAY 81364  
ORBIT 522  
857 - 923 UT

CONVECTION VELOCITY  
COMPONENT

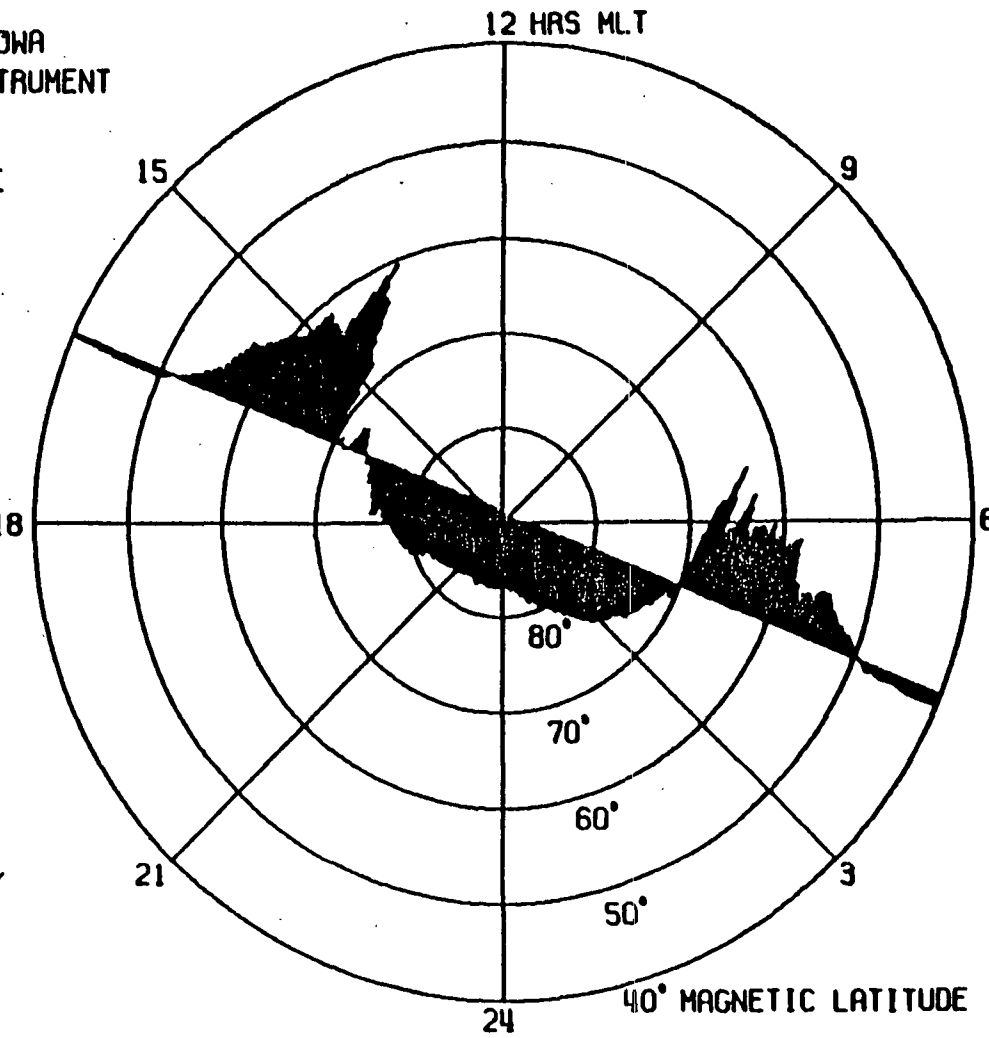


Figure 23

Figure 24      Interplanetary magnetic field data and geomagnetic activity indices for day 81364 (December 30, 1981).  
The bar on the time scale marks the time when the data in figure 23 were obtained.

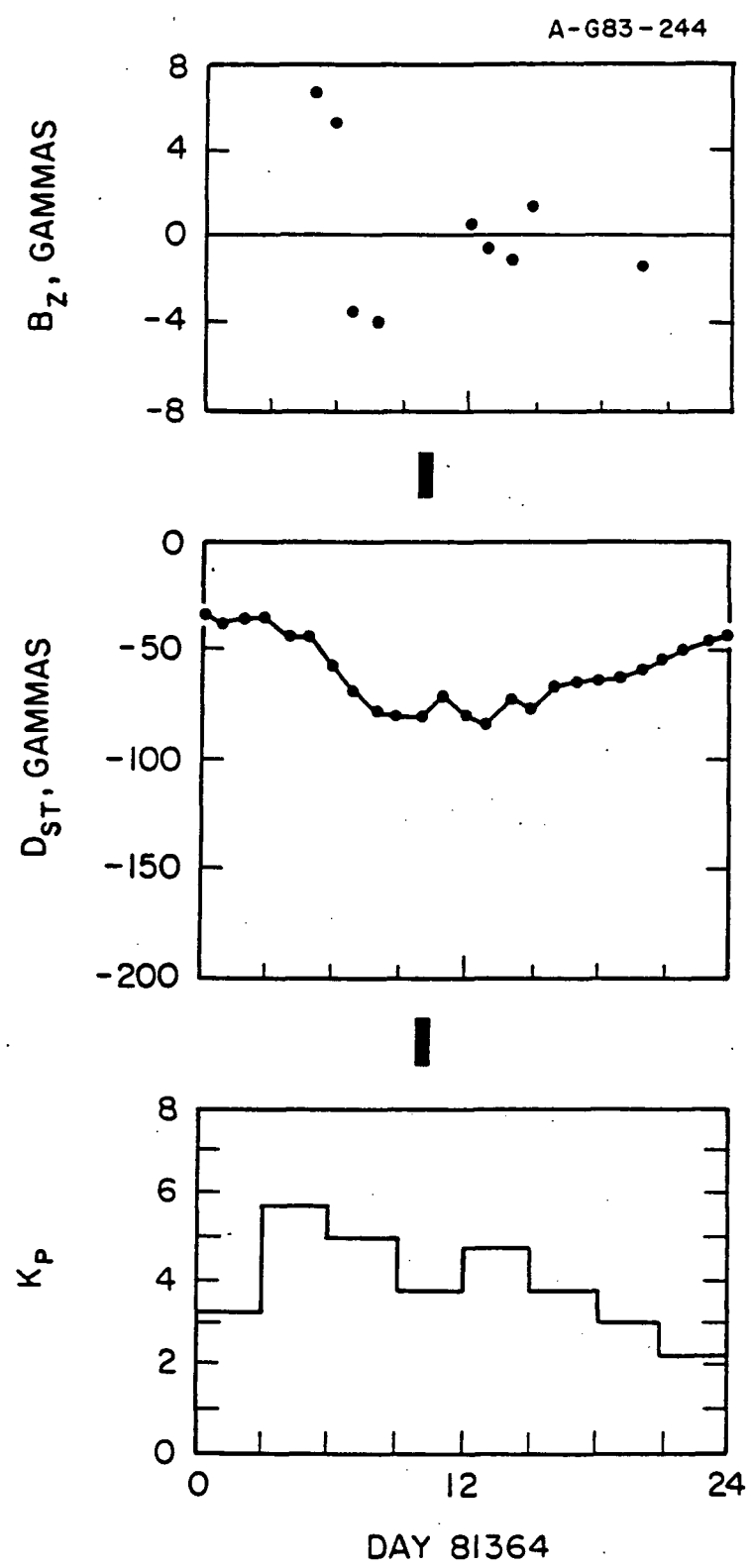


Figure 24

**Figure 25**

Example of oppositely directed electric fields detected on auroral field lines. The DE-1 spacecraft was at an invariant latitude of  $65.3^\circ$  and altitude of 9,000 km, moving 5.46 km/s. At 28 seconds from the start of the plot, a field with a magnitude of 90 mV/m was detected. In the next spin period a larger field was detected, but with a  $180^\circ$  phase reversal.

A-683-293

UNIVERSITY OF IOWA  
DE-1 PLASMA WAVE INSTRUMENT      DC ELECTRIC FIELD  
ORBIT 283      DAY 81296      UT 3:44:44 - 3:45:56

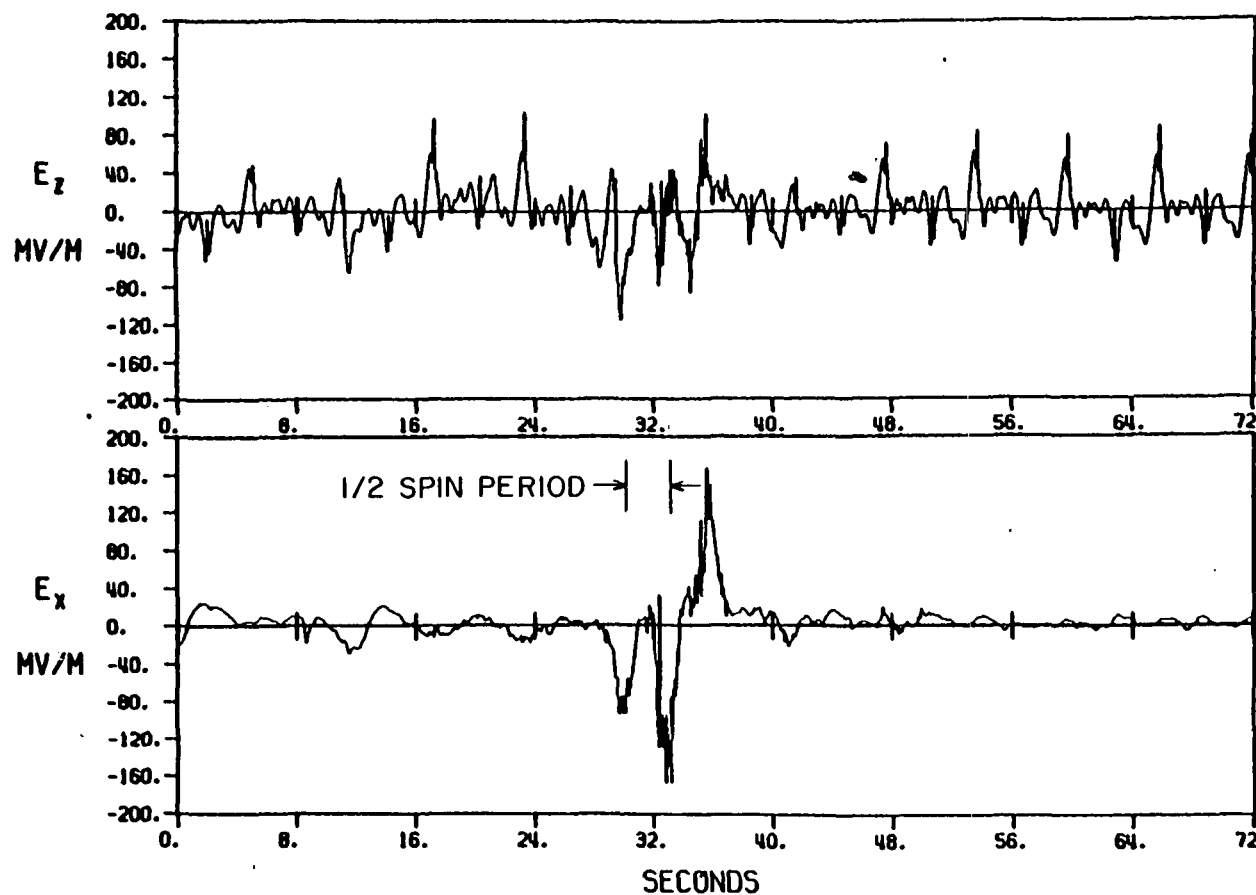


Figure 25

**Figure 26**      Northern hemisphere plasma convection measured from  
14:35 UT to 15:35 UT on day 82092 (April 2, 1982).  
At 15:27 UT an "auroral vortex" was encountered.

A-G83-296

UNIVERSITY OF IOWA  
DE-1 PLASMA WAVE INSTRUMENT

NORTHERN HEMISPHERE

ALTITUDE:  
13625 - 1596 KM

RADIUS:  
3.139 - 1.250 RE

DAY 82092

ORBIT 849

1435 - 1535 UT

CONVECTION VELOCITY  
COMPONENT

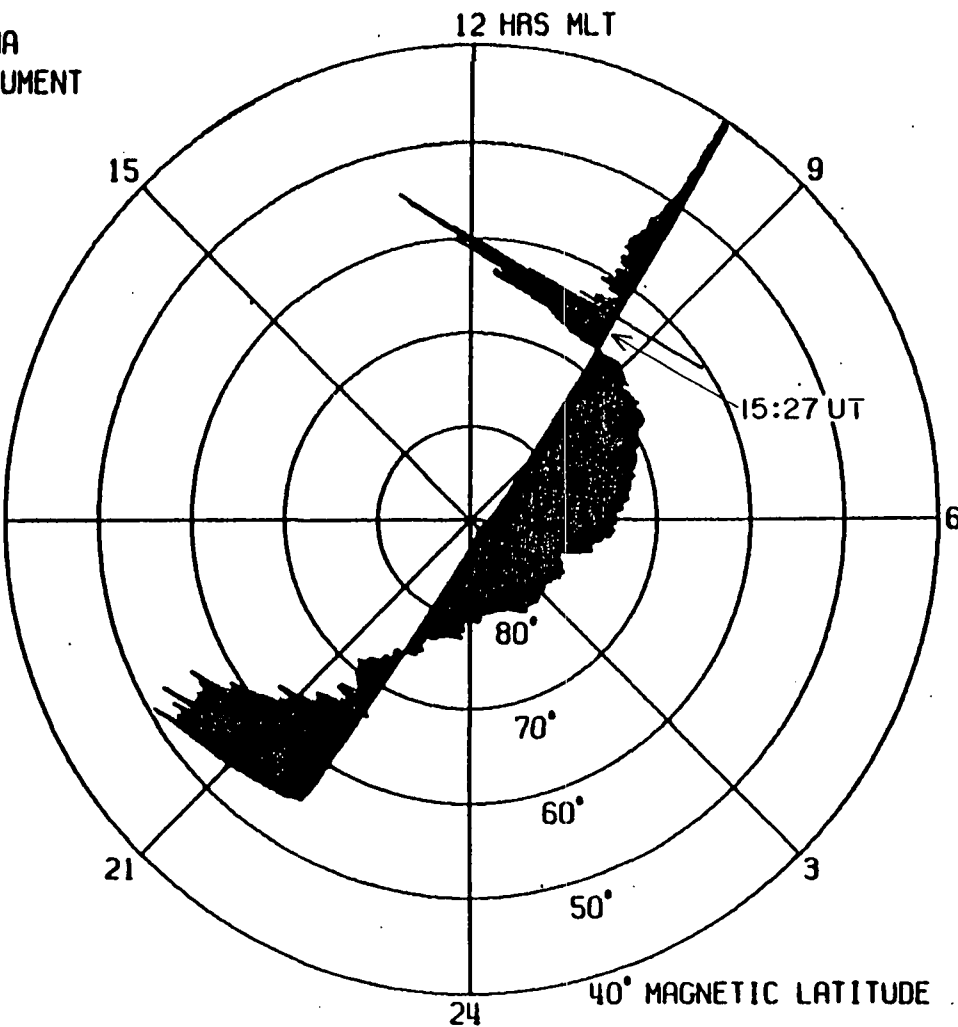


Figure 26

**Figure 27**

High-resolution electric field data for the auroral vortex event at 15:27 UT on day 82092. Up to the time 32 seconds from the start of the plot the field in the spin plane ( $E_x$ ) is increasing, then there is a sudden reversal. The field at 35 seconds is  $180^\circ$  out of phase. After 44 seconds the phase of the sine wave is the same as at the start. A very large change is seen on the Z axis at the same point where the field in the spin plane reverses.

UNIVERSITY OF IOWA  
DE-1 PLASMA WAVE INSTRUMENT      DC ELECTRIC FIELD  
ORBIT 849      DAY 82092      UT 15:27:16 - 15:28:28

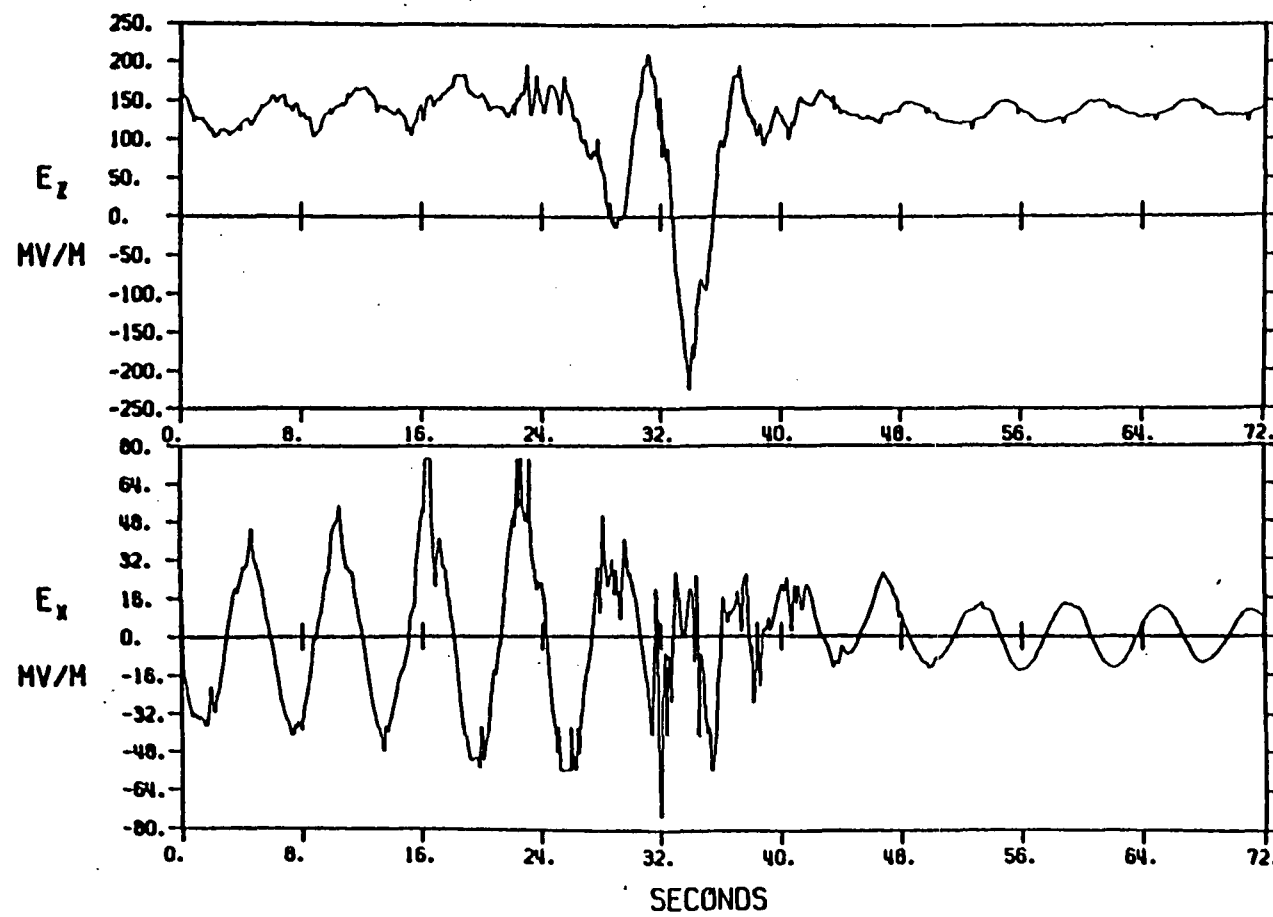


Figure 27

Figure 28      Plasma Wave Instrument spectrogram for 14:30 UT to  
18:30 UT on day 82092 (April 2, 1982). A broadband  
noise burst was detected at 15:27 UT, coincident with  
the auroral vortex seen in the electric field data.

**"Page missing from available version"**

Figure 29

Southern hemisphere plasma convection measured from  
22:02 UT to 22:43 UT on day 82108 (April 18, 1982).  
The events of interest are the peak at 22:09 UT and  
the sudden reversal at 22:24 UT.

A-683-297

UNIVERSITY OF IOWA  
DE-1 PLASMA WAVE INSTRUMENT

SOUTHERN HEMISPHERE

ALTITUDE:

601 - 8829 KM

RADIUS:

1.094 - 2.386  $R_E$

DAY 82108

ORBIT 906

2202 - 2243 UT

CONVECTION VELOCITY  
COMPONENT

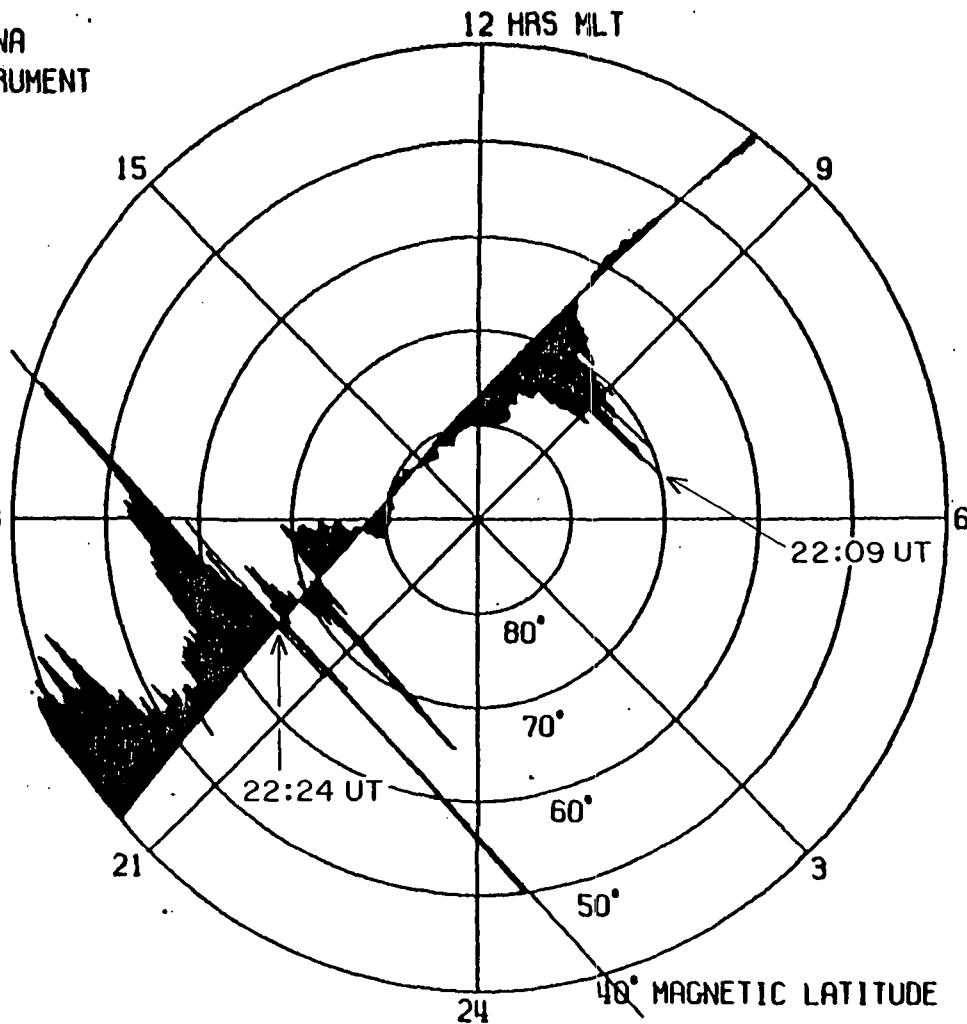


Figure 29

Figure 30      Plasma Wave Instrument spectrogram for 21:30 UT to  
                  23:30 UT on day 82108 (April 18, 1982). Broadband  
                  noise bursts occur at 22:09 UT and 22:24 UT.

**"Page missing from available version"**

**Figure 31**

Example of an unusual, low latitude electric field found on a magnetic field line coincident with an SAR arc. This data is from day 81293 (October 20, 1981). The graph spans only 16 minutes of time. The peak in the  $E_1$  plot occurs at 14:11 UT, when DE-1 was on an L shell of 2.82, which translates to an invariant latitude of  $53^\circ$ . At the same time, an SAR arc was detected with ground-based photometers. The location of the arc was  $53^\circ$  INVLAT.

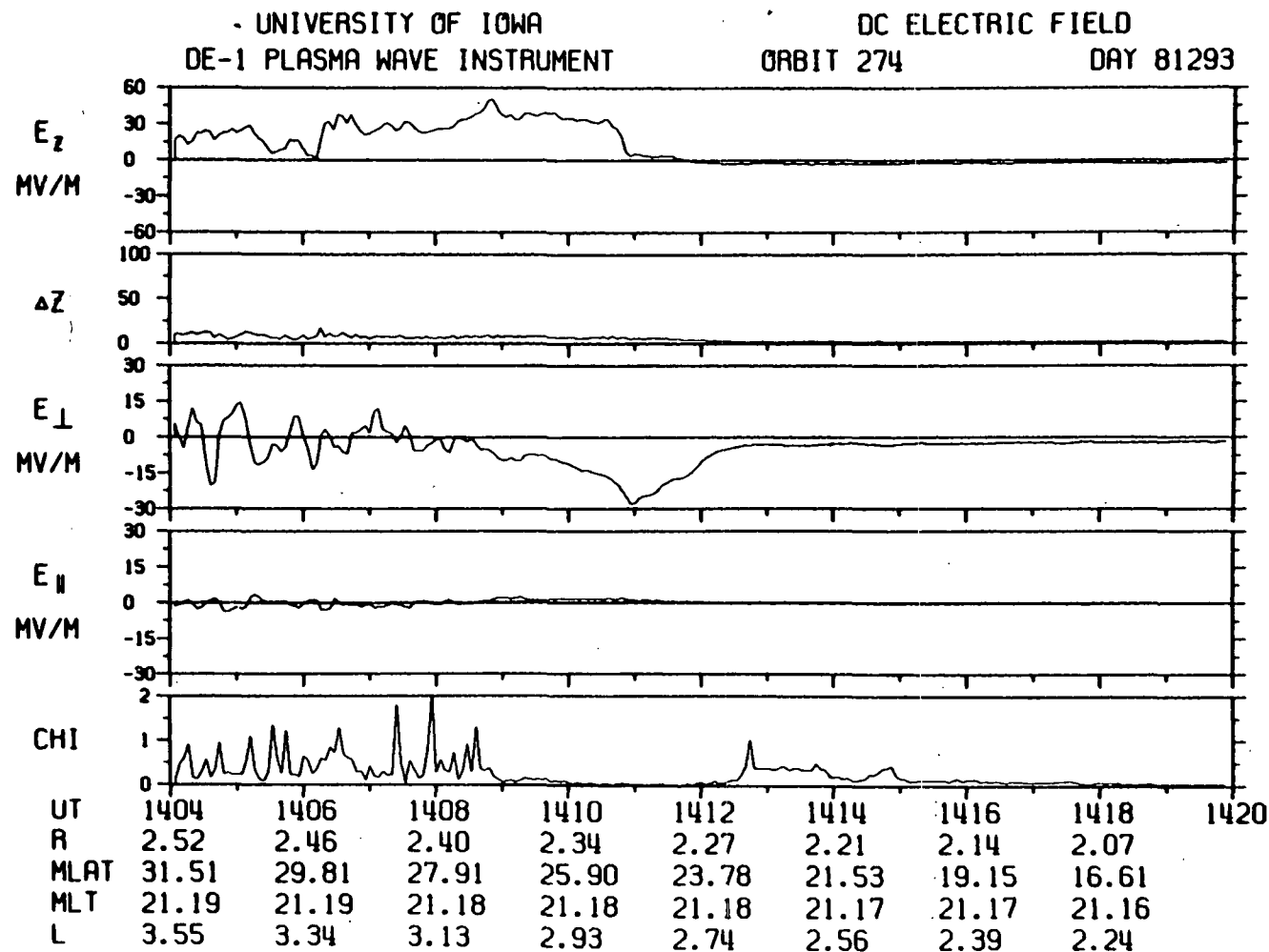


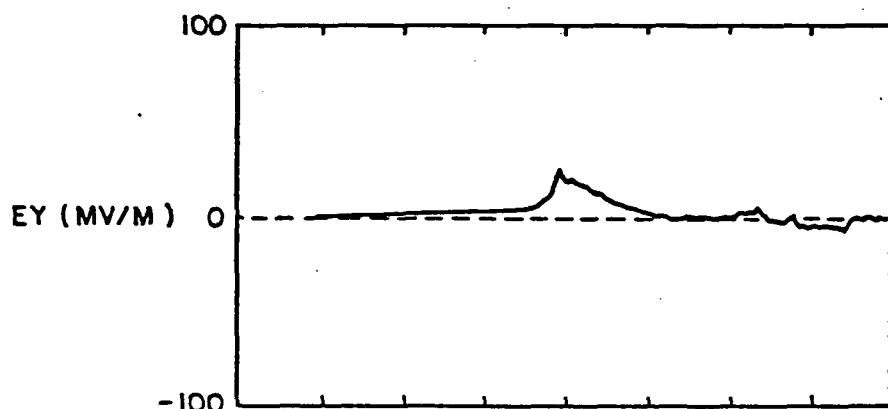
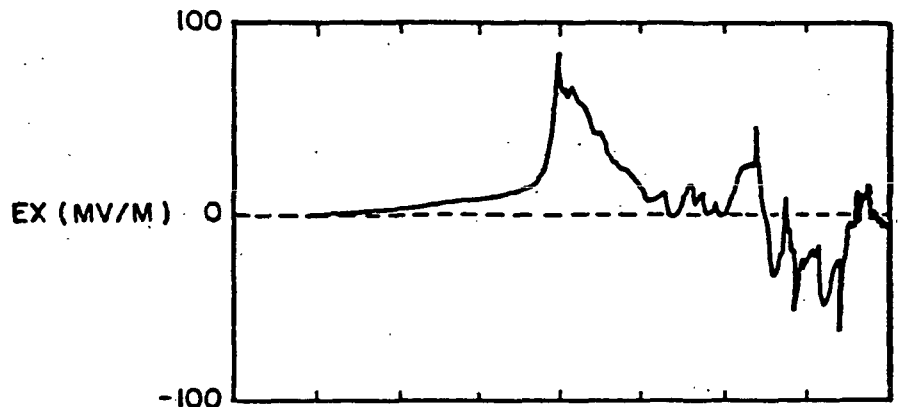
Figure 31

**Figure 32**

Electric field measurement from the VEFI experiment on the low-altitude DE-2 spacecraft. This data was obtained 70 minutes prior to the data shown in figure 31. DE-2 was on the same magnetic field lines but in the opposite hemisphere, so the electric field is a mirror image of the DE-1 data.

A-G83-273

DE-B VEFI 20 OCT 1981 - 81293 COORD: SPC  
ORBIT 1153



UT	13:16	13:18	13:20	13:22	13:24
INV. LAT.	39.9	48.2	56.5	64.6	72.6
MLT (H)	21.1	21.1	21.1	21.1	21.1
GLAT	-26.7	-34.3	-42.0	-49.7	-57.5
GLONG	112	112	111	111	110
ALT (KM)	564	527	491	458	428

Figure 32

POLAR CAP ELECTRON DENSITIES FROM  
DE-1 PLASMA WAVE OBSERVATIONS

by

Ann Marie Miller Persoon

A thesis submitted in partial fulfillment  
of the requirements for the degree of  
Master of Science in Physics  
in the Graduate College of  
The University of Iowa

May, 1983

Thesis supervisor: Professor Donald A. Gurnett

Graduate College  
The University of Iowa  
Iowa City, Iowa

CERTIFICATE OF APPROVAL

MASTER'S THESIS

This is to certify that the Master's thesis of

Ann Marie Miller Persoon

has been approved by the Examining Committee  
for the thesis requirement for the Master of  
Science degree in Physics at the May, 1983  
graduation.

Thesis committee: Daniel A. Knuttt  
Thesis supervisor

Stanley J. Hawk  
Member

Raymond T. Day  
Member

#### ACKNOWLEDGEMENTS

I would like to thank D. B. Muldrew of the Communications Research Centre, Department of Communications, Ottawa, Canada for the use of electron density profiles from the Alouette II and Isis-1 satellites. Density data from these profiles were used to obtain the median profile in Figure 15. I would also like to thank J. E. Jackson of Goddard Space Flight Center and J. Fennel of Aerospace Corporation for their valuable discussions on low-altitude density studies and J. L. Green and J. H. Waite, Jr. of Marshall Space Flight Center for their interesting discussions of ion composition and densities in the polar cap deduced from the Retarding Ion Mass Spectrometer on DE-1.

I would like to express my appreciation to Don Gurnett for his instruction and guidance during my years of study and research. His intuitive insight and helpful suggestions provided the inspiration and direction for this research project and his instructive comments transformed my early awkward efforts into a coherent scientific paper. I would like to thank all of those people whose knowledge and technical skill were largely responsible for transforming my vague ideas and rough sketches into a professional piece of literature: Terry Averkamp whose programming skills converted volumes of data into the instructive plots used in this study; Kathy Goodner whose patience and secretarial skills turned my poor penmanship and numerous rough drafts into

a finished paper; Joyce Chrisinger whose drafting skills changed my imperfect sketches into instructive illustrations; Mark Brown for his fine photography; and Rich Huff and his co-workers for their efforts in obtaining the electric field spectrum measurements used in this study. I would also like to thank all of the faculty members, research scientists, and fellow graduate students who contributed their time, knowledge and patience in countless discussions concerning this research. Their instruction, guidance and support have been invaluable.

This research was supported by NASA through Contracts NAS5-25690 and NAG5-310 with Goddard Space Flight Center, through Grants NGL-16-001-002 and NGL-16-001-043 from NASA Headquarters, and by the Office of Naval Research.

## ABSTRACT

Electric field spectrum measurements from the Plasma Wave Instrument on the Dynamics Explorer-1 spacecraft are used to determine the plasma frequency cutoff of whistler mode radiation at high altitudes over the northern polar cap region. This cutoff provides an accurate (less than 12%) determination of the local electron density. The median electron density over the polar cap at  $L$  greater than 10 is found to vary from  $35.2 \pm 8.5 \text{ cm}^{-3}$  at  $2.1 R_E$  to  $0.99 \pm 0.51 \text{ cm}^{-3}$  at  $4.66 R_E$ . Variations up to a factor or four occur from these median values.

The steady state radial outflow model is examined for consistency with the observed density profile. The model predicts an inverse dependence on the product of the plasma velocity and the cube of the radial distance. Comparison of the observed density profile with the radial outflow model yields a power law distribution for the electron density with an exponent of  $-3.85 \pm 0.32$ , which implies a flow velocity increasing nearly linearly with increasing radial distance. Comparison of the observed electron densities with theoretical polar wind densities yields consistent results up to  $2.8 R_E$ , although the steady-state solutions for supersonic  $H^+$  outflow are slightly lower than the observed median densities. Recent DE-1 measurements contradict polar

wind predictions of ion composition and energies, although a thermal polar wind component in the polar cap plasma is also present.

A comparison of observed electron densities with low-altitude density profiles from the Alouette II and Isis-1 spacecrafts indicates a transition in the radial dependence of the electron density at  $1.16 R_E$  and another transition between  $1.55 R_E$  and  $2.0 R_E$ . These transitions are due to changes in the basic processes of plasma transport with increasing radial distance in the polar cap region. A combination of a near diffusive equilibrium distribution and a subsonic outward plasma flow in the high density region below  $1.16 R_E$  becomes a supersonic, collision-dominated outward flux as the plasma density diminishes above  $1.16 R_E$ . A second transition in the density profile is expected between  $1.55 R_E$  and  $2.0 R_E$  when the collision-dominated radial outflow model below  $1.55 R_E$  develops into a collisionless power law distribution in the very low density regions of the polar cap at the height of the DE-1 orbit.

## TABLE OF CONTENTS

	Page
LIST OF FIGURES . . . . .	vii
I. INTRODUCTION . . . . .	1
A. Early Work on Electron Density Measurements . . . . .	2
B. Instrumentation of DE-1 . . . . .	4
II. METHOD OF ANALYSIS . . . . .	6
A. Plasma Wave Modes in the Polar Cap . . . . .	6
B. A Typical Spectrogram: Day 309, 1981 . . . . .	8
C. Identification of Plasma Frequency Cutoff . . . . .	10
D. Measuring the Plasma Frequency Cutoff . . . . .	10
III. REPRESENTATIVE ELECTRIC FIELD SPECTROGRAMS . . . . .	14
A. Day 278, 1981 . . . . .	14
B. Day 047, 1982 . . . . .	15
C. Day 046, 1982 . . . . .	16
D. Day 039, 1982 . . . . .	17
IV. THE ELECTRON DENSITY PROFILE . . . . .	19
V. COMPARISON OF THE DENSITY PROFILES WITH THEORETICAL MODELS . . . . .	22
A. Radial Outflow Model . . . . .	22
B. Polar Wind Solutions . . . . .	26
VI. COMPARISON OF THE HIGH-ALTITUDE DENSITY PROFILE WITH TOPSIDE SOUNDER MEASUREMENTS . . . . .	31
VII. DISCUSSION AND SUMMARY . . . . .	36
REFERENCES . . . . .	40
APPENDIX A: FIGURES . . . . .	43

## LIST OF FIGURES

	Page	
<b>Figure 5</b>	An electric field spectrogram of a polar cusp crossing in early October. . . . .	52
<b>Figure 6</b>	A nightside crossing of auroral field lines in mid-February illustrating a depletion in electron densities at $\lambda_m \approx 50^\circ$ [Calvert, 1981] and a smooth density profile inside the polar cap region. . . . . . . . .	54
<b>Figure 7</b>	A continuation of the same polar pass illustrated in Figure 6. . . . . . . . .	56
<b>Figure 8</b>	A spectrogram illustrating the time variability of the density profile. . . . .	58
<b>Figure 9</b>	Another nightside crossing of the auroral field lines in early February. . . . .	60
<b>Figure 10</b>	This pass follows the pass illustrated in Figure 9 by eight hours for the region of the polar magnetosphere just poleward of the nightside auroral zone. . . . . . .	62
<b>Figure 11</b>	A scatter plot of electron density as a function of radial distance. . . . . . .	64



## I. INTRODUCTION

In this report the electron density profile as a function of radial distance is determined using electric field spectrum measurements from the Plasma Wave Instrument on the Dynamics Explorer-1 spacecraft. The region of interest in this study is the earth's northern polar cap region where geomagnetic field lines are open into the magnetotail and a steady outward plasma flow occurs, resulting in lower electron densities than those observed equatorward of the auroral field lines. The polar cap region is defined to be the region of the magnetosphere poleward of the auroral field lines. Because the auroral zone varies with disturbances in the earth's magnetic field, the northern polar cap region, for purposes of this study, was taken to be that region of the magnetosphere with L-shell values greater than 10, or corresponding invariant latitudes greater than  $71.6^\circ$  ( $\Lambda = \cos^{-1} \sqrt{1/L}$ ).

The Dynamics Explorer-1 spacecraft, launched on August 3, 1981, is in an eccentric polar orbit with perigee and apogee geocentric radial distances of  $1.09 R_E$  and  $4.66 R_E$ , respectively. Because of the eccentricity and range of its orbit and the latitudinal precession of its apogee, this spacecraft provides electric and magnetic field data for a region of the polar magnetosphere not previously studied. Figure 1 illustrates the orientation of the DE-1 orbit in September, 1981, and

the precession of its apogee over the five-month period involved in this study--September, 1981 to February, 1982. The latitudinal precession of the DE-1 apogee is 108° per year. This precession is responsible both for the variations in the altitude of the spacecraft in the polar cap region and for the variations in the length of time the spacecraft spends in this region. During the five-month period covered in this study, the geocentric radial distance of DE-1 in the northern polar cap region varied from 2.0 RE to 4.66 RE, or 6378 km to 23,300 km above the earth's surface. This altitude range is far below the high altitude studies of the Hawkeye spacecraft and above the low altitude studies of the Alouette-Isis satellites and the S3-3 spacecraft.

#### A. Early Work on Electron Density Measurements

Prior to 1962, electron density measurements were obtained with the use of ground-based ionosondes [Calvert, 1966]. The bottomside sounding technique employed by the ionosondes was based on the principle of the vertical reflection of pulsed radio waves by ionospheric electron densities, which were related to the sounding frequencies of the waves. The altitude of the reflecting density layers was derived from the measured time delay between the transmitted signal and the reflected echo. This technique was limited to an analysis of electron number densities below the height of maximum ionization of the ionosphere (F2 peak). Transmitted signals with sounding frequencies that exceeded the critical reflection frequency corresponding to this maximum electron density would pass through the ionosphere and would not be reflected. Data from the ground-based ionosondes were used to

construct electron density profiles as a function of altitude only for the region of the ionosphere below the peak of the F2 layer.

To study the electron density profile above the F2 peak, topside sounders, similar in concept and operation to the ground-based ionosondes, were designed to operate on orbiting satellites. The first topside sounder satellite, Alouette I, was launched on September 29, 1962, into a nearly circular polar orbit at 1000 km [Jackson and Warren, 1969; Florida, 1969]. It provided electron density profiles from the F2 peak up to the height of its orbit. This altitude coverage of electron density measurements was expanded to nearly 3000 km by Alouette II, which was launched into an elliptical polar orbit on November 29, 1965 [Jackson and Warren, 1969; Florida, 1969]. Altitude coverage was further expanded by Isis-1 which was launched on January 30, 1969, into an elliptical polar orbit with an apogee of nearly 3500 km [Florida, 1969]. Isis-2, the last satellite in the Alouette-Isis series, was launched on April 1, 1971, into a circular polar orbit at 1400 km. Like its three predecessors, this satellite carried a swept-frequency sounder capable of making the electron density measurements subsequently used to construct vertical electron density profiles. Isis-2 also carried a Langmuir probe instrument, capable of making local measurements of electron density and temperature in the vicinity of the spacecraft [Florida, 1969; Coordinated Ionospheric and Magnetospheric Observations from the Isis 2 Satellite, 1980].

The S3-3 satellite, launched in the summer of 1976, also carried a Langmuir probe instrument to measure electron number densities and density fluctuations along the satellite orbit [Mozer et al., 1979]. The S3-3 orbit was an elliptical polar orbit with an apogee of 8000 km, but electron density measurements in the polar cap region have not yet been published. Above 8000 km, one spacecraft to cross the northern polar cap region was the Hawkeye I spacecraft. It was launched on June 3, 1974, into a highly eccentric orbit with a polar apogee of  $20.5 R_E$ . Due to the precession of its apogee during its four-year lifetime, the Hawkeye spacecraft was able to obtain electric and magnetic field measurements and corresponding charge particle measurements at large radial distances up to  $20 R_E$  in the polar cap region [Gurnett and Frank, 1978]. But, because of the eccentricity of its orbit, there was a gap in the Hawkeye data measurements below approximately  $8 R_E$ . Although density measurements at higher altitudes in the polar cap region could be derived from the Hawkeye electric field measurements [Calvert, 1981], to date no such results have been published.

#### B. Instrumentation of DE-1

The Plasma Wave Instrument (PWI) on Dynamics Explorer-1 has been described in detail in a previous report [see Shawhan et al., 1981]. The instrument is designed to measure AC electric fields over a frequency range of 1 Hz to 2 MHz and an amplitude range of  $0.03 \mu V m^{-1}$  to  $100 mV m^{-1}$ , in addition to magnetic fields and quasi-static electric fields. The antenna system used in measuring these AC electric fields consists of a pair of electric antennas mounted orthogonally to each

other. One 9m tubular antenna is oriented parallel to the spin axis and a 215m long wire antenna is oriented perpendicular to the spin axis. Signals from these sensors are received by two of the PWI receiver systems, the Step Frequency Correlator (SFC) and the Low Frequency Correlator (LFC). The Step Frequency Correlator consists of a correlator and two identical Step Frequency Receivers (SFR) with four frequency bands, each containing 32 frequency steps, scanning a frequency range of 100 Hz to 400 kHz every 32 seconds. The Low Frequency Correlator consists of a correlator and two identical spectrum analyzers with eight filters, scanning a frequency range of 1.78 Hz to 100 Hz every 32 seconds. The resulting electric field amplitude measurements are displayed in frequency-time spectrogram form, covering a two-hour time interval and spanning a frequency range of 1.78 Hz to 400 kHz.

## II. METHOD OF ANALYSIS

### A. Plasma Wave Modes in the Polar Cap

Electric field spectrograms obtained from the electric field amplitude measurements of the PWI illustrate features of the various modes of plasma waves observed by DE-1 for frequencies in the vicinity of the electron gyrofrequency and the electron plasma frequency. There are four plasma wave modes predicted by cold plasma theory for this frequency range [Stix, 1962]. These modes are the free space L-0 (left-hand polarized, ordinary) mode, the free-space R-X (right-hand polarized, extraordinary) mode, the Z-mode (extraordinary) and the whistler mode (right-hand polarized). Regions of allowed propagation for these various modes are summarized in the CMA diagrams of Figure 2. These CMA diagrams are derived from the two-component plasma CMA diagrams of Stix [1962, Chap. 2] and Chen [1974, Chap. 4] for a plasma composed of electrons and infinitely massive ions with frequencies near the electron gyrofrequency and the electron plasma frequency. The use of the infinitely massive ion component in this plasma model is justified since the dominant ion for the majority of the polar passes is H<sup>+</sup> and this ion is 10<sup>3</sup> times more massive than the electron.

The vertical axis in Figure 2 is the electron gyrofrequency-wave frequency ratio and the horizontal axis is the square of the electron plasma frequency-wave frequency ratio. Figure 2(a) illustrates the

regions of allowed propagation for the free space R-X mode and the Z-mode. The free space R-X mode has a low frequency cutoff at  $f(R=0) = \frac{f_g}{2} + ((\frac{f_g}{2})^2 + f_p^2)^{1/2}$ . The Z-mode is bounded at low frequencies by  $f(L=0) = -\frac{f_g}{2} + ((\frac{f_g}{2})^2 + f_p^2)^{1/2}$  and at high frequencies by the upper hybrid resonance,  $f_{UHR} = (f_g^2 + f_p^2)^{1/2}$ . Figure 2(b) illustrates the regions of allowed propagation for the free space L-O mode and the whistler mode. The free space L-O mode has a low frequency cutoff at the electron plasma frequency. The whistler mode is confined to frequencies below the electron gyrofrequency or the electron plasma frequency, whichever is smaller.

These four plasma wave modes have been associated with electromagnetic plasma wave emissions found in the auroral zone and polar cap region [Gurnett et al., 1983]. Broadband electromagnetic emissions propagating below the electron gyrofrequency in the auroral zone (where  $f_g < f_p$ ) are called auroral hiss. These emissions are believed to be propagating in the whistler mode [Gurnett et al., 1983] because this is the only electromagnetic plasma wave mode propagating in this frequency range (see Figure 2(b)). Auroral hiss is believed to be generated by low energy (100 eV to 10 keV) electrons moving upward along auroral field lines [Gurnett and Frank, 1972] from a region of electron acceleration between  $1.7 R_E$  and  $1.9 R_E$  [Gurnett et al., 1983]. Intense, high-frequency emissions called auroral kilometric radiation (AKR) have also been identified on the PWI electric field spectrograms. This radiation is generated along auroral field lines between  $2 R_E$  and  $4 R_E$  [Gallagher and Gurnett, 1979] and escapes from the earth's

magnetosphere. Recent polarization measurements of AKR by Shawhan and Gurnett [1982] have determined that the dominant component of AKR is right-hand polarized and the radiation propagates in the free space R-X mode. Z-mode radiation has been identified as broadband emissions in the auroral zone by Calvert [1981] and Gurnett et al. [1983]. It can be seen on the following spectrograms that Z-mode radiation extends into the polar cap region with larger bandwidths because of the lower plasma density.

B. A Typical Spectrogram: Day 309, 1981

A typical example of an electric field spectrogram illustrating these various wave modes is shown in Figure 3. The trajectory of the spacecraft in a magnetic meridian plane is shown in the lower left corner of the spectrogram. The spacecraft is approaching the nightside auroral region from a radial distance of  $4.2 R_E$  and  $79^\circ$  magnetic latitude and entering the auroral zone at  $47^\circ$  magnetic latitude and a radial distance of  $2.6 R_E$ . Intense emissions in the high frequency range are auroral kilometric radiation, electromagnetic emissions characteristically found in the 100 - 400 kHz frequency range [Shawhan, 1979; Gurnett et al., 1983]. The apparent lower frequency cutoff of auroral kilometric radiation is an instrumentation effect; the low frequency cutoff of the Step Frequency Receivers' fourth frequency band is located at 58 kHz. Emissions in the 15 - 60 kHz range are Z-mode radiation, electromagnetic emissions with a characteristic upper frequency cutoff located at the upper hybrid resonance frequency [Shawhan, 1979; Gurnett et al., 1983]. In this spectrogram, the Z-mode

radiation exhibits a sharply defined upper frequency cutoff at the electron gyrofrequency on the poleward side of the auroral zone. In this region, lower electron densities result in an electron plasma frequency that is much lower than the local electron gyrofrequency. Under these circumstances, the upper hybrid resonance frequency is approximately equal to the local electron gyrofrequency and the latter will become the upper frequency cutoff for the Z-mode.

Intense emissions below 20 kHz which spread out from the auroral region toward the pole are auroral hiss emissions. Auroral hiss is commonly observed between 10 Hz and 100 kHz. Figure 3 illustrates the funnel-shaped lower frequency cutoff of auroral hiss emissions in the auroral zone, a feature that is frequently but not always observed at the altitude of the DE-1 orbit [Gurnett et al., 1983]. Auroral hiss is not confined to the auroral zone but spreads out over a wide range of latitudes on the poleward side of the auroral zone. Stronger damping effects due to the hot magnetospheric plasma in the plasmasphere and plasmapause inhibit the propagation of auroral hiss at lower latitudes. Auroral hiss emissions are also found in the dayside polar cusp (see Figure 5) and exhibit a similar latitudinal asymmetry in the direction of the pole, resulting in a nearly continuous band of emissions over the polar cap region (see Figures 6 and 7). Figure 4 is an illustration of the propagation of auroral hiss emissions into the polar cap region from sources located at approximately  $1.8 R_E$  in the auroral zone and polar cusp. The representative ray paths for a source located at  $1.8 R_E$  have been determined by Gurnett et al. [1983] to fit the lower frequency cutoff of auroral hiss emissions observed by DE-1.

### C. Identification of Plasma Frequency Cutoff

Auroral hiss is whistler mode radiation which, according to plasma wave theory, has a characteristic upper frequency cutoff located at either the electron gyrofrequency or the electron plasma frequency, whichever is smaller [Stix, 1962; Chap. 2; Chen, 1974, Chap. 4]. In the polar cap region, the electron plasma frequency is generally much smaller than the electron gyrofrequency. The electron plasma frequency then gives the upper frequency cutoff for the whistler mode radiation in the polar cap region. In Figure 3, the plasma frequency cutoff is well-defined and varies smoothly from 16 to 19 kHz. It divides the auroral hiss emissions below from the Z-mode radiation above.

### D. Measuring the Plasma Frequency Cutoff

Spectrograms, such as the one in Figure 3, were constructed from the digitized data output of the Step Frequency Receivers. The digitized data was displayed on a video monitor in spectrogram form. A digitizing cursor was used to trace the plasma frequency cutoff on the spectrogram and a frequency value was recorded for each sweep of the Step Frequency Receiver (every 32 seconds). In addition, orbit parameters of the spacecraft, such as magnetic latitude and radial distance, were indexed to each 32-second time interval. From a knowledge of the electron plasma frequency, the electron number density was derived, using the well-known relation:

$$f_p = 9\sqrt{n_e}$$

where  $f_p$  is the electron plasma frequency in kHz and  $n_e$  is the electron number density in  $\text{cm}^{-3}$ .

In addition to using the video monitor and cursor for tracing the plasma frequency cutoff on the spectrogram, the quality of each frequency value was monitored with the use of a quality control index. The index was assigned to each data point in order to isolate data of questionable reliability on spectrograms where the intensity of the whistler mode radiation approached the intensity of the background noise and the upper frequency cutoff was no longer clearly defined. The use of the quality control index made it possible to study the effect of marginally reliable data on the density profile and to locate spurious data points.

For spectrograms in which the upper frequency cutoff was not clearly defined, intensity enhancement techniques were employed to accent the plasma frequency cutoff and minimize background noise and Z-mode radiation. Enhancement techniques were helpful in locating the frequency cutoff when the intensity of the Z-mode radiation approached the intensity of the whistler mode radiation, thereby partially obscuring the plasma frequency cutoff. This effect is evident after 0550 in Figure 3. A 16-point sliding grey scale provided the capability of enhancing the intensity of segments of the frequency range by raising the minimum intensity levels above the maximum intensity of the background noise and lowering the maximum intensity levels displayed on the monitor screen. The remaining narrower intensity range would be spanned by 16 shades from white (lowest intensity) to black (highest intensity). Such enhancement techniques were necessary since the

accurate determination of the electron number density depended on the measurement of a well-defined plasma frequency cutoff.

The combined use of intensity enhancement techniques and tracing the frequency cutoff with a cursor permitted the determination of the frequency cutoff to a high degree of accuracy. The top three SFR frequency bands (900 Hz - 40 kHz) were divided into 96 frequency indices. The cursor could locate the frequency cutoff within a frequency index. At 10 kHz, a typical frequency cutoff value, the frequency cutoff could be determined within  $\pm 600$  Hz, corresponding to an uncertainty in the calculated number density of  $\pm 12\%$ . This uncertainty is negligible compared to the observed spread in density values due to diurnal and latitudinal variations, as well as anticipated large scale variations, due to magnetic field activity and the solar sunspot cycle.

A smaller source of error comes from the identification of the cutoff frequency with the electron plasma frequency. Hot plasma effects such as cyclotron damping and Landau damping can cause the whistler mode wave to cut off at frequencies below the electron plasma frequency. These effects, however, are expected to be small. Because of the small resonance angle of the whistler mode at resonance and the subsequently high index of refraction required for Landau damping, this effect will only be significant in a narrow band of frequencies just below the plasma frequency. Only particles with frequencies in this band will resonate with the wave. For frequencies in the range of  $f_p \pm 2$  kHz, the Landau damping effect would imply an error in the calculated number density of approximately 5% for  $f_p = 10$  kHz. Cyclotron damping will have a significant effect on the cutoff frequency only in the

region of the electron gyrofrequency. A statistical comparison of the electron gyrofrequency and the observed cutoff frequency on the electric field spectrograms indicated that the cutoff frequency was equal to or greater than  $0.9 f_g$  for less than 10% of all data points over most radial distances in this study (see Section IV). Consequently, the cyclotron damping effect implies an error in the calculated number density of less than 3% for 7% of all density data points. The effect is expected to be much smaller than the Landau damping effect.

The method of determining the electron number density from a measured plasma frequency cutoff has a significant inherent limitation. The plasma frequency can be determined with the aforementioned accuracy only for those spectrograms where the cutoff is reasonably well-defined. Of the more than 750 electric field spectrograms examined in this study, only 40% have observable upper frequency cutoffs for at least some fraction of the two-hour time interval of the spectrogram. The quality of the upper frequency cutoff on these spectrograms varies with the intensity of the whistler mode radiation as well as the background noise and the other plasma wave modes propagating near the upper frequency cutoff. The quality of the frequency cutoff was particularly biased toward the lower polar latitudes. Few well-defined frequency cutoffs could be found for magnetic latitudes above  $85^\circ$ . The intensity of auroral hiss emissions propagating into the polar cap from lower auroral latitudes diminishes with increasing latitude. Frequently, at high polar latitudes, auroral hiss emissions could not be distinguished from the background noise.

### III. REPRESENTATIVE ELECTRIC FIELD SPECTROGRAMS

#### A. Day 278, 1981

The electron plasma frequency cutoff, indicated on the spectrogram in Figure 5, is well-defined up until 0840 as the satellite nears the pole. The spectrogram is from early October, 1981, when the satellite's apogee had precessed about  $15^\circ$  to the dayside of the pole. The panel in the lower left-hand corner of the spectrogram indicates the satellite's trajectory. DE-1 is emerging from the dayside polar cusp at  $4.3 R_E$  with a magnetic latitude of  $59^\circ$  and approaching the pole at  $4.6 R_E$  and  $78^\circ$  magnetic latitude at 0858 where there is a data gap. Intense AKR is again evident above 100 kHz and Z-mode radiation, less intense than it was in Figure 3, is found between 10 kHz and 20 kHz at 0755. As in Figure 3, the auroral hiss emissions are latitudinally asymmetric, spreading out over the polar cap region in the direction of the pole. However, the funnel-shaped lower frequency cutoff of the auroral hiss in the auroral zone is not evident in this spectrogram. Below  $78^\circ$  magnetic latitude, the electron plasma frequency is smoothly varying, decreasing with increasing radial distance. Exceptions are the sharp spike in the plasma frequency cutoff at 0752 and several spikes after 0845, indicating a sudden increase in the electron number density by more than a factor of two.

B. Day 047, 1982

The two spectrograms in Figures 6 and 7 were chosen to illustrate one continuous pass of DE-1 over the polar cap. This pass occurred in mid-February of 1982 when the spacecraft apogee had precessed into the nightside auroral zone. In Figure 6, the spacecraft is in and emerging from the auroral zone as illustrated in the panel in the bottom left-hand corner of the spectrogram. It passes through apogee at approximately 0350 and emerges from the auroral zone shortly after 0400, with a range in magnetic latitude of  $34^\circ$  to  $69^\circ$ . In the polar cap region, the plasma frequency cutoff of the whistler mode radiation is sharply defined and constant at approximately 10 kHz. The Z-mode radiation above the auroral hiss is less intense and again exhibits a sharp upper-frequency cutoff at the electron gyrofrequency.

The spectrogram in Figure 7 is a continuation of the two-hour spectrogram in Figure 6. The spacecraft is in the northern polar cap region for most of this time interval, passing over the pole at approximately 0600. The vertical white lines on the spectrogram indicate short data gaps. The radial distance of the spacecraft for this spectrogram varies from  $4.4 R_E$  with a magnetic latitude of  $62^\circ$  on the nightside of the pole to  $1.8 R_E$  with a magnetic latitude of  $44^\circ$  on the dayside of the pole. The spacecraft enters the polar cusp at approximately 0640, as indicated by the onset of broadband auroral hiss emissions at that time. The plasma frequency cutoff in Figure 7 is again sharply defined and is generally constant at about 16 kHz before the spacecraft crosses the pole. However, there is an abrupt 12% decrease in magnitude at a magnetic latitude of  $84^\circ$  on the dayside of the pole

(at 0604) and a steady increase in the plasma frequency after 0625 with decreasing radial distance. Generally, though, the plasma frequency in Figures 6 and 7 exhibits few variations on a short time scale and the resulting electron density profile for this orbital pass is smoothly varying.

C. Day 046, 1982

However, the plasma frequency is not smoothly varying for the orbital pass which immediately precedes the pass illustrated in Figures 6 and 7. In Figure 8 the spacecraft is in the same region of the polar magnetosphere as it is in Figures 6 and 7, only 5 hours earlier. As indicated in the panel in the lower right-hand corner, DE-1 is emerging from the nightside auroral zone into the northern polar cap region. In this two-hour interval, the radial distance of the spacecraft varies from  $4.4 R_E$  with a magnetic latitude of  $47^\circ$  on the nightside of the pole to  $1.8 R_E$  with a magnetic latitude of  $51^\circ$  on the dayside of the pole.

The radiation seen below 50 kHz in Figure 8 is electromagnetic and propagates at frequencies below the electron gyrofrequency in a region of the polar magnetosphere where  $f_p \ll f_g$ . Whistler mode radiation is the only electromagnetic plasma wave mode that can propagate in this frequency range (see Figure 2b)). This whistler mode radiation, however, is not the usual type of auroral hiss associated with the auroral zone since it is believed to be generated at high magnetic latitudes poleward of the auroral field lines [S. D. Shawhan, personal communication]. This radiation may be associated with the polar cap aurora or other aurora-like processes over the polar cap.

Since this radiation is whistler mode radiation, the upper frequency cutoff visible in Figure 8 is the electron plasma frequency. Unlike the plasma frequency cutoff in Figures 6 and 7, the plasma frequency cutoff in Figure 8 is highly variable on time scales of 8 minutes to less than one minute, indicating variations in the electron number density of an order of magnitude or more on spatial scales of 50 - 1400 km.

D. Day 039, 1982

The variability in the character of the electron density profile between successive orbital passes of the spacecraft is again illustrated in Figures 9 and 10. The spectrograms in these figures are from successive passes of the spacecraft, emerging from the nightside auroral zone in early February, 1982. In Figure 9, the spacecraft exits the auroral zone at 0400 at a radial distance of  $4.6 R_E$  and a magnetic latitude of approximately  $45^\circ$  and passes through apogee in the polar cap region about 10 minutes later. In this spectrogram, the electron plasma frequency varies smoothly between 9 kHz and 13 kHz with few abrupt changes on a short-time scale, indicating changes in the electron number density by a factor of 2 or less.

On the following orbital pass (Figure 10) the spacecraft again emerges from the nightside auroral zone at 1140 (approximately 7.5 hours later) at a radial distance of  $4.5 R_E$  and a magnetic latitude of  $50^\circ$ . The radial distance of the spacecraft in the polar cap region for this pass varies from  $4.5 R_E$  with a magnetic latitude of  $50^\circ$  to  $3 R_E$  with a magnetic latitude of  $78^\circ$  on the nightside of the pole. Unlike

the preceding pass, the electron plasma frequency cutoff on this spectrogram is not smoothly varying. There is a general tendency for the plasma frequency to increase in magnitude with decreasing radial distance as the spacecraft nears the pole, as it did in Figure 5. But more striking are the large variations in the magnitude of the plasma frequency on time scales of 5 minutes or less, indicating variations in the electron number density up to one order of magnitude on spatial scales of less than 700 km. The electron density profile for this orbital pass is not as smoothly varying as it was in Figure 9.

#### IV. THE ELECTRON DENSITY PROFILE

To obtain the electron density profile in the northern polar cap region, the electron plasma frequency was numerically determined from the analysis of nearly one hundred 2-hour electric field spectrograms, selected from the five-month time interval of September, 1981, to February, 1982. The electron number density was calculated from the plasma frequency using the relation:  $f_p = 9\sqrt{n_e}$ , where  $f_p$  is in kHz and  $n_e$  is in  $\text{cm}^{-3}$ . Figure 11 is a semilog plot of the calculated electron number density as a function of radial distance. This plot illustrates the wide scatter in the observed electron density for a given radial distance. The scatter was not unexpected since the electron densities have been obtained over a wide range of magnetic latitudes for a given radial distance. The electron density data also includes a wide range of magnetic field conditions and large variations are observed from orbit to orbit. On the average, during the five months immediately following the launch of DE-1, magnetic activity was relatively high ( $k_p \approx 3$ ), although magnetic field conditions were subject to change on time scales less than the period of the DE-1 orbit. Nevertheless, despite the resulting spread in density values for a given radial distance, the expected decrease in electron density with increasing radial distance is clearly evident.

The observed upper density cutoff in Figure 11 corresponds to the electron gyrofrequency as a function of radial distance. Electron number densities can be determined from the whistler mode cutoff frequency only when the electron plasma frequency is lower than the electron gyrofrequency. When the electron plasma frequency exceeds the gyrofrequency, the electron density calculated from the cutoff frequency (now the electron gyrofrequency) merely represents a lower limit on the actual electron density. A statistical tabulation of the data points for which the cutoff frequency was greater than 90% of the electron gyrofrequency indicated that the electron gyrofrequency contaminated the calculation of electron densities in only 1% of the cases at  $2.0 R_E$  to 11% of the cases for radial distances greater than  $4.0 R_E$ .

To further explore the relationship between electron density and radial distance and to determine the spread in number density values for a given altitude, the radial range was divided into radial increments of  $0.25 R_E$  and the median value of the electron number density was computed for each radial increment. Median values were used to minimize the effect of number density values greater than the gyrofrequency density values. Since the majority of the data points cluster in a band below the "gyrofrequency cutoff" in Figure 11, the median values are negligibly affected by the relatively few discarded density values located above the gyrofrequency cutoff. Figure 12 is a log-log plot of the median electron number density as a function of radial distance. The error bars indicate quartiles, illustrating the spread in 25% of the data on either side of the median values. These median number densities range from  $35.2 \pm 8.5 \text{ cm}^{-3}$  at  $2.0 R_E$  to  $0.99 \pm 0.51$

$\text{cm}^{-3}$  at  $4.5 R_E$ . Variations up to a factor of 4 occur from these median values. The calculation of the slope of the best line fit through these median values indicates a power law relationship between the electron number density and radial distance with an exponent of  $-3.85 \pm 0.32$ .

## V. COMPARISON OF THE DENSITY PROFILES WITH THEORETICAL MODELS

### A. Radial Outflow Model

In the high density low-latitude region of the Earth's magnetosphere, plasma is contained on closed magnetic field lines and exists in a state of near-diffusive equilibrium [Dessler and Michel, 1966; Dungey, 1961]. However, diffusive equilibrium solutions are derived from a Maxwellian velocity distribution in a collision-dominated regime [Bauer, 1969]. At high geomagnetic latitudes, electron densities can be very low above  $1.24 R_E$  [Hagg, 1967; Timleck and Nelms, 1969]. Field lines are open to interplanetary space in the magnetotail region where the boundary plasma pressure is very low and an outward flow of ionospheric ions results [Banks and Holzer, 1968, 1969b]. This outward flux of predominantly light ions has been called the polar wind [Axford, 1968].

The existence of an upward, field-aligned flux of protons, predicted by the polar wind theory, was confirmed by Explorer XXXI. The ion mass spectrometer on this satellite, launched simultaneously with Alouette II, detected an upward proton flux in the low plasma density region of the polar cap above 1000 km [Hoffman, 1969; Hoffman and Dodson, 1980]. At the higher altitudes of the DE-1 orbit, the Retarding Ion Mass Spectrometer and the Energetic Ion Composition Spectrometer have both detected a similar flux of lighter ions ( $H^+$  and  $He^+$ ) in the polar cap region [Chappell et al., 1982a; Shelley et al., 1982].

However, a significant flux of N<sup>+</sup> ions [Chappell et al., 1982b] has also been detected, and recent measurements have discovered a peak in the flux of the O<sup>+</sup> ion [Shelley et al., 1982] which appears to be associated with periods of increased magnetic activity with k<sub>p</sub> > 5 [J. H. Waite, personal communication].

A simplified illustration of the observed ion flux at high geomagnetic latitudes is shown in Figure 13. Since the ion fluxes detected by DE-1 are field-aligned, the ion flux tube follows the magnetic field geometry. An ion flux perpendicular to the magnetic field lines also exists in this region of the polar magnetosphere due to the magnetic convection cycle [Banks and Holzer, 1969b]. The individual ion continuity equation can be written in the form

$$\frac{\partial n_i}{\partial t} + \vec{\nabla} \cdot (n_i \vec{U}_i) = q_i - l_i$$

where n<sub>i</sub> is the ion number density,  $\vec{U}_i$  is the ion flow velocity, q<sub>i</sub> is the ion production rate and l<sub>i</sub> is the ion loss rate.

Adopting steady state conditions, the first term tends to zero. Although steady state conditions do not exist at all times in the polar magnetosphere, steady state is a justifiable first-order approximation when density data is time-averaged over several months, minimizing variations on a short time scale. For the low neutral particle density regions of the polar magnetosphere at the height of the DE-1 orbit, the ion loss and production terms are assumed to be negligible so that the continuity equation becomes

$$\vec{\nabla}_{\parallel} \cdot (n_i \vec{U}_{i\parallel}) + \vec{\nabla}_{\perp} \cdot (n_i \vec{U}_{i\perp}) = 0$$

where the terms in parentheses refer to the divergence of the ion flux parallel and perpendicular to the magnetic field. The constancy of the magnetic field in the polar cap requires a zero divergence of the perpendicular flow velocity. Although latitudinal variations in the number density suggest a non-zero divergence in the perpendicular flux, it is assumed, in a first order approximation, that this divergence is negligibly small. With these approximations, the continuity equation of a simple radial outflow model requires that

$$n_i u_i A = \text{constant}$$

where  $u_i$  is the ion flow velocity parallel to the magnetic field and  $A$  is the cross-sectional area of the flux tube at a given radial distance (see Figure 13).

The conservation of magnetic flux requires that

$$AB = \text{constant}$$

where  $B$  is the magnetic field intensity. A first order dipole approximation for the magnetic field in the polar cap region is

$$B \propto R^{-3}$$

This approximation is valid over a considerable radial range in the polar magnetosphere and leads to a relationship between the cross-sectional area of a magnetic flux tube and the radial distance:

$$A \propto R^3$$

The continuity equation for the steady state radial outflow of plasma along magnetic field lines, neglecting ion loss and production, predicts that

$$n_i \propto u_i^{-1} R^{-3}$$

where  $A \propto R^3$  has been substituted for the cross-sectional area of the flux tube in the continuity equation. The condition of electrical neutrality in the polar cap region requires that

$$n_e = \sum_i Z_i n_i$$

where  $Z_i$  is the charge state of the individual ion species. Since  $H^+$  is generally the dominant ion in the polar cap, the leading term in the summation is  $n_{H+}$  where  $n_{H+}$  is the singly charged hydrogen ion number density. It follows that, to a first order approximation,  $n_e \approx n_{H+}$  so that

$$n_e \propto u^{-1} R^{-3}$$

where  $u$  is the plasma flow velocity along the magnetic field line. A constant plasma flow velocity would place an upper limit on the exponent of a power law distribution of -3:

$$n_e \propto R^{-3} \text{ for } u = \text{constant}$$

This power law distribution is the asymptotic limit of the polar wind solution derived by Banks and Holzer [1968].

The development of steady-state solutions for high-latitude plasma transport by Banks and Holzer [1969a,b] and by Schunk and Watkins [1981, 1982] indicated an increase in the flow velocity with increasing radial distance. Thus, an exponent greater than 3 in Figure 12 is consistent with the expected relationships of radial distance with flow velocity and cross-sectional area in the polar cap region. It is reasonable to expect that  $n_e \propto R^{-\gamma}$  where  $\gamma > 3$ , if a valid power law relationship exists between electron number density and radial distance. Our best data fit in Figure 12,  $n_e \propto R^{-3.85}$ , indicates a plasma flow velocity increasing almost linearly with increasing radial distance.

#### B. Polar Wind Solutions

The newly discovered dominance of the oxygen ion for some DE-1 polar passes was unexpected [Shelley et al., 1982]. The classic polar wind theory predicted a large flux of lighter ions along open magnetic field lines at high latitudes, due to low plasma pressure in the geomagnetic tail. It was postulated that the loss of light ions from the

topside polar ionosphere would result in a dominance of the  $O^+$  ion to an altitude of 4000 km to 7500 km. Above this altitude a substantial, though rapidly diminishing, upward  $O^+$  flux would exist to support the dominant  $H^+$  flux through charge-exchange reactions.

In their theoretical study of multi-ion plasma transport at high geomagnetic latitudes, Banks and Holzer [1969b] derived a set of solutions to the standard hydrodynamic transport equations for various neutral atmosphere models and a range of isotropic, equal electron and ion temperatures. At an altitude of 7000 km ( $2.18 R_E$ ), their predicted electron densities ranged from approximately  $80 \text{ cm}^{-3}$  to nearly  $1000 \text{ cm}^{-3}$ . These densities exceed our observed densities at  $2.25 R_E$  by a factor of 5 to 50.

Banks and Holzer [1969b] also derived a set of predicted ion densities for different neutral atmosphere temperatures and a range of equal electron and ion temperatures. Predicted  $O^+$  densities were found to vary from  $10 \text{ cm}^{-3}$  to  $200 \text{ cm}^{-3}$  and  $H^+$  densities from  $90 \text{ cm}^{-3}$  to  $120 \text{ cm}^{-3}$  at 7000 km. The altitude of the transition from dominant  $O^+$  at low altitudes to dominant  $H^+$  at higher altitudes was found to vary between 4000 km and 7500 km, depending on the initial concentration of hydrogen in the neutral atmosphere model.

When electron and ion temperatures were allowed to vary individually and anisotropic temperature distributions were included in the analysis of high-latitude plasma transport, the predicted ion density profiles were altered and the transition to a dominance of the  $H^+$  ion was discovered to occur at even lower altitudes. In 1982, Schunk and Watkins [1982] developed a set of steady-state solutions for the

high-latitude plasma flow in the altitude range of 1500 km to 12,000 km. Their solutions were derived from the 13-moment system of transport equations which included continuity, momentum, internal energy, stress tensor and heat flow equations for electrons and oxygen and hydrogen ions. The solutions were determined for a range of lower boundary conditions which included the H<sup>+</sup> drift velocity, electron and H<sup>+</sup> temperature gradients, ion number densities, electron and H<sup>+</sup> temperatures and heat fluxes for the electrons and ions at 1500 km. Isis-2 provided the measurements of the hydrogen ion number density, drift velocity and temperature at the base reference level and S3-3 provided electron temperature measurements and a range of possible electron temperature gradients at the reference level.

Schunk and Watkins [1982] published ion density predictions both for supersonic ( $M > 1$ ) and subsonic ( $M < 1$ ) H<sup>+</sup> outflows where the Mach number M refers to the ratio of ion flow velocity to the thermal velocity. The 13-moment transport equations predict a significant electron temperature anisotropy ( $T_{e\perp} > T_{e\parallel}$ ) for the supersonic H<sup>+</sup> outflow and an isotropic electron temperature distribution at this altitude range for a subsonic flow. Both sets of ion density predictions are presented in Figure 14 for two lower boundary electron temperature gradients ( $\nabla T_e = 0.1^\circ K km^{-1}$ ,  $\nabla T_e = 1^\circ K km^{-1}$ ). As the boundary electron temperature gradient increases, the solutions for the supersonic H<sup>+</sup> outflow show a decrease in the hydrogen ion density and a slight increase in the oxygen ion density. Charge neutrality demands that

$$n_e = \sum_i Z_i n_i$$

and it can be seen that the sum of the two highest ion densities ( $H^+$  and  $O^+$ ) predicted by these steady-state solutions to the plasma transport equations for supersonic  $H^+$  outflow is within  $\pm 25\%$  of the median electron density values observed by DE-1 above  $2.5 R_E$ . Predicted ion densities for subsonic  $H^+$  outflow, on the other hand, are much higher at  $2 R_E$  than our data would suggest and the ion density profile drops off with increasing radial distance much more slowly than the PWI measurements indicate.

Recent measurements by the DE-1 High Altitude Plasma Instrument have established the existence of a low energy, field-aligned supersonic ion flux in the polar cap and a conic component of the ion flux due to the perpendicular heating of the field-aligned component [Gurgiolo and Burch, 1982]. The low energy, field-aligned ions constitute the classical polar wind as described by Axford [1968]. These measurements suggest that the subsonic  $H^+$  outflow solutions illustrated in Figure 14 are not appropriate in the polar magnetosphere at the altitude of the DE-1 orbit.

Below  $2.5 R_E$  the slightly lower theoretical ion densities based on the polar wind model, illustrated in Figure 14 for supersonic  $H^+$  outflows, are not unexpected since they are derived from the steady-state solutions to the plasma transport equations. The existence of steady-state conditions along polar magnetic field lines is related to the convection of plasma across the polar magnetosphere and to the speed of the magnetic convective cycle [Banks and Holzer, 1969b]. Regions of recently disconnected field lines, where the time delay has not been sufficient to achieve a steady state, can be expected to have higher

number densities than regions deep in the polar cap. Thus, number density can be expected to vary with magnetic latitudes across the polar cap. A rapid convective speed, which shortens the time interval between the merging and reconnection of magnetic field lines, may be sufficiently great to prevent the plasma from achieving a steady-state flow in the polar magnetosphere. Under these circumstances, observed number densities across the polar cap will be generally higher than the number densities predicted by the steady-state solutions. Variations in the number density due to changes in the magnetic latitude or disturbances in the magnetic field on small time scales have been minimized in this study by averaging densities over all polar magnetic latitudes for L-shell values greater than 10 at any given radial distance. The resulting density profile is expected to be higher than the predicted steady-state densities.

## VI. COMPARISON OF THE HIGH-ALTITUDE DENSITY PROFILE WITH TOPSIDE SOUNDER MEASUREMENTS

Figure 15 is a log-log plot of the electron number density as a function of radial distance from  $1.05 R_E$  to  $4.7 R_E$ . Electron densities for geocentric distances of  $1.05 R_E$  to  $1.47 R_E$  are median density values calculated from a random sampling of more than 350 high-latitude ( $\Lambda > 80^\circ$ ) density profiles derived from the Alouette II and Isis-1 topside sounder data. Error bars indicate the spread in electron density values for this random sampling of Alouette II profiles (1966-1967) and Isis-1 profiles (1969). The large density variations are due to latitudinal variations in temperature and ionic composition [Nelms and Lockwood, 1967] as well as variations in solar activity and magnetic field conditions.

There is an abrupt change in the nature of the Alouette/Isis density profile at approximately 1000 km ( $1.16 R_E$ ). This transition indicates a change in the basic processes of ion transport in the lower ionosphere. Below 1000 km, conditions of near diffusive equilibrium combined with an outward flux of plasma at subsonic transport speeds are expected to exist [Bauer, 1969]. A diffusive equilibrium model, based on the rapid diffusion of plasma above the F2 peak, predicts an electron density distribution of [Angerami and Thomas, 1964]

$$n_e \propto e^{-z/2h_i}$$

for  $z \approx R - l$

and  $h_i = kT_i/m_i g$

where  $n_e$  is the electron number density,  $R$  is the geocentric radial distance,  $k$  is Boltzmann's constant,  $h_i$  is the scale height of the dominant ion species,  $T_i$  is the ion temperature and  $m_i$  is the ion mass. An analysis of the Alouette/Isis density data below 1000 km yields a plasma scale height of 337 km. This value for the plasma scale height compares favorably with the  $O^+$  scale height of 282 km for a representative ion temperature of 4000°K at an altitude of 1000 km.  $O^+$  is the dominant ionospheric ion at all altitudes below 1000 km and is the leading term in the determination of the plasma scale height.

Although a vertical diffusive equilibrium distribution is a good approximation of the Alouette/Isis density profiles below 1000 km, the applicability of the model is limited in the polar cap region by the existence of geomagnetic field lines that are open into regions of low plasma pressure in the magnetotail [Bauer, 1969]. Such boundary conditions result in an outward plasma flow along the field lines at subsonic transport speeds below 1000 km [Banks and Holzer, 1969b]. In their solutions of the hydrodynamic transport equations for  $H^+$  and  $O^+$ , Raitt et al. [1975] determined that energy losses due to convective plasma motion are significant in determining density distributions between 700 km and 1000 km.

Above 1000 km, a weakening of the charge-exchange reactions between molecules and ions and a decrease in ion-ion friction due to rapidly decreasing densities results in an upward plasma flow along magnetic field lines [Banks and Holzer, 1969b]. This outward flow, even for low-energy, field-aligned ions, has been found to be supersonic [Gurgiolo and Burch, 1982]. The transition to supersonic transport speeds is theoretically expected to occur between 1000 km and 1500 km [Raftt et al., 1975]. However, the assumption of a collisionless plasma valid at the altitude of the DE-1 orbit, is not valid below 3000 km due to the substantially higher densities in this region. Ion transport processes, consequently, are found to depend in a complicated way on gradients in the plasma parameters and Coulomb collision frequencies [Schunk and Watkins, 1981; 1982; Raftt et al., 1975].

In the density data gap which occurs between the Alouette/Isis orbits and the DE-1 orbit, another transition must occur in order to fit the observed density profiles at low and high altitudes. The observed change in the density profile between  $1.55 R_E$  and  $2.0 R_E$  is attributed to the transition from a collision-dominated regime below to a collisionless regime above. In addition to changes in the basic plasma transport processes, transitions in the density profile may also be attributed to changes in the ionic composition and ion acceleration processes in the polar magnetosphere.

The topside sounder data used to derive the median density values observed in Figure 15 are biased toward regions of higher densities ( $> 300 \text{ cm}^{-3}$ ) by the standard methods of deriving electron densities from topside ionograms [Nelms and Lockwood, 1967]. Electron density values

for these profiles were calculated indirectly from the extraordinary wave reflection frequency and the gyrofrequency and upper hybrid resonance frequency [Hagg, 1967; Alouette II Ionospheric Data from Communications Research Centre in Ottawa] for ionograms on which all traces were distinctly visible. This indirect method of deriving density values was employed because the ordinary wave reflection trace at the plasma resonance  $f_p$  was not always observed, especially in low density regions at high latitudes and altitudes where the plasma frequency occasionally fell below the low frequency limit of the satellite's topside sounder.

In regions of very low electron densities and subsequently low plasma frequencies where  $f_p \ll f_g$ , the upper hybrid resonance frequency approaches the electron gyrofrequency and the indirect determination of electron density described above could not be used. Interference between the electron gyrofrequency and the upper hybrid resonance results in a difference or modulation frequency that can be determined from the ionograms and used to calculate electron densities below  $100 \text{ cm}^{-3}$  [Hagg, 1967]. The use of a modulation frequency technique to determine low density values resulted in the discovery of very low electron densities ( $< 100 \text{ cm}^{-3}$ ) for all polar latitudes ( $\lambda_m > 60^\circ$ ) at radial distances of  $1.24 R_E$  to  $1.47 R_E$  for selected ionograms on which the extraordinary wave reflection trace was not distinctly visible [Nelms and Lockwood, 1967; Hagg, 1967]. The inclusion of these very low densities on Figure 15 would lower the error bars of the Alouette/Isis density curve by an order of magnitude above  $1.2 R_E$ . This would reduce the discrepancy between the low-altitude density studies and the

observed DE-1 density values, since the whistler mode frequency cutoff method of determining electron densities is valid for low densities (see Figure 12). A more complete analysis of available topside ionograms would be necessary in order to determine an accurate slope of the electron density profile between  $1.24 R_E$  and  $1.47 R_E$ .

## VII. DISCUSSION AND SUMMARY

Electron densities at  $2.0 R_E$  to  $4.66 R_E$  have been derived from the plasma frequency cutoff of the whistler mode radiation in the polar cap using electric field spectrum measurements from the PWI on the DE-1 spacecraft. A log-log plot of the median density values as a function of radial distance indicates a power law distribution of electron densities, varying as  $R^{-3.85 \pm 0.32}$ . This power law distribution is consistent with a steady state, radial outflow model of ionospheric ions and electrons along polar magnetic field lines. It implies a nearly linear increase in plasma flow velocity with increasing radial distance.

A comparison of observed electron densities with theoretical ion and electron densities based on the classic polar wind model for supersonic ion flow velocities yields consistent results at  $2.5 R_E$  to  $2.8 R_E$ . The theoretical polar wind densities below  $2.5 R_E$  are slightly lower than the observed median densities. This result is not unexpected since conditions of steady-state plasma flow are not expected to exist across the polar cap at all latitudes and at all times.

A comparison of observed electron densities with low-altitude density profiles from the Alouette/Isis topside sounder data indicates several evolutions in the radial dependence of electron distributions in the polar cap. A state of near diffusive equilibrium combined with an outward flux of plasma at subsonic transport speeds below 1000 km

changes to a collision-dominated outward flux of plasma with a transition to supersonic velocities above 1000 km. This transition is clearly evident in the low-altitude density profile at approximately  $1.16 R_E$  (see Figure 15). A second transition is also indicated in the density data gap between  $1.55 R_E$  and  $2.0 R_E$  to account for the changing nature of the density profiles at high and low altitudes in the polar cap. This second transition in the density profile is due to a change from a collision-dominated radial outflow distribution model below  $1.5 R_E$  to a collisionless power law distribution above  $2.0 R_E$ . Other factors affecting the change in the radial dependence of the electron number density include changes in the ionic composition of the plasma as well as changes in the plasma flow velocity and plasma temperature.

Large variations seen in low-altitude electron densities in earlier studies persist at the higher altitudes of the DE-1 orbit. The spread in the density data is the result of averaging over all polar magnetic latitudes and nearly 80 polar passes for the five-month time interval of this study. Such a survey would conceal all density irregularities on a short time scale and would even suppress irregularities of large spatial dimensions which are not consistent across the polar cap at a constant radial distance. Such irregularities in the density profile at low altitudes were discovered by the early topside sounder satellites. Alouette I, in a polar orbit at a constant radial distance of  $1.16 R_E$ , provided evidence of latitudinal, diurnal and seasonal variations in the electron density profile at high geomagnetic latitudes [Nelms, 1966; Thomas et al., 1966]. Superimposed on the monotonic decrease in number density with increasing latitude were

prominent peaks and troughs in the density distribution on spatial scales of several hundred km [Thomas et al., 1966]. In addition, many small scale irregularities in space and time contributed to the spread in the density data. Some large scale irregularities persisted over continuous polar passes in narrow bands of invariant latitude [Sato and Colin, 1969; Chan and Colin, 1969]. In general polar cap density distributions were found to be very irregular and to sensitively depend on magnetic activity, seasonal variations and local time.

Similar irregularities in the density profile are expected to persist at DE-1 altitudes. The previously cited example of density profile variability between successive polar passes (see Figures 6 - 10) are evidence of large density fluctuations in time periods of less than 8 hours. Such a large transformation in the density profile for the same region of the polar magnetosphere is probably due to abrupt changes in the magnetic field activity. Sufficient data to examine seasonal variations in the density profile at DE-1 altitudes are not yet available. Statistically significant density data for seasonal comparisons at the same radial distances in the polar magnetosphere cannot be obtained until the DE-1 orbit has precessed around to the northern polar cap region in the spring of 1985. But sufficient density data already exist to investigate latitudinal density variations in the polar cap region and to compare these results with low-altitude studies of latitudinal density variations in order to determine the radial extent of persistent maxima and minima in the electron density distributions. A further comparison of magnetic activity and the density profile as a function of time is planned in order to determine the

magnitude of the effect of magnetic convection on the electron density distribution at high geomagnetic latitudes and high altitudes.

## REFERENCES

- Angerami, J. J., and J. O. Thomas, The distribution of electrons and ions in the earth's exosphere, J. Geophys. Res., 69, 4537, 1964.
- Axford, W. I., The polar wind and the terrestrial helium budget, J. Geophys. Res., 73, 6855, 1968.
- Banks, P. M., and T. E. Holzer, The polar wind, J. Geophys. Res., 73, 6846, 1968.
- Banks, P. M., and T. E. Holzer, Features of plasma transport in the upper atmosphere, J. Geophys. Res., 74, 6304, 1969a.
- Banks, P. M., and T. E. Holzer, High-latitude plasma transport: The polar wind, J. Geophys. Res., 74, 6317, 1969b.
- Bauer, S. J., Diffusive equilibrium in the topside ionosphere, Proceedings of the IEEE, 57, 1114, 1969.
- Calvert, W., Ionospheric topside sounding, Science, 154, 228, 1966.
- Calvert, W., The auroral plasma cavity, Geophys. Res. Lett., 8, 919, 1981.
- Chan, K. L., and L. Colin, Global electron density distributions from topside soundings, Proceedings of the IEEE, 57, 990, 1969.
- Chappell, C. R., J. L. Green, J. F. E. Johnson, and J. H. Waite, Jr., Pitch angle variations in magnetospheric thermal plasma - Initial observations from Dynamics Explorer-1, Geophys. Res. Lett., 9, 933, 1982a.
- Chappell, C. R., R. C. Olsen, J. L. Green, J. F. E. Johnson, and J. H. Waite, Jr., The discovery of nitrogen ions in the earth's magnetosphere, Geophys. Res. Lett., 9, 937, 1982b.
- Chen, F. F., Introduction to Plasma Physics, Plenum Press Publishing Company, New York, 1974.

Coordinated Ionospheric and Magnetospheric Observations from the Isis 2 Satellite by the Isis 2 Experimenters, Vol. 3, High-latitude charged particle, magnetic field and ionospheric plasma observations during northern summer, National Space Science Data Center, November 1980.

Dessler, A. J., and F. C. Michel, Plasma in the geomagnetic tail, J. Geophys. Res., 71, 1421, 1966.

Dungey, J. W., Interplanetary magnetic field and the auroral zones, Phys. Rev. Lett., 6, 47, 1961.

Florida C. D., The development of a series of ionospheric satellites, Proceedings of the IEEE, 57, 867, 1969.

Gallagher, D. L., and D. A. Gurnett, Auroral kilometric radiation: Time-averaged source position, J. Geophys. Res., 84, 6501, 1979.

Gurgiolo, C., and J. L. Burch, DE-1 observations of the polar wind - A heated and an unheated component, Geophys. Res. Lett., 9, 945, 1982.

Gurnett, D. A., and L. A. Frank, VLF hiss and related plasma observations in the polar magnetosphere, J. Geophys. Res., 77, 172, 1972.

Gurnett, D. A., and L. A. Frank, Plasma waves in the polar cusp: Observations from Hawkeye 1, J. Geophys. Res., 83, 1447, 1978.

Gurnett, D. A., S. D. Shawhan, and R. R. Shaw, Auroral hiss, z-mode radiation and auroral kilometric radiation in the polar magnetosphere: DE-1 observations, J. Geophys. Res., 88, 329, 1983.

Hagg, E. L., Electron densities of 8-100 electrons  $\text{cm}^{-3}$  deduced from Alouette II high-latitude ionograms, Canadian Journal of Physics, 45, 27, 1967.

Hoffman, J. H., Ion mass spectrometer on Explorer XXXI satellite, Proceedings of the IEEE, 57, No. 6, 1063, 1969.

Hoffman, J. H., and W. H. Dodson, Light ion concentrations and fluxes in the polar regions during magnetically quiet times, J. Geophys. Res., 85, 626, 1980.

Jackson, J. E., and E. S. Warren, Objectives, history, and principal achievements of the topside sounder and Isis programs, Proceedings of the IEEE, 57, 861, 1969.

Mozer, F. S., C. A. Cattell, M. Temerin, R. B. Torbert, S. Von Glinski, M. Woldorff, and J. Wygant, The dc and ac electric field, plasma density, plasma temperature, and field-aligned current experiments on the S3-3 satellite, J. Geophys. Res., 84, 5875, 1979.

Nelms, G. L., Seasonal and diurnal variations of the distribution of electron density in the topside of the ionosphere, in Electron Density Profiles in the Ionosphere and Exosphere, ed. by J. Frihagen, North-Holland Publishing Company, Amsterdam, 358, 1966.

Nelms, G. L., and G. E. K. Lockwood, Early results from the topside sounder in the Alouette II satellite, in Space Research VII, ed. by R. L. Smith Rose, North-Holland Publishing Company, Amsterdam, 604, 1967.

Raitt, W. J., R. W. Schunk, and P. M. Banks, A comparison of the temperature and density structure in high and low speed thermal proton flows, Planet. Space Sci., 23, 1103, 1975.

Sato, T., and L. Colin, Morphology of electron concentration enhancement at a height of 1000 km at polar latitudes, J. Geophys. Res., 74, 2193, 1969.

Schunk, R. W., and D. S. Watkins, Electron temperature anisotropy in the polar wind, J. Geophys. Res., 86, 91, 1981.

Schunk, R. W., and D. W. Watkins, Proton temperature anisotropy in the polar wind, J. Geophys. Res., 87, 171, 1982.

Shawhan, S. D., Magnetospheric plasma waves, in Solar System Plasma Physics, Vol. III, ed. by L. J. Lanzerotti, C. F. Kennel and E. H. Parker, North-Holland Publishing Company, 211, 1979.

Shawhan, S. D., D. A. Gurnett, D. L. Odem, R. A. Helliwell, and C. G. Park, The plasma wave and quasi-static electric field instrument (PWI) for Dynamics Explorer-A, Space Science Instrumentation, 5, 535, 1981.

Shawhan, S. D., and D. A. Gurnett, The polarization of auroral kilometric radiation by Dynamics Explorer-1, Geophys. Res. Lett., 9, 913, 1982.

Shelley, E. G., W. K. Peterson, A. G. Ghielmetti, and J. Geiss, The polar ionosphere as a source of energetic magnetospheric plasma, Geophys. Res. Lett., 9, 941, 1982.

Stix, T. H., The Theory of Plasma Waves, McGraw-Hill Book Company, Inc., New York, 1962.

Thomas, J. O., M. J. Rycroft, L. Colin, and K. L. Chan, Experimental results from the Alouette I satellite, in Electron Density Profiles in the Ionosphere and Exosphere, ed. by J. Frihagen, North-Holland Publishing Company, Amsterdam, 322, 1966.

Timleck, P. L., and G. L. Nelms, Electron densities less than 100 electrons  $\text{cm}^{-3}$  in the topside ionosphere, Proceedings of the IEEE, 57, 1164, 1969.

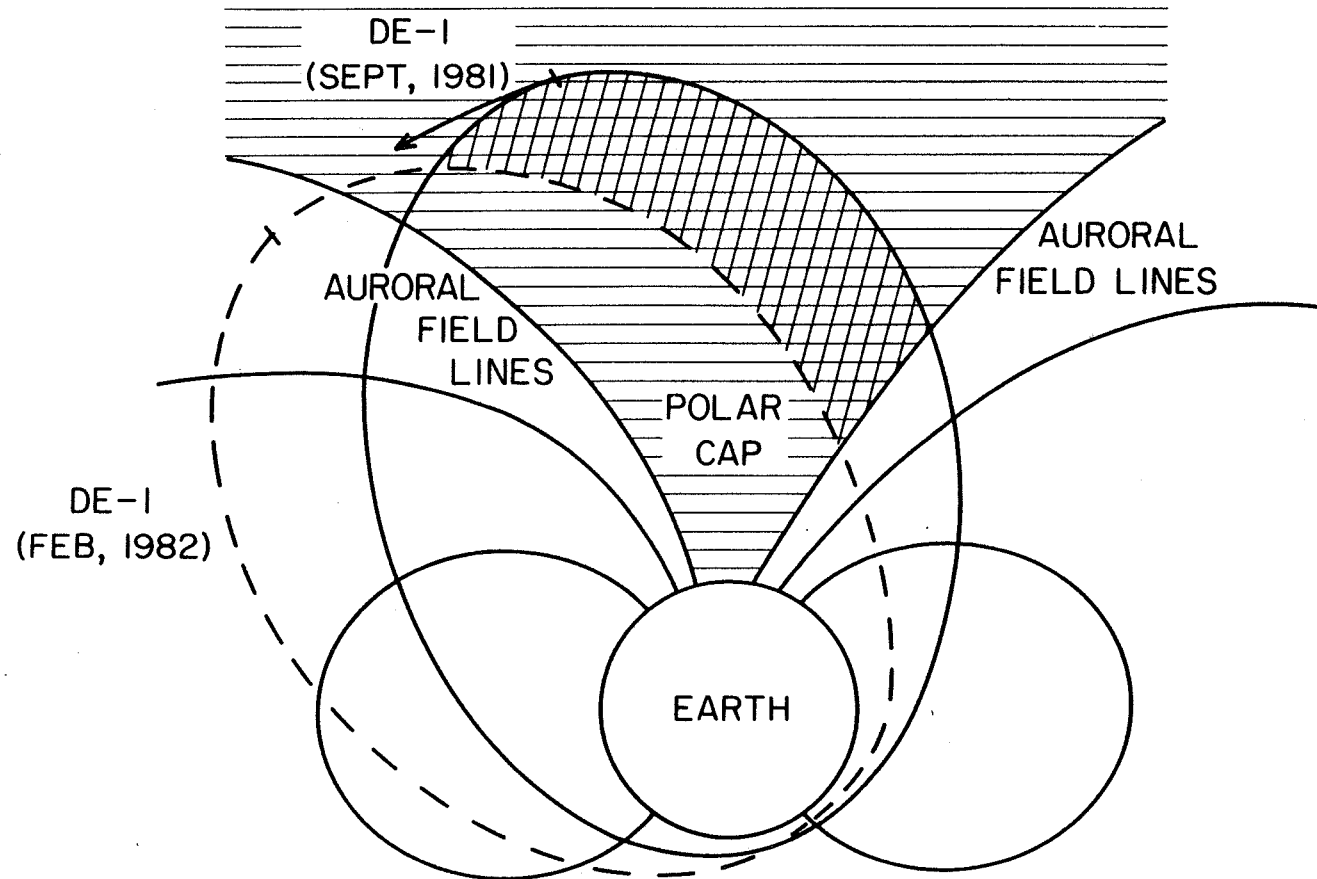
**APPENDIX A**

**FIGURES**

Figure 1

A representation of the orientation of the DE-1 orbit in September, 1981, and February, 1982. All density data presented in this study for this five-month interval are from high-latitude passes over the polar cap region.

A-G83-68-1



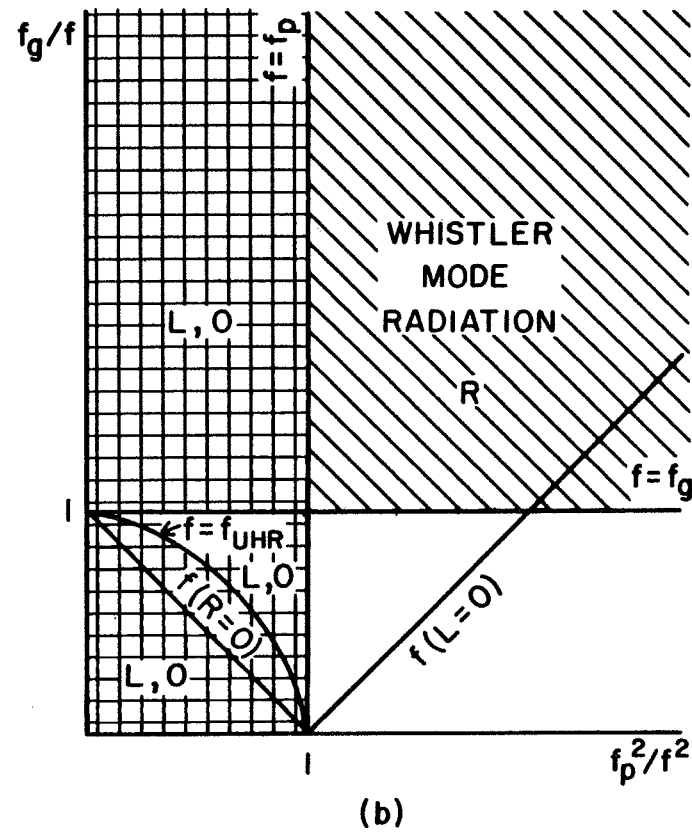
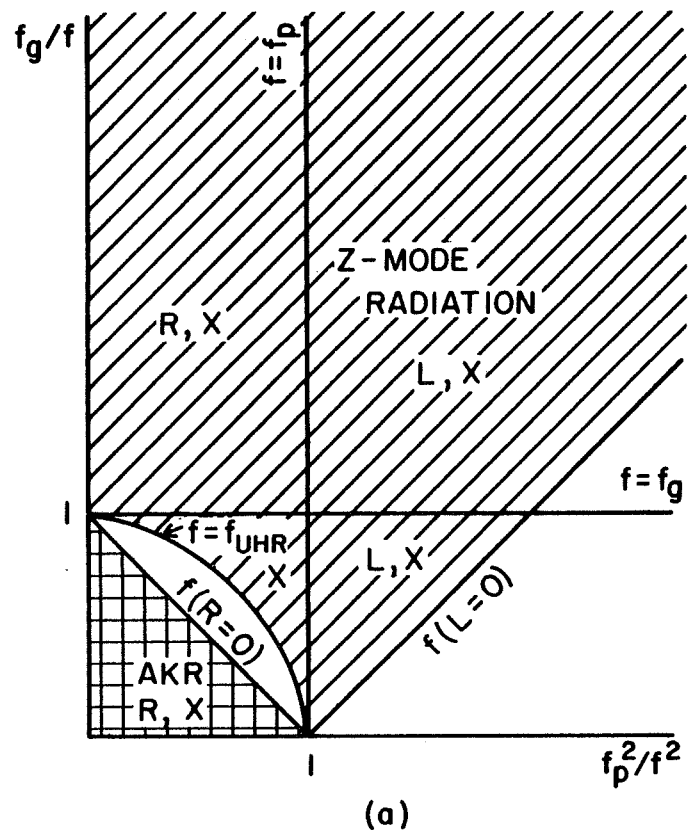
APOGEE ADVANCES IN DE-I ORBIT OVER A  
5-MONTH INTERVAL

Figure 1

Figure 2

CMA diagrams for a two-component plasma for frequencies near the electron gyrofrequency and plasma frequency [Stix, 1962; Chen, 1974].

Figure 2(a) illustrates the regions of allowed propagation for the free space R-X mode and the Z-mode. Figure 2(b) illustrates the regions of allowed propagation for the free space L-O mode and the whistler mode.



CMA DIAGRAMS FOR A SINGLE ION-ELECTRON PLASMA

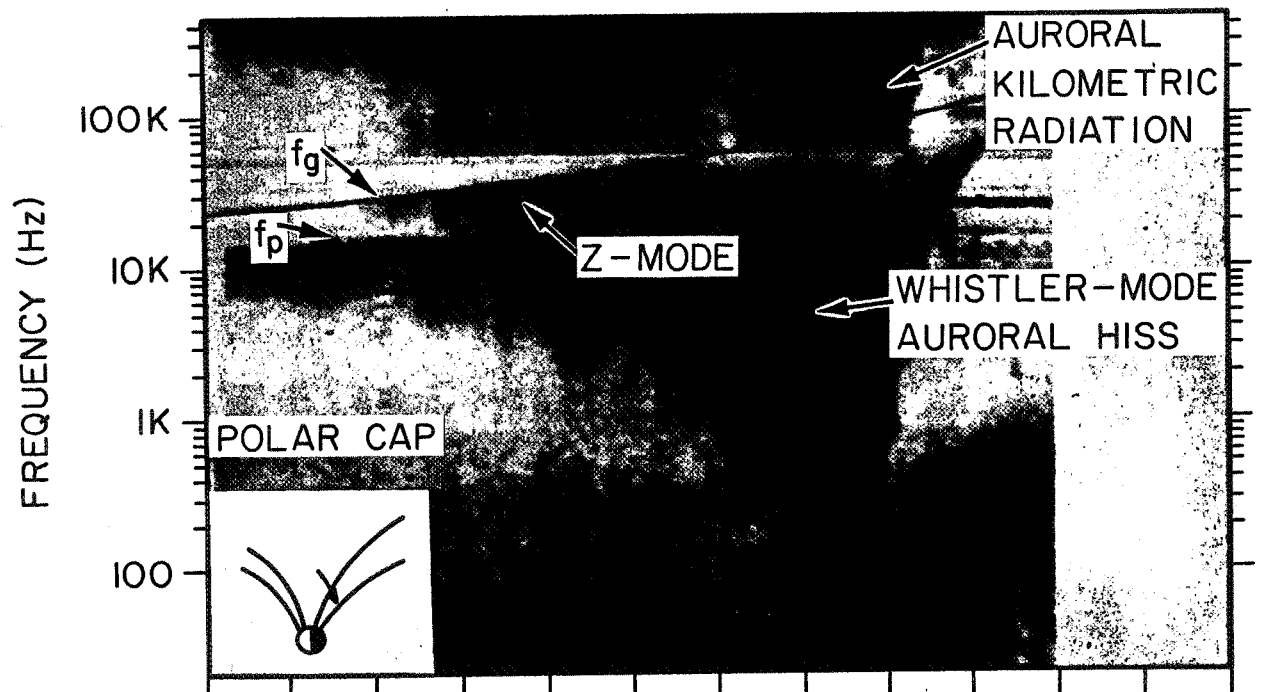
Figure 2

Figure 3

A representative spectrogram of electric field amplitude measurements illustrating the various plasma wave emissions found in the polar cap region near the electron gyrofrequency and plasma frequency.

A-G82-926-2

ELECTRIC FIELD, DE-I, NOVEMBER 5, DAY 309, 1981



UT	0520	0540	0600	0620	0640	0700	0720
$R (R_E)$	4.21	3.92	3.56	3.10	2.55	1.90	1.24
L			93.56	35.72	13.56	5.38	2.19
MLT	13.70	16.16	17.80	18.74	19.37	19.88	20.59
$\lambda_m$ (DEG)	79.07	77.25	71.04	61.33	47.09	23.67	-25.18

Figure 3

Figure 4 An illustration of representative whistler mode  
ray paths for sources located in the auroral zone  
and polar cusp at  $1.8 R_E$ .

A-G83-379

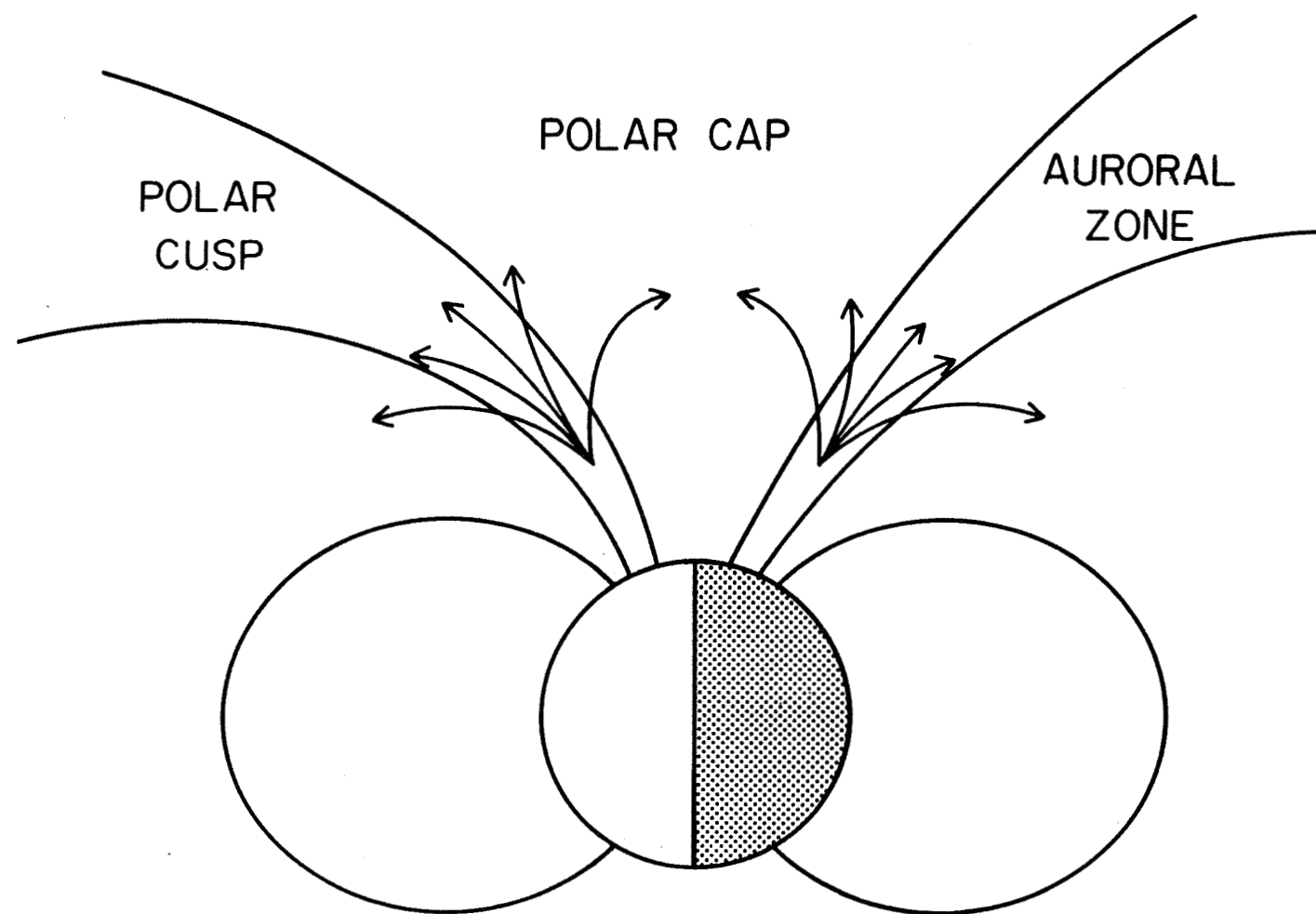


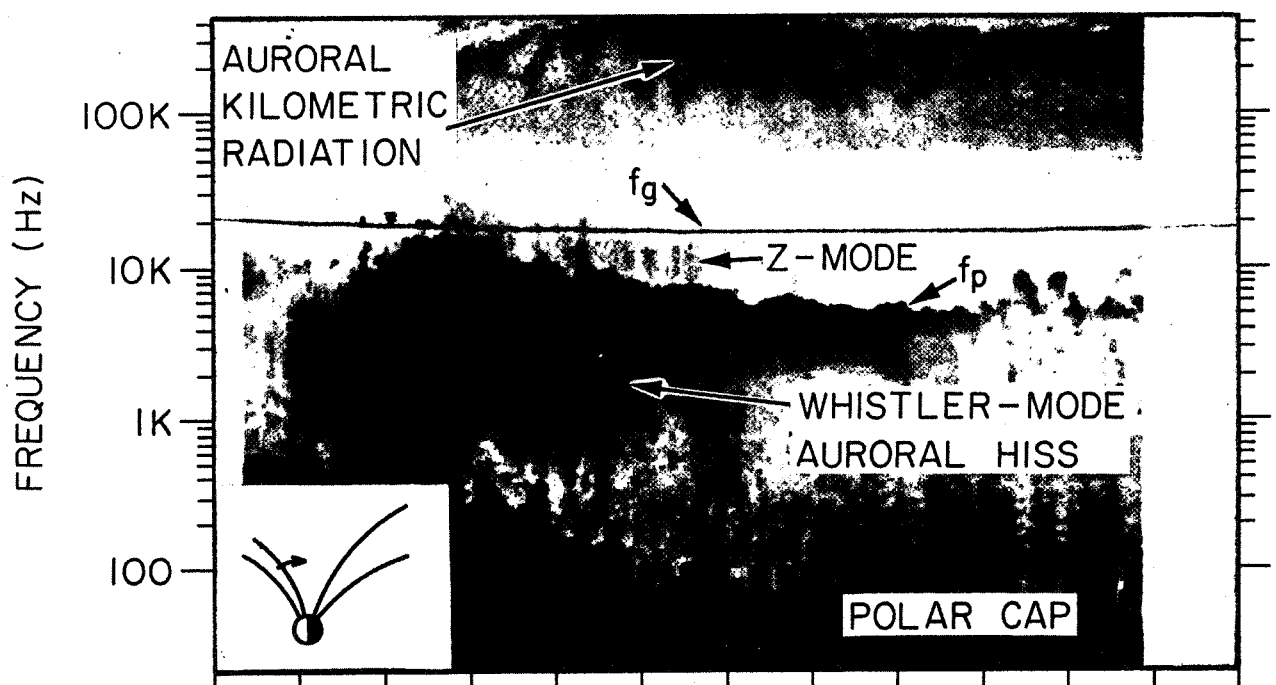
Figure 4

Figure 5

An electric field spectrogram of a polar cusp crossing in early October. Irregularities in the density profile are indicated by sudden increases in  $f_p$  at 0752 and at 0845-0850 as the satellite nears the pole.

A-G82-793-1

ELECTRIC FIELD, DE-I, OCTOBER 5, DAY 278, 1981



UT	0710	0730	0750	0810	0830	0850	0910
R( $R_E$ )	4.1	4.3	4.5	4.6	4.7	4.6	4.5
L	11.01	16.55	25.83	42.69	74.79		
MLT	11.1	11.4	11.9	12.5	13.5	15.1	17.2
$\lambda_m$ (DEG)	53.95	59.31	65.43	70.73	75.21	78.17	

Figure 5

Figure 6

A nightside crossing of auroral field lines in mid-February illustrating a depletion in electron densities at  $\lambda_m \approx 50^\circ$  [Calvert, 1981] and a smooth density profile inside the polar cap region.

A-G82-907-1

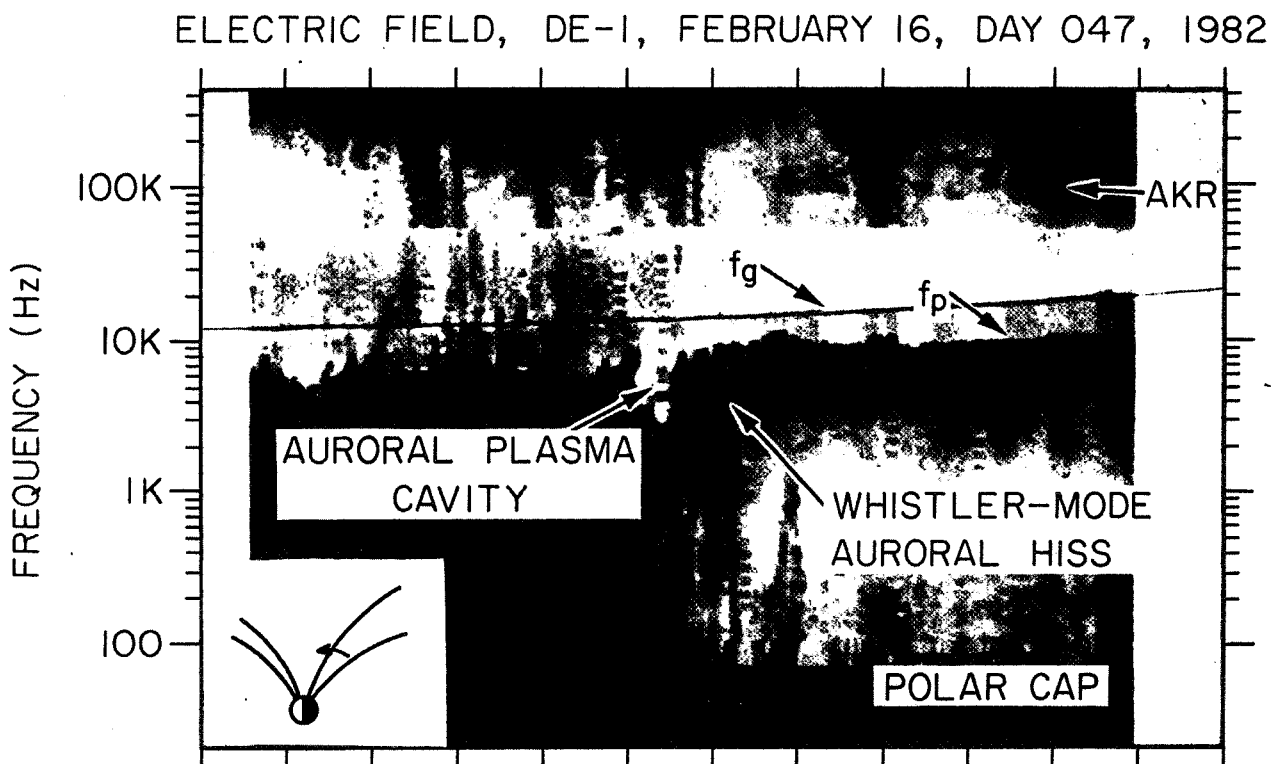


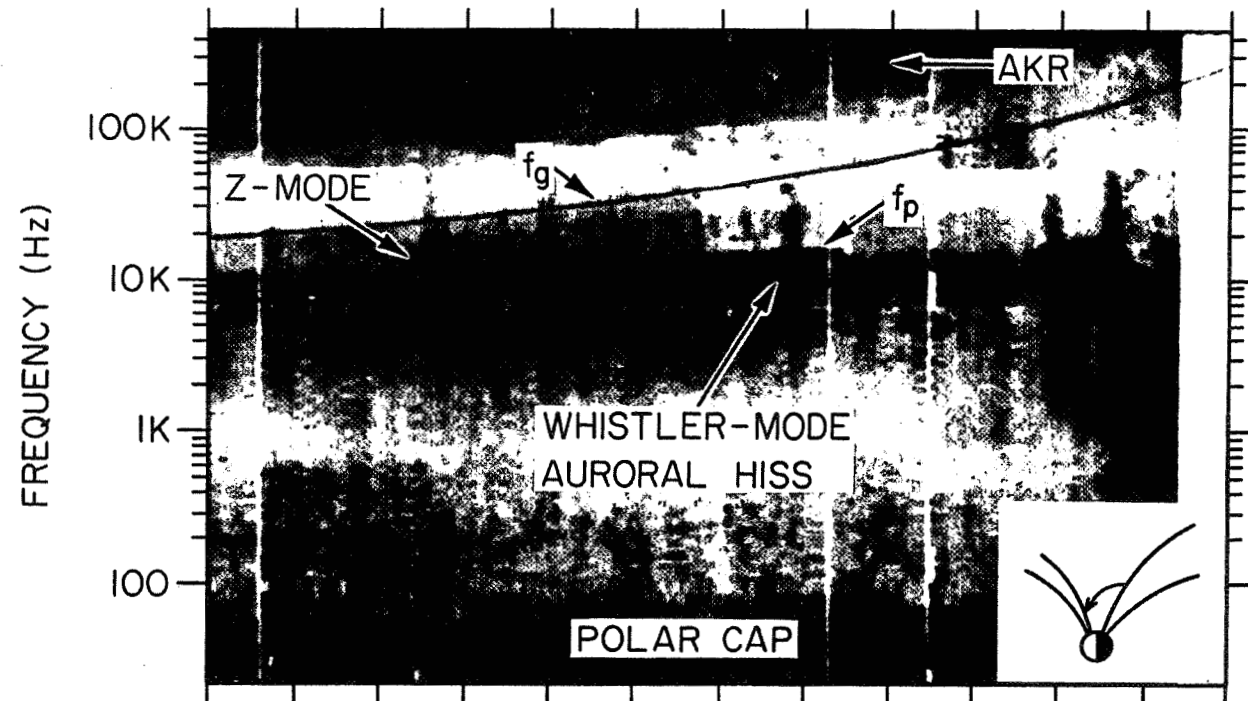
Figure 6

Figure 7

A continuation of the same polar pass illustrated in Figure 6. The density profile is smoothly varying over the entire polar cap region.

A-G83-214-1

ELECTRIC FIELD, DE-I, FEBRUARY 16, DAY 047, 1982



UT	0450	0510	0530	0550	0610	0630	0650
$R(R_E)$	4.39	4.17	3.87	3.49	3.02	2.45	1.78
L	20.66	32.10	65.42			22.68	3.69
MLT	1.08	1.03	0.91	0.28	13.93	13.36	13.15
m (DEG)	62.41	68.69	75.64	83.38	83.69	69.50	44.11

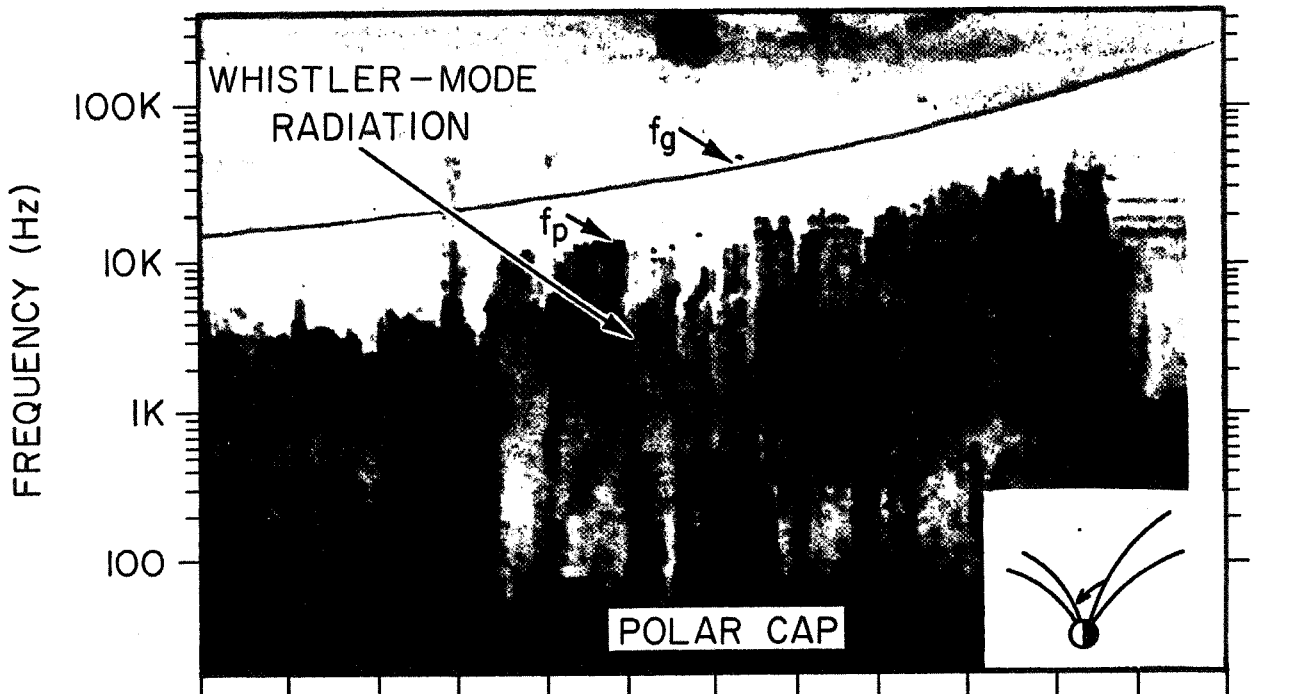
Figure 7

Figure 8

A spectrogram illustrating the time variability of the density profile. This pass preceded the pass illustrated in Figures 6 and 7 by just five hours for the same region of the polar magnetosphere. The density profile is highly variable on very short time scales.

A-G82-928-I

ELECTRIC FIELD, DE-I, FEBRUARY 15, DAY 046, 1982



UT	2200	2220	2240	2300	2320	2340	0000
$R (R_E)$	4.39	4.16	3.86	3.47	3.00	2.42	1.75
L	9.36	11.74	16.27	27.78	71.55	41.31	4.28
MLT	1.44	1.67	2.04	2.77	4.83	9.48	11.65
$\lambda_m$ (DEG)	47.00	53.66	60.99	69.18	77.33	74.83	50.87

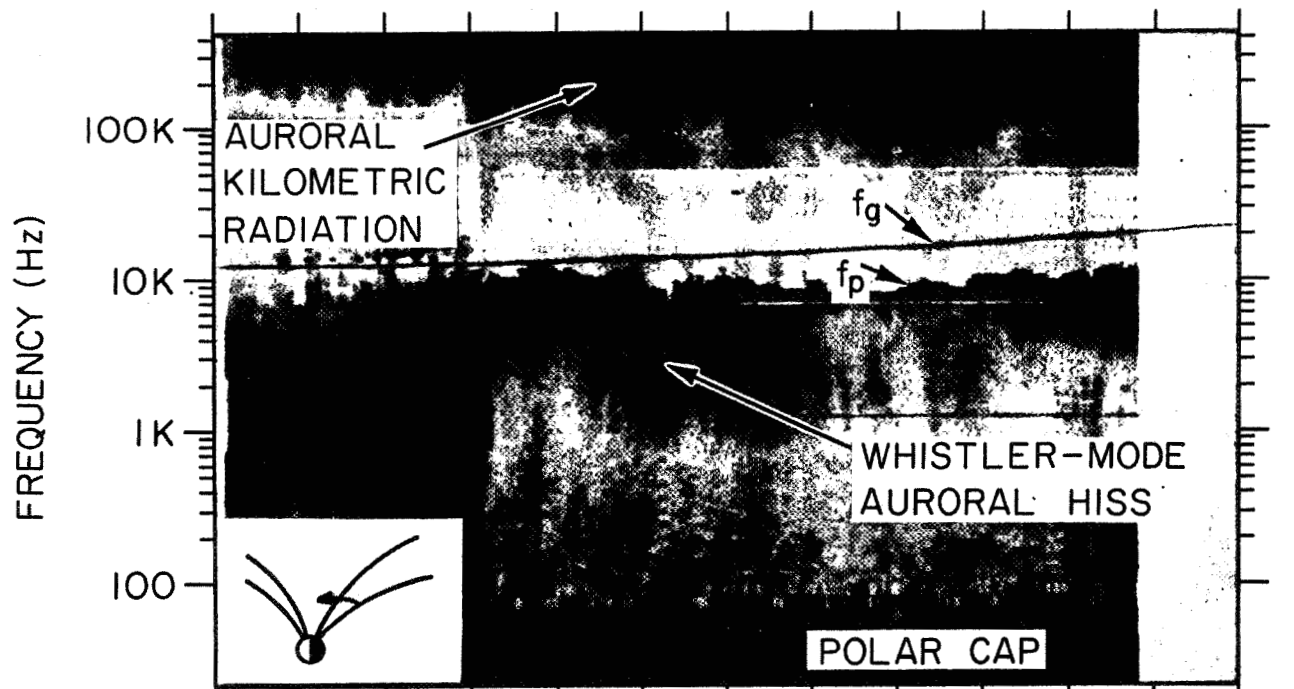
Figure 8

Figure 9

Another nightside crossing of the auroral field lines in early February. The density profile at low polar latitudes above  $50^{\circ}$  magnetic latitude is relatively smooth.

A-G82-906-1

ELECTRIC FIELD, DE-I, FEBRUARY 8, DAY 039, 1982



UT	0330	0350	0410	0430	0450	0510	0530
R( $R_E$ )	4.53	4.63	4.66	4.63	4.54	4.38	4.14
L	6.94	8.39	10.35	13.13	17.46	25.20	42.62
MLT	1.54	1.61	1.66	1.70	1.74	1.76	1.76
$\lambda_m$ (DEG)	36.36	42.28	48.00	53.66	59.39	65.35	71.73

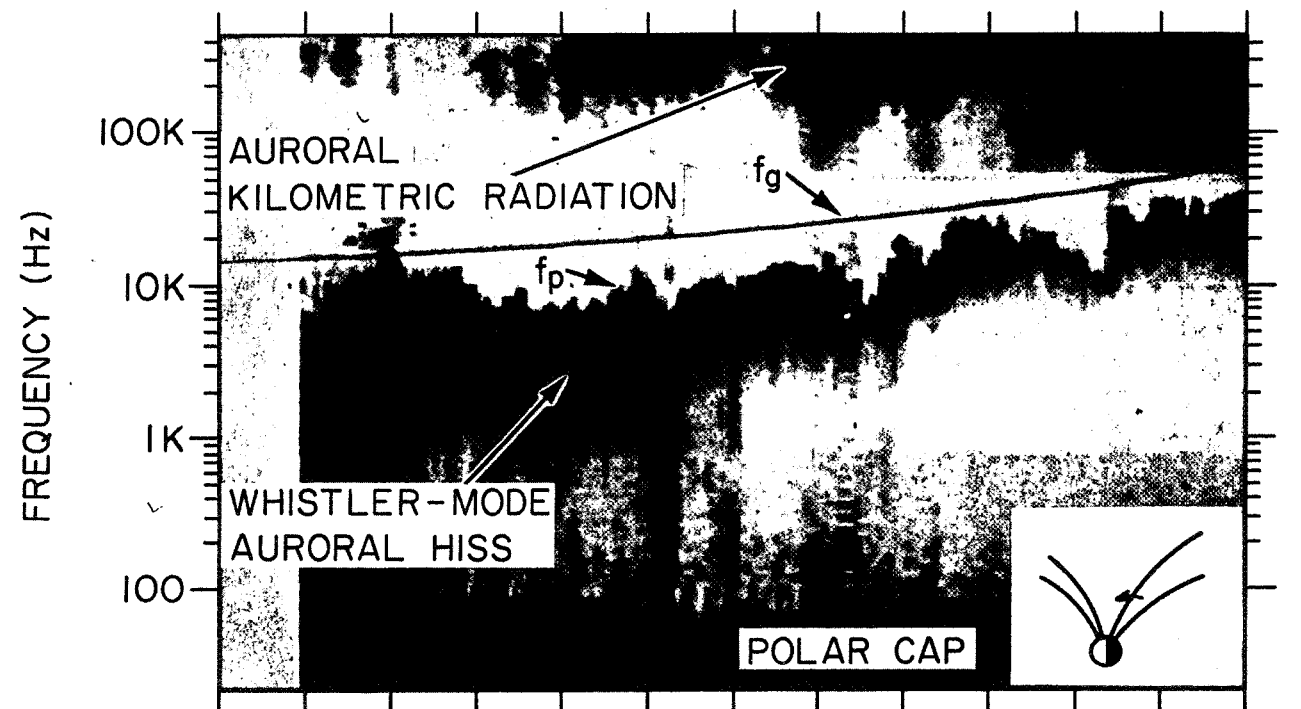
Figure 9

Figure 10

This pass follows the pass illustrated in Figure 9 by eight hours for the region of the polar magnetosphere just poleward of the nightside auroral zone. The density profile is highly irregular with fluctuations by a factor of 2 on spatial scales of less than 700 km.

A-G82-911-2

ELECTRIC FIELD, DE-I, FEBRUARY 8, DAY 039, 1982



UT	1120	1140	1200	1220	1240	1300	1320
$R(R_E)$	4.63	4.54	4.38	4.16	3.85	3.47	2.99
L	9.41	10.84	12.82	15.89	21.74	36.31	85.75
MLT	0.71	0.55	0.37	0.12	23.76	23.09	21.30
$\lambda_m$ (DEG)	45.68	49.89	54.35	59.24	64.81	71.27	77.98

Figure 10

Figure 11

A scatter plot of electron density as a function of radial distance. The large scatter in the data is due to changing magnetic field conditions and latitudinal variations in the data.

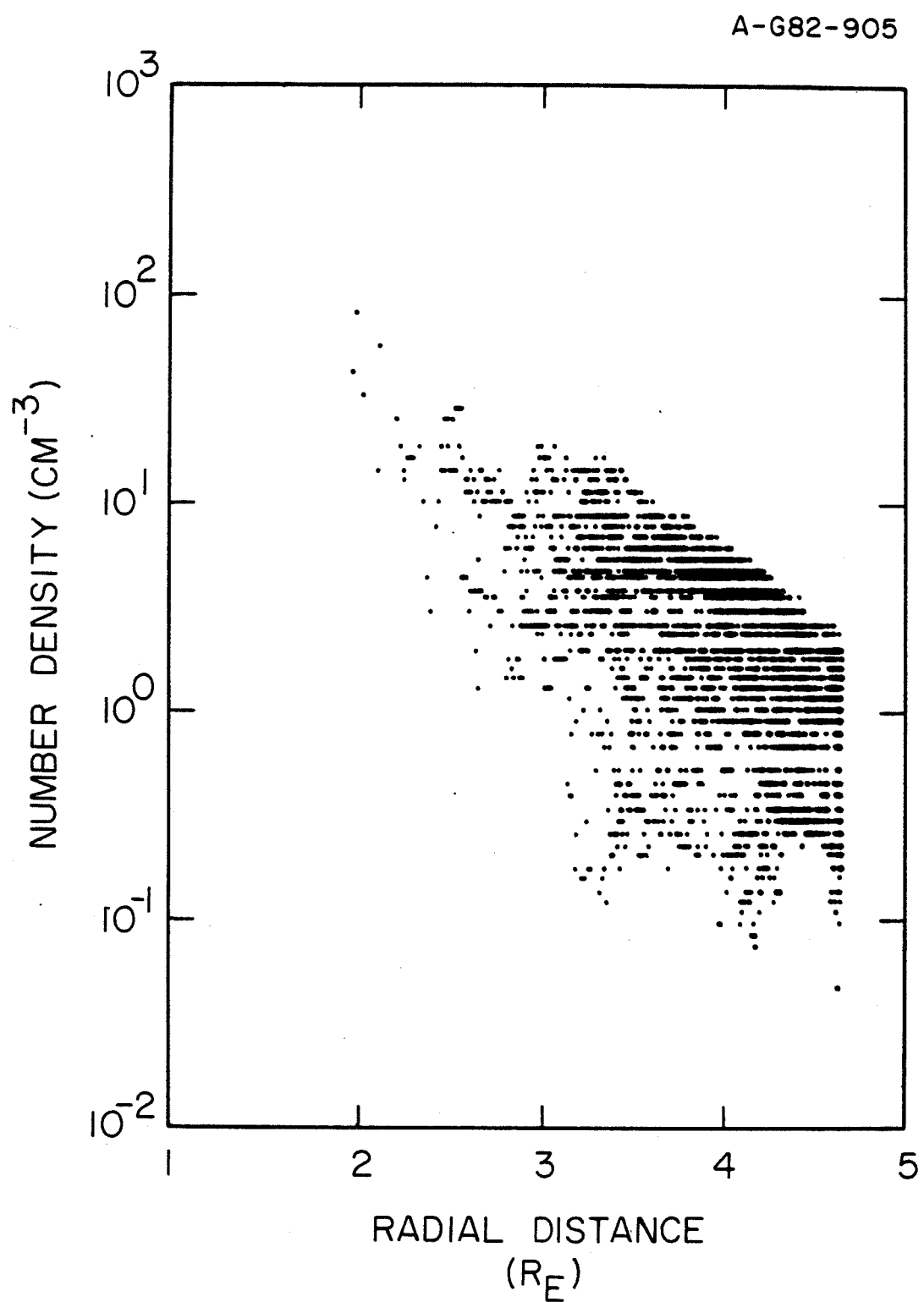


Figure 11

Figure 12      A log-log plot of median number densities as a function of radial distance. The best line fit through these points indicates a power law distribution for electron densities in the polar cap:  $n_e \propto R^{-3.85}$ .

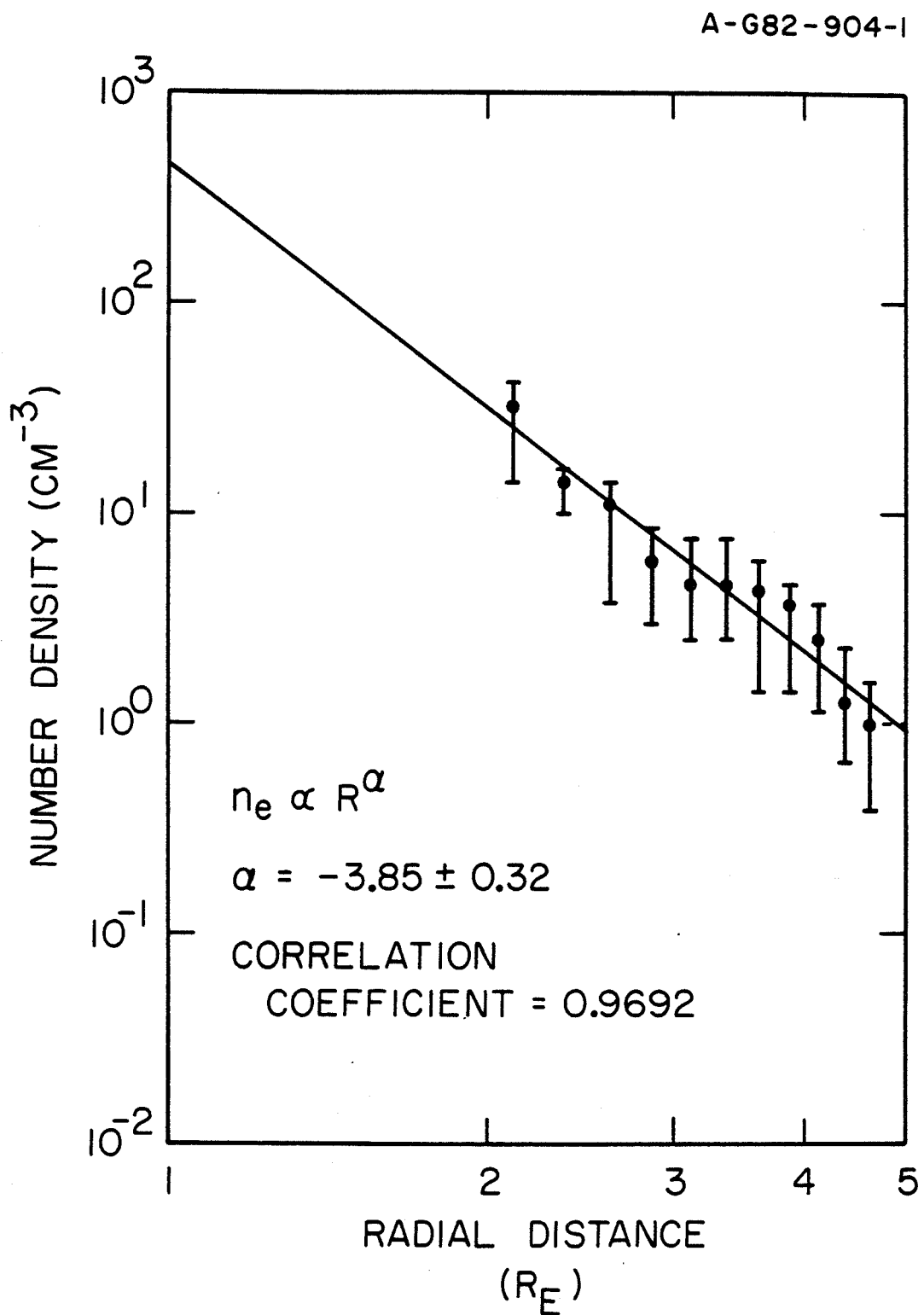


Figure 12

**Figure 13      Illustration of field-aligned ion flux at high  
geomagnetic latitudes.**

A-G83-227

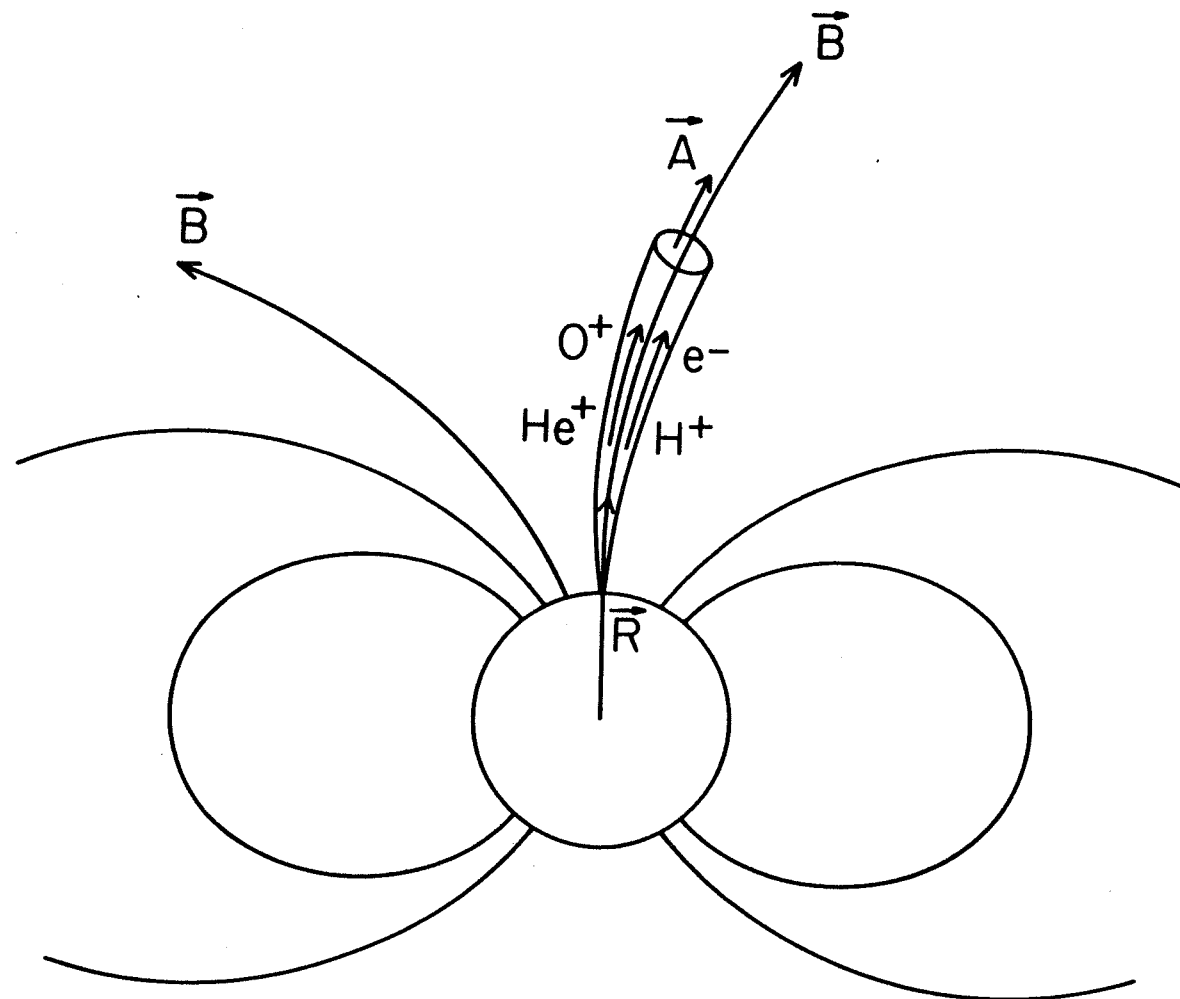


Figure 13

**Figure 14**

Predicted ion densities below  $2.8 R_E$  based on solutions to the 13-moment transport equations [Schunk and Watkins, 1982]. The subsonic outflow solutions correspond to higher  $H^+$  and  $O^+$  densities. These predicted densities exceed the DE-1 measured densities at  $2 R_E$  by more than an order of magnitude. Supersonic outflow solutions correspond to lower  $H^+$  and  $O^+$  densities. An increase in the boundary electron temperature gradient (from  $0.1^\circ K km^{-1}$  to  $1^\circ K km^{-1}$ ) corresponds to a slight increase in the predicted  $O^+$  densities and a larger decrease in the predicted  $H^+$  densities. Both sets of predicted ion densities for the supersonic outflow solutions are within 25% of the median density values observed by DE-1.

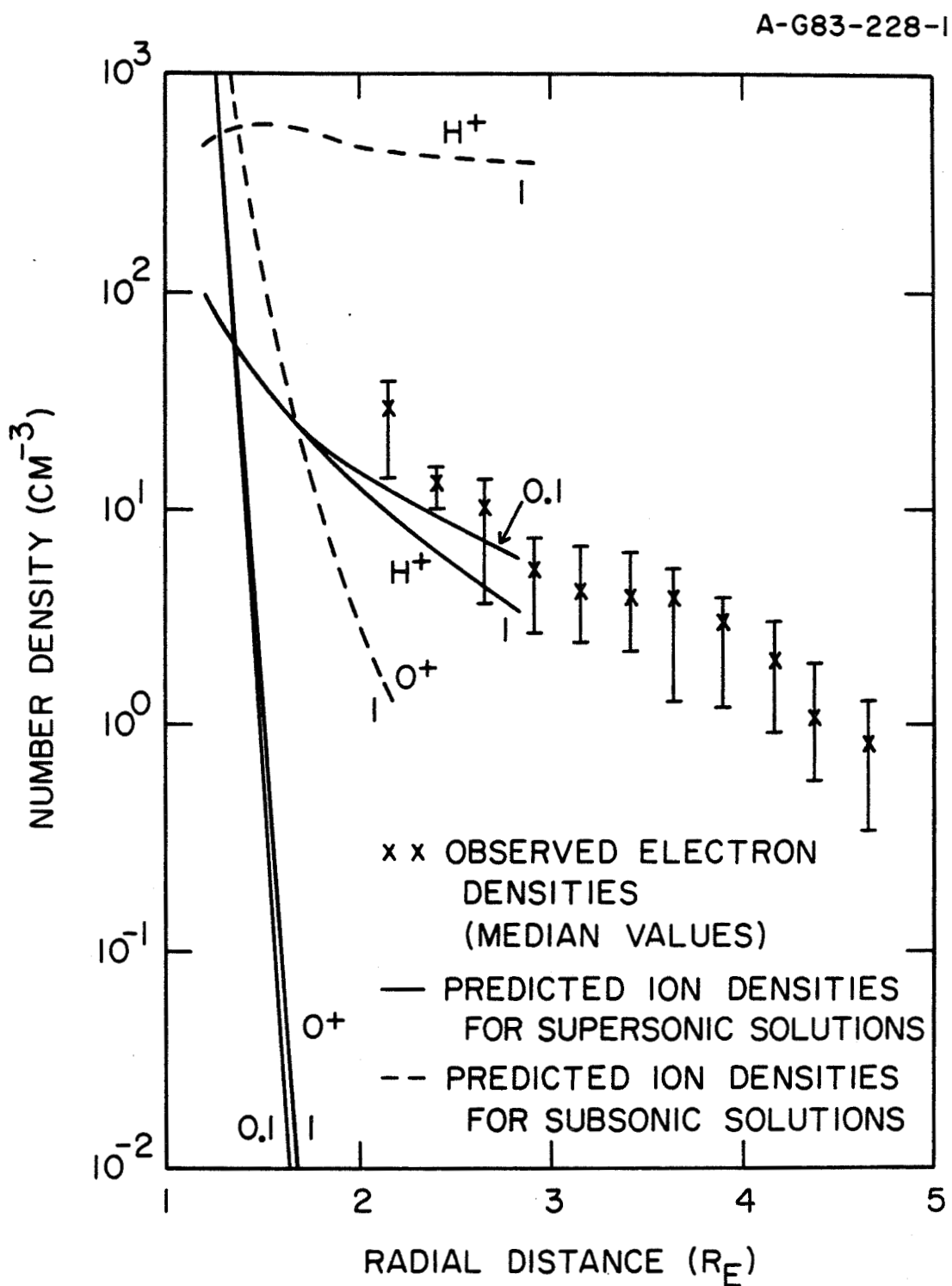


Figure 14

Figure 15

A log-log plot comparing low-altitude median electron densities obtained from the topside sounder data of Alouette II and Isis-1 and high-altitude median electron densities obtained from the PWI on DE-1.

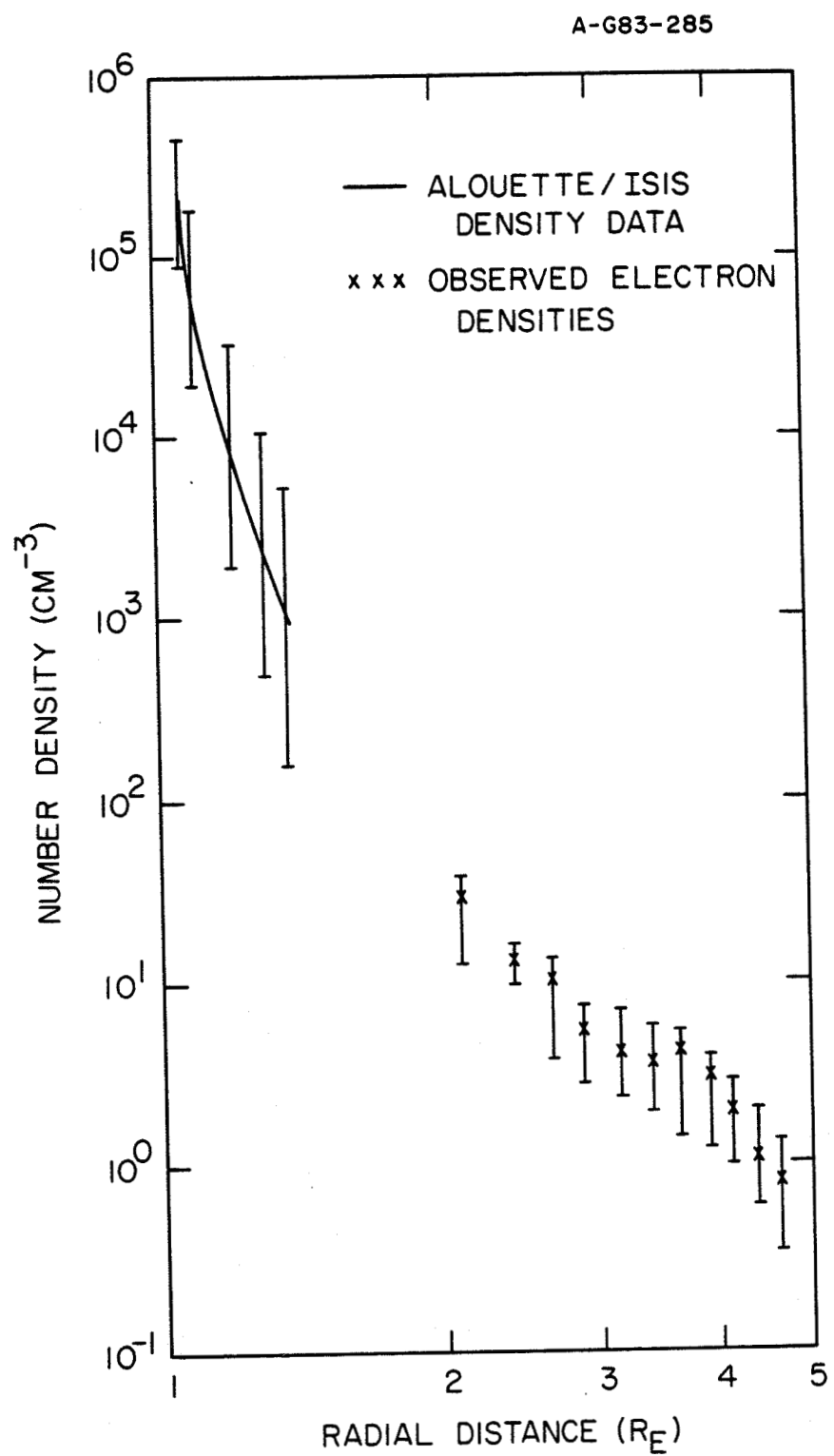


Figure 15